

Quantum transport in carbon nanotubes

A mis padres, hermanos y Empar

Quantum transport in carbon nanotubes

Proefschrift

ter verkrijging van de graad van doctor
aan de Technische Universiteit Delft,
op gezag van de Rector Magnificus prof.dr.ir. J.T. Fokkema,
voorzitter van het College voor Promoties,
in het openbaar te verdedigen op maandag 3 oktober 2005 om 15.30 uur

door

Pablo David JARILLO-HERRERO

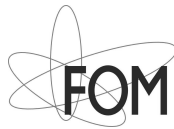
Master of Science in Physics, University of California San Diego, USA
geboren te Valencia, Spain.

Dit proefschrift is goedgekeurd door de promotor:

Prof. dr. ir. L. P. Kouwenhoven

Samenstelling van de promotiecommissie:

Rector Magnificus,	voorzitter
Prof. dr. ir. L. P. Kouwenhoven	Technische Universiteit Delft, promotor
Prof. dr. C. Dekker	Technische Universiteit Delft
Prof. dr. C. M. Marcus	Harvard University, Verenigde Staten
Prof. dr. Yu. V. Nazarov	Technische Universiteit Delft
Prof. dr. H. W. M. Salemink	Technische Universiteit Delft
Prof. dr. S. Tarucha	Tokyo University, Japan
Dr. Silvano De Franceschi	TASC National Laboratory, Italië
Prof. dr. ir. J. E. Mooij	Technische Universiteit Delft, reservelid



Printed by: Febodruk b.v., The Netherlands

<http://www.febodruk.nl>

Keywords: carbon nanotubes, quantum dots, Kondo effect

Cover theme: The beautiful path of scientific research

Cover design: Pablo Jarillo-Herrero

Front cover image: Grand Prismatic Spring, Yellowstone (NPS)

Back cover image from Chris Ewels (<http://www.ewels.info>)

An electronic version of this thesis, including color figures, is available at:

<http://www.library.tudelft.nl/dissertations/>

Copyright © 2005 by Pablo Jarillo-Herrero

All rights reserved. No part of the material protected by this copyright notice may be reproduced or utilized in any form or by any means, electronic or mechanical, including photocopying, recording or by any information storage and retrieval system, without permission from the author.

Printed in the Netherlands

Preface

When I first visited Delft for an interview in late March 2001, it was raining and hailing. Temperatures during the day: 4°C. Couldn't believe it. I had just arrived from sunny San Diego in southern California. Was I going to do my PhD here? A ~ 20 min lunch in the 'Aula' nearly threw myself back... Yet the group seemed very nice and the physics very interesting. I decided to come and, looking backwards, I definitely made the right choice.

This thesis describes experiments done during four years of research in the Quantum Transport (QT) group at Delft University of Technology. Many people have contributed both to my research and, very importantly, to the many good moments in this important period of my life.

First of all I want to thank my advisor Leo Kouwenhoven. Thanks for your enthusiasm and deep insight with science and for the freedom to explore whatever I wanted, while at the same time encouraging me to focus on relevant experiments. I admire your ability to choose the right people to form a very good group, with a very informal atmosphere and where excellent research and personal life can be perfectly combined. Thanks for those 'very good Pablo' every now and then, and the responsibility and trust in sending me to important conferences.

I owe an especial acknowledgement to professor Seigo Tarucha, from the University of Tokyo, for providing, through the ERATO, SORST and ICORP programs, the funding for my salary and research. Domo arigato gozaimass!

This thesis would not have been possible without the help of many collaborators. I want to thank you all for the exciting experience of working together these years. I want to start by thanking Silvano De Franceschi, 'Grandissimo Signore dell'Italia', a good friend and a true supervisor. Working with you in the mid part of my PhD has had the strongest influence in shaping me as a young scientist. I admire your profound knowledge of physics, your enthusiasm and capability to work countless hours, and your patience and willingness to explain and discuss science. I've enjoyed our multiple discussions on physics and non-physics issues inside and outside the lab. I'm glad you finally admitted that the Spanish 'Jamón pata negra' is better than the Italian 'Prosciutto di Parma'. I will visit you soon

in Trieste! Sami Sapmaz, co-founder of the nanotube transport team, has been a very important collaborator during my PhD. A lot of hard work, during the good and the not so good times, has resulted in a strong nanotube research subgroup within QT. It could not have occurred without you. Your many stories about Turkey have definitely made me wish to visit it, I hope to go soon. Çok tesekkür ederim!. The nanotube effort in Delft greatly benefitted with the arrival of Jing Kong, the most efficient person fabricating I've ever met!. I have enjoyed very much all the time we worked together in the lab. I've also learnt a lot from your chemist (i.e., practical) approach to things. I appreciate very much your friendship and I hope you can keep your sweet and cheerful personality in the wild MIT. During the last months of my PhD I've had the pleasure of working very closely with Jorden van Dam, a really nice and talented person. Pianist, politician, and a great researcher (I could keep on...). Our multiple successful two-sample cool downs have redefined the concept of 'efficient dilution fridge use'!. Jorden, bedankt voor alles. Herre van der Zant played an important role during the first half of my PhD. Thanks for all the support and encouragement, especially when things were not going so good, and thanks also for the confidence you showed proposing me for talks abroad already early on. The close collaboration with the group of Cees Dekker has been very important for my research. Cees, thanks for the discussions, critical reading of papers, the usage of MB facilities, and your good eye hiring people. The nanotube transport team has grown with the incorporations of Carola Meyer (thanks for the lessons on German politics and science!) and Piotr Beliczynski (a fan of Valencia and Spain!). I wish you all the best with NT qubits! We have had several students in the team. I had the pleasure to supervise Chris Lodewijk during his Masters project. I'm very glad that your latter work got recently rewarded, and that you decided to keep on with physics research. I've had also a nice time co-supervising or simply discussing with Samir Etaki, Arjan van Loo, Jan-Willem Weber and Edoardo.

QT is world-wide recognized by its research output. But what less people probably know is the phenomenal group atmosphere here, largely responsible in fact for the former. I want to especially thank Hans Mooij as founder of what I consider the 'Mooij School'. I want to thank everybody in QT for making my PhD time here so enjoyable, and especially: Leonid Gurevich, for introducing me to the art of nanofabrication and all his help on various issues. My office mates Gunther Lientschnig (well known for his characteristic laugh!), Michel Hendriks, Franck Balestro (the Grenoblover), and Ethan Minot (I'm looking forward to join the Q-optics team) for the nice atmosphere in B003!. Hubert Heersche (world adventurer and QT-interieurverzorging), charming Wilfredillo van der Wiel (your thesis has been almost a guide for my research), the three F's: Floris Zwanen-

burg (and his Renault Clio), Frank Koppens (spider-man) and the always friendly Floor Paauw, Tristan Meunier (really funny French), Eugen Onac (with who I shared the ‘joyful times’ of writing a thesis), Jeroen Elzerman (temporary guest of the NT team), Laurens Willems van Beveren (BKV team mate), Alexander ter Haar, Yong-Joo Doh for the discussions on SC, Dirk van der Mast for organizing the QT boat-trip, easy going Christo Buizert, Pieter de Groot, Arend Zwaneveld, Ivo Vink, Silvia and Josh Folk, Allard Katan (spider-man 2), Jonathan Eroms, Patrice Bertet, Stefan Oberholzer, Ronald Hanson, Jelle Plantenberg, Adrian Lupascu (future NEMS expert), Lieven Vandersypen (sailing master), Bart van Lijen, Peter Hadley, who I could always ask basic physics questions, Kees Harmans (for the nice notes on mesoscopic physics), ex-Qter Ramón Aguado and all other (ex-)members of QT I may have forgotten!.

Research at QT is greatly facilitated by the help from Raymond Schouten (our electronics guru) and Bram van der Ende, alias ‘nightingale whistler’. I also want to acknowledge the support of Mascha van Oossanen, Leo Dam, Wim Schot, Willem den Braver and Leo Lander. Special thanks to always smiling Yuki French for all the management work. Thanks also to Ria van Heeren for help with housing issues and trips.

The excellent scientific research done in Delft is, of course, not only due to QT. Among the groups I’ve had special interaction are the Molecular Biophysics group of Cees Dekker and the Theory group led by Gerrit Bauer and Yuli Nazarov. I want to thank past and present members of both groups for the nice discussions and experimental help. At MB I particularly want to thank Henk Postma for his experimental help at the very beginning of my PhD, Keith Williams for his enthusiasm with nanotubes, Jeong-O Lee for her kindness and useful advices on fabrication, Diego Krapf (a ver si nos volvemos a tomar un mate pronto), Serge Lemay and Brian Leroy who can *see* nanotubes, Derek Stein (I still don’t think the BBC is *pro-government*) and Gilles Gaudin and his sense of humour.

The theorists upstairs form a really nice group. I want to thank first of all Yuli Nazarov for the many discussions on various aspects of mesoscopic physics. I really admire your broad and deep physical insight, and your scientific honesty. During the NEMS meetings I enjoyed discussions with Yaroslav Blanter and Milena Grifoni. Special thanks to Joel Pëguiron for his hospitality in Regensburg, and to Daniel Huertas, my first Spanish connection in Delft. I have also enjoyed discussions and chats with Gerrit Bauer (the professor with the largest computer display ever), Gabriele Campagnano ‘il napolitano’, Markus Kindermann, Omar Usmani, Siggi Erlingsson and Oleg Jouravlev. I’ve also enjoyed very much the enthusiastic lectures/talks from Carlo Beenakker, from Leiden University (he also has a cool website!).

I want to acknowledge all the personnel from DIMES for their superb job in making the nanofacility in Delft an excellent (and safe) place for nanofabrication. Special thanks to Emile van der Drift for his perseverance.

During my PhD I've had the opportunity to travel all around the world, visit beautiful countries and meet many people. I want to thank some of them for their warm hospitality. Professor Young Hee Lee and his students made my trip to Korea a very interesting experience. I enjoyed very much my visit to Japan, and the cordial hospitality of Abdou Hassanien and Madoka Tokumoto-san, from AIST (giving a seminar about Kondo with Kondo-sensei in the audience was certainly the highlight of the trip!). In the same trip I had the pleasure to visit NTT basic research laboratories (what a fantastic place for nanoscience!), and enjoyed the hospitality of Toshimasa Fujisawa. Hans Kuzmany, from University of Vienna, was very kind to invite me both to a nice conference in Kirchberg and to Vienna. Thanks also to Andrea Ferrari, for the invitation to visit Cambridge University and the dinner at 'High-Table'.

Here in Delft I've met many people whose friendship I appreciate very much. Special thanks to Marta (thanks for being my paranimf!) and Stefan (a true British, and I mean it as a compliment!), Fernando (and his famous 'fabada asturiana'), Paloma and her almost Spanish boyfriend, Luuk, Josep and Silvia, Cesar (toledano de pura cepa), Javis and Elena (er trio cordobé), and many other with whom I've also enjoyed the 'Spanish lunches' in the Aula (which soon became international with the Erasmus crowd). I cannot forget my *hurricane* friend Patricia and her never ending all-around-the-world stories.

The people who I love and love me most deserve special mention here. I want to thank all my friends from Spain for their patience and not forgetting about me after some many years abroad. Special thanks to Joaquín Fernández, who encouraged me to come to Delft for my PhD. My family have surely been the ones to suffer most the difficulties associated with my scientific career. I would certainly not be here without my parents, MariCarmen and Carlos: mamá, papá, sé que ha sido especialmente difícil para vosotros. Gracias por vuestro apoyo y confianza. My brothers Dani, Edu and Nacho also had to bear my being away for such a long time. Os quiero mucho a los tres. Finally I want to thank the most special person I found in my life: Empar. Thanks for all the time spent together, for your continuous support and love. Mi pequeña molestoncilla. Te quiero.

Pablo Jarillo-Herrero
Delft, September 2005

Contents

1	Introduction	1
1.1	Motivation	2
1.2	Why keep on studying carbon nanotubes?	3
	References	5
2	Basic theoretical concepts and device fabrication	7
2.1	Carbon nanotubes	7
2.2	Quantum dots	17
2.3	Carbon nanotube quantum dots	22
2.4	Kondo effect	25
2.5	Device fabrication	28
	References	32
3	Electron-hole symmetry in a semiconducting carbon nanotube quantum dot	35
3.1	Introduction	36
3.2	A few electron-hole quantum dot	36
3.3	Electron-hole symmetry	39
	References	44
3.4	Appendix	45
4	Electronic excitation spectrum of metallic carbon nanotubes	49
4.1	Introduction	50
4.2	Four-fold shell filling	50
4.3	HiPCO nanotubes	52
4.4	CVD nanotubes	54
	References	55
5	Electronic transport spectroscopy of carbon nanotubes in a magnetic field	57
5.1	Introduction	58

5.2	Semiconductor carbon nanotube quantum dots	58
5.3	Evolution of the ground state of the quantum dot with magnetic field	60
5.4	Inelastic cotunneling spectroscopy	63
	References	65
6	Orbital Kondo effect in carbon nanotubes	67
6.1	Introduction	68
6.2	Orbital Kondo effect	70
6.3	SU(4) Kondo effect	72
	References	75
6.4	Appendix	78
7	Quantum supercurrent transistors in carbon nanotubes	83
7.1	Introduction	85
7.2	Quantum supercurrent transistor action	85
7.3	Correlation between critical current and normal state conductance	88
	References	91
7.4	Appendix	93
8	Tunneling in suspended carbon nanotubes assisted by longitudinal phonons	97
8.1	Introduction	98
8.2	Stability diagrams and low-energy spectra	99
8.3	Vibrational states and Franck-Condon model	101
	References	105
	Summary	107
	Samenvatting	111
	Curriculum Vitae	115

Chapter 1

Introduction

For a scientist working in mesoscopic physics, it is quite difficult to imagine a ‘world’ without quantum mechanics. Yet it’s not so long since Planck, Einstein, Bohr, Schrödinger, Heisenberg or Dirac, among others, started the ‘Quantum Revolution’. There is no doubt that the technology developed from our understanding of quantum mechanics has had a tremendous influence in the world and the way we live: from geopolitics to entertainment, from economics to health, and pretty much any aspect of life. Inventions like the transistor, the laser or the atomic bomb, just to name a few, have changed our world in a way that few people would have anticipated at the beginning of the 20th century. Some people believe that we are at the beginning of another revolution. Much to the regret of most physicists, this one may not be a conceptual revolution, like quantum mechanics, but purely technological: nanotechnology. In fact, it could be just a natural continuation of the technological revolution based on quantum mechanics. If scientists and engineers really get to control matter at the level of individual electrons or atoms, then the consequences for our world and the way we live will be greater than even the most imaginative physicist of the 20th century would have dreamed.

Nanoscience aims to study any phenomenon/object which occurs/exists at the nanometer scale. It is one of the most rapidly developing scientific disciplines and it has broken the traditional barriers separating physics, chemistry and biology. This interdisciplinary character of nanoscience is often quoted as one of its most important characteristics. Among the many objects being studied, carbon nanotubes (CNTs) have emerged as the prototypical nanomaterial: their diameters in the one to few nanometers range and their fantastic physical properties have made them immensely popular and they have, without any doubt, contributed very much to the nanotechnology ‘hype’.

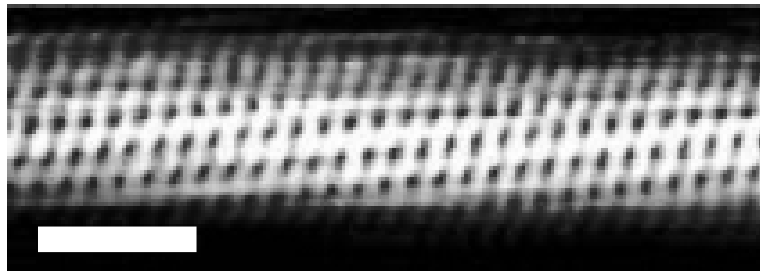


Figure 1.1: Scanning tunneling microscope picture of a carbon nanotube. The scale bar is 1 nm (from ref. [14]).

1.1 Motivation

When I visited the Quantum Transport group in Delft in the spring of 2001, I was suggested to do a PhD on electronic transport through carbon nanotubes, with emphasis on their electromechanical properties. Nanotubes were a very hot topic of research at the time, but one could easily wonder whether the ‘crest of the wave’ had already passed. After all, most of their basic electronic properties had been well established during the late 90’s (the ‘golden years’ for nanotube research) [1]. In fact, although I didn’t fully realize then, most of the people doing nanotube research were about to leave Delft at that moment, and the group of Cees Dekker, pioneer in the field and recently split from QT, was already moving into other directions, such as biophysics. Nevertheless, partly motivated by the amazing properties of nanotubes and partly naively, I embarked on this four-year trip and became the first PhD student of what is now the nanotube transport team in our group.

I immediately became fascinated with these objects: so tiny, so simple in structure, yet how much beautiful physics can be explored with them. Carbon nanotubes are tiny cylinders (of just few nm in diameter) made entirely out of carbon atoms (Fig 1.1). Basically one can think of them as a rolled graphite sheet (also known as graphene). They have lengths ranging from a few hundreds of nanometers up to several centimeters [2] and they are one of the strongest, yet lighter, materials on earth (approximately 5 times stronger than steel, yet 6 times lighter). Of particular interest are the electronic properties of CNTs. For example, they can behave as metals or semiconductors depending on their so-called ‘chirality’ (basically depending on how you roll the graphene sheet). They can also withstand current densities as high as 10^{13} A/m² (higher even than superconductors) and can behave as ballistic conductors at room temperature. But it is at low temperatures, in the ‘world of quantum mechanics’, that CNTs exhibit their most intriguing behaviour.

One of the most basic predictions of quantum mechanics is that a confined object can only have a discrete set of energy states. A familiar example of this are the electronic states in an atom. But this can also happen in solids. We call such ‘artificial atoms’ quantum dots (QDs). It turns out that electrons in a short segment of CNT, being confined in the three directions of space, have a discrete energy spectrum, and thus CNTs behave also as QDs. In order to observe this spectrum one needs to cool them down to temperatures below a few Kelvin, so that the thermal energy is smaller than the energy level separation.

The Quantum Transport group had a long research tradition on quantum dots (QDs) defined in semiconductor heterostructures, so it seemed natural to study carbon nanotube quantum dots. This actually proved more difficult than expected. Previous experiments [3, 4] had already shown that QDs can be formed in metallic CNTs, but their spectra, the most fundamental property of a QD, were highly irregular and could not be understood. The band structure of metallic CNTs is fairly simple, so verifying the predictions from theory was of fundamental importance to do more sophisticated experiments in CNT QDs. Some of the problems to be studied were: i) what is the role of the double orbital degeneracy in the transport properties of CNTs?; ii) is it possible to form QDs in semiconducting carbon nanotubes and reach the few particle regime?; iii) how is the transport modified when you attach different types of metals (superconductors, ferromagnets, etc...)?; iv) do the discrete phonon modes in finite size CNTs play any role in the transport?; v) is it possible to create tunable tunnel barriers in CNTs QDs?. Much progress has been done in most of these topics thanks to the work of several research groups around the world. The nanotube team in Delft has certainly contributed too and many of our results are contained in this thesis. All in all, I can affirm that the research into CNT QDs has reached a reasonable level of maturity, and there is no fundamental reason why CNTs cannot be used for most of the experiments done or planned in QDs defined in other systems, such as QDs in semiconductor heterostructures. In fact several groups with strong tradition in QD research in semiconductors have started research projects in nanotubes too.

1.2 Why keep on studying carbon nanotubes?

Much of the recent progress in nanotube research is due to improvements on the quality of CNTs. This means that CNTs are now a much more reliable system than they were before and there is a lot of fun physics to be explored with them. I briefly describe here some of the areas where I think there will be significant

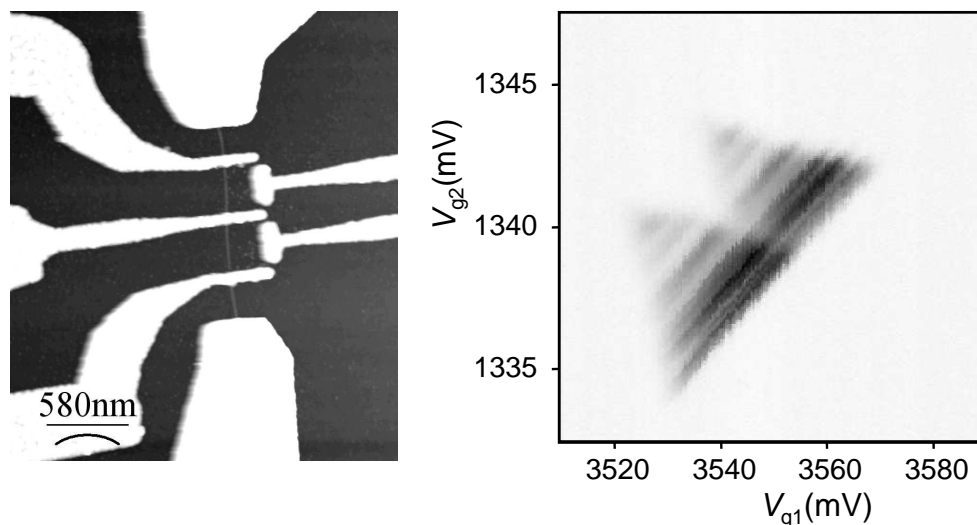


Figure 1.2: **a**, Atomic force microscope picture of a carbon nanotube double quantum dot. **b**, Current through a CNT double QD, at finite bias, as a function of each dot's side gate. The discrete lines correspond to transitions between the different electronic states in each dot. ([15]).

progress in the near future.

One 'traditional' advantage of QDs in semiconductor heterostructures over those in nanotubes is that the tunnel barriers that confine electrons in the dot can be tuned *in situ*. This enables to explore different experimental regimes by varying the coupling between the dot and the leads, and also to design novel geometries where multiple quantum dots are involved. It has recently been reported [5] that tunable tunnel barriers can be introduced in CNTs too, and several groups have been able to create, for example, double quantum dots (see Fig 1.2). I foresee many exciting results stemming from this area of research. One of them, for example, is the measurement of the spin and orbital relaxation times in CNT QDs. In semiconductor QDs, the orbital relaxation time has been measured to be of order \sim few ns [6], limited mainly by phonon emission. The spin relaxation time, on the other hand is much longer, of order $\sim 100\mu\text{s}$ [6], and limited by spin-orbit interaction. In CNT QDs these times have not been measured, but there is great hope that they will be long. On one hand, most of the phonon modes in CNTs have very large energies [7], so the probability of relaxation due to phonon emission will be low. This will lead to an increased orbital relaxation time. On the other, carbon is a light element, so the spin-orbit interaction is very weak, and this will also lead to very long spin relaxation times. Moreover, it has recently been shown that the interaction of the electron spin with the nuclear spins leads to a very short decoherence time in QDs defined in GaAs [8]. In

carbon nanotubes, most of the carbon is ^{12}C (with zero nuclear spin magnetic moment). In principle, pure ^{12}C nanotubes can be grown by using isotopically pure gases. Therefore, one can expect electrons in CNTs to have long spin de-coherence times. Another interesting experiment is to measure the spontaneous emission spectrum of a double QD [9] in a CNT. This will tell us information about phonon-mediated relaxation processes in CNT QDs.

An area of CNT research which is advancing very rapidly in recent years is the optical and optoelectronic properties of CNTs. Both photoluminescence [10] and electroluminescence [11] from individual semiconducting nanotubes has been measured. In principle, photoluminescence measurements enable the determination of the chirality of the nanotube being studied [12]. Recent measurements, however, have shown that the measured photoluminescence energies don't correspond to the true band gap of the nanotube, but are much smaller due to very strong exciton binding energies in CNTs [13]. This in itself is already very interesting and opens the door to many experiments. A good way to check this strong excitonic effects would be to combine low temperature electronic transport experiments, where the single particle band gap can be accurately measured, with photoluminescence measurements on the same nanotube, to measure the optical gap. Furthermore, by using short carbon nanotubes, one would be able to study photoluminescence from individual QD states in the valence and conduction band of CNTs, and thus perform similar studies to those done in self-assembled QDs or nanocrystals. Of course, these band gaps are tunable, by means of a magnetic field, for example, but also by means of strain. In addition, controlling the nanotube diameter also enables to have QD emitters with very different wavelengths.

All in all, you don't have to think too hard to find interesting experiments to be done with carbon nanotubes. Their properties are so unique, that there are almost endless opportunities to explore physics with them. Surely a big wave passed in the late 90's, but we'll be able to 'surf' still for many years.

References

- [1] For reviews, see C. Dekker, *Phys. Today* **52**, No. 5, 22-28 (1999); P.L. McEuen, *Phys. World*, June, 31-36 (2000); C. Schönenberger & L. Forro, *ibid.*, 37-41 (2000).
- [2] The current world-record length for an individual single wall carbon nanotube is ~ 4 cm. Zheng, L. X. *et al.* Ultralong single-wall carbon nanotubes. *Nature Materials* **3**, 673-676 (2004). It seems that this is just limited by the size of the substrate used. Who knows?, soon we could see meter long

- individual nanotubes in the labs!
- [3] Tans, S. J. *et al.* Individual single-wall nanotubes as quantum wires. *Nature* **386**, 474-477 (1997).
 - [4] Bockrath, M. *et al.* Single-electron transport in ropes of carbon nanotubes. *Science* **275**, 1922-1925 (1997).
 - [5] Biercuk, M. J., Garaj, S., Mason, N., Chow, J. M. & Marcus, C. M. Gate-defined quantum dots on carbon nanotubes. *Nano Letters* **5**, 1267-1271 (2005).
 - [6] Fujisawa, T., Austing, D. G., Tokura, Y., Hirayama, Y. & Tarucha, S. Allowed and forbidden transitions in artificial hydrogen and helium atoms. *Nature* **419**, 278-281 (2002).
 - [7] Rao, A. M. *et al.* Diameter-selective Raman scattering from vibrational modes in carbon nanotubes. *Science* **275**, 187-191 (1997).
 - [8] Johnson, A. C. *et al.* Triplet-singlet spin relaxation via nuclei in a double quantum dot. *Nature* **435**, 925-928 (2005).
 - [9] Fujisawa, T. *et al.* Spontaneous emission spectrum in double quantum dot devices. *Science* **282**, 932-935 (1998).
 - [10] Lefebvre, J., Homma, Y. & Finnie, P. Bright band gap photoluminescence from unprocessed single-walled carbon nanotubes. *Phys. Rev. Lett.* **90**, 217401 (2003).
 - [11] Misewich, J. A. *et al.* Electrically induced optical emission from a carbon nanotube FET. *Science* **300**, 783-786 (2003).
 - [12] Bachilo, S. M. *et al.* Structure-assigned optical spectra of single-walled carbon nanotubes. *Science* **298**, 2361-2366 (2002).
 - [13] Wang, F., Dukovic, G., Brus, L. E. & Heinz, T. F. The optical resonances in carbon nanotubes arise from excitons. *Science* **308**, 838-841 (2005).
 - [14] Wildoer, J. W. G., Venema, L. C., Rinzler, A. G., Smalley, R. E. & Dekker, C. Electronic structure of atomically resolved carbon nanotubes. *Nature* **391**, 59-62 (1998).
 - [15] Results from our group, measured by Sami Sapmaz *et al.*(2005).

Chapter 2

Basic theoretical concepts and device fabrication

2.1 Carbon nanotubes

Carbon nanotubes (CNTs) are thin hollow cylinders made entirely out of carbon atoms. There are many types of carbon nanotubes and carbon nanotube-like structures. The most basic ones are two: multiwall nanotubes (with diameters, d , of order ~ 10 nm) and single wall nanotubes ($d \sim 1$ nm) (see Fig. 2.1). Multiwall carbon nanotubes were discovered by Japanese scientist Sumio Iijima in 1991 [1] and, two years later, individual single wall carbon nanotubes were reported [2, 3]. Immediately after their discovery, it became clear that these tiny objects would have very remarkable electronic properties [4, 5]. Still, it was not until 1997 that the first electronic transport measurements on carbon nanotubes were performed [6, 7], thanks by a large part to a new growth method developed by the group of R. Smalley that enabled the production of large amounts of carbon nanotube material [8]. Since then, the number of groups working on the electronic properties of carbon nanotubes has increased dramatically.

Constructing a carbon nanotube

Carbon nanotubes have cylindrical structure and can be thought of as a rolled graphene sheet (graphene, a single sheet of graphite, is a honey-comb lattice of covalently bonded carbon atoms, see Fig. 2.2). There are many ways to roll a graphene sheet to form a CNT, so there are, in principle, an infinite amount of CNTs (if you allow the diameter to be as large as you want). One of the most interesting properties of CNTs is that the orientation of a carbon nanotube's axis with respect to the graphene crystal axes influences very strongly its electronic

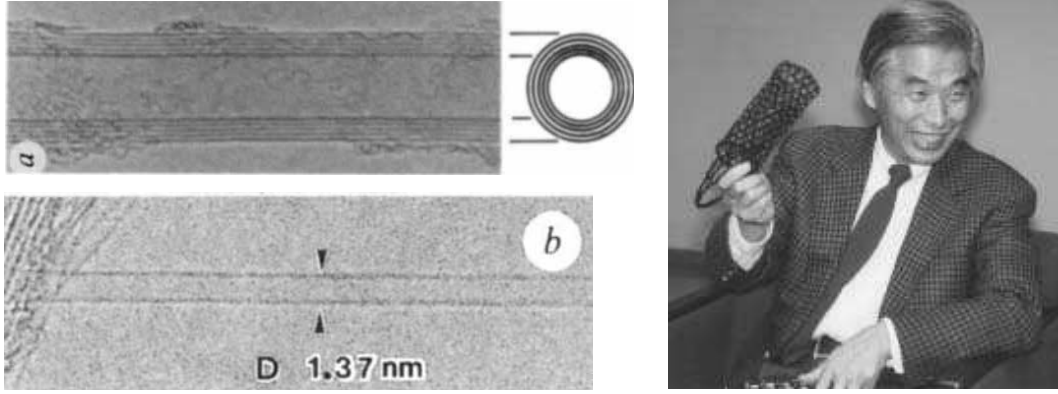


Figure 2.1: Discovery of carbon nanotubes. Left: Transmission electron microscope pictures of a multiwall nanotube (top) and an individual single wall nanotube (bottom) (from refs. [1, 2]). Right: Sumio Iijima, discoverer of carbon nanotubes.

behaviour. In particular, as we will see, CNTs can behave as semiconductors or as metals.

The geometry of a CNT is described by a wrapping vector. The wrapping vector encircles the waist of a CNT so that the tip of the vector meets its own tail. One possible wrapping vector, \mathbf{C} , is shown in Fig. 2.2. In this example, the shaded area of graphene will be rolled into the NT. The wrapping vector can be any $\mathbf{C} = n\mathbf{a}_1 + m\mathbf{a}_2$, where n and m are integers and \mathbf{a}_1 and \mathbf{a}_2 are the unit vectors of the graphene lattice. The angle between the wrapping vector and the lattice vector \mathbf{a}_1 is called the chiral angle of a NT. The pair of indexes (n, m) identifies the nanotube and each (n, m) pair corresponds to a specific chiral angle, θ , and diameter d :

$$\theta = \arctan[\sqrt{3}m/(m + 2n)] \quad (2.1)$$

$$d = C/\pi = \frac{a}{\pi} \sqrt{n^2 + m^2 + nm} \quad (2.2)$$

where $a = |\mathbf{a}_i|$ (~ 0.25 nm) is the lattice constant. A nanotube whose (n, m) indices are $(12, 6)$, for example, will have then a diameter $d = 1.24$ nm and a chiral angle θ of 19.1° . Vector \mathbf{T} is perpendicular to \mathbf{C} and it points from $(0,0)$ to the first lattice site through which the dashed line passes exactly. The area defined by $|\mathbf{T} \times \mathbf{C}|$ is the primitive unit cell from which a nanotube can be constructed.

There are two special directions in the graphene lattice that generate non-chiral tubes. These correspond to the $(n, 0)$ and (n, n) lines in Fig. 2.2 and are

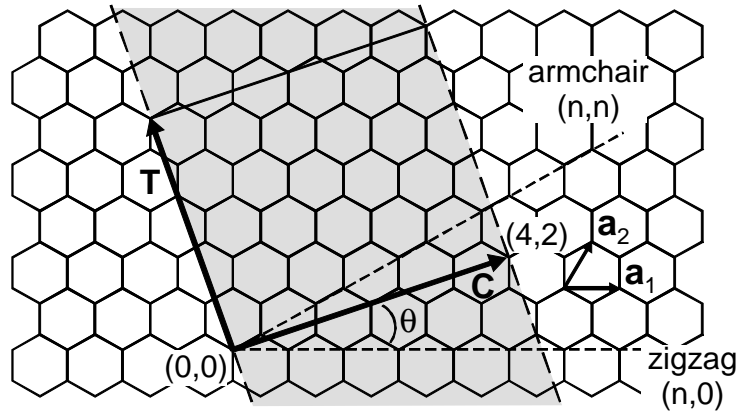


Figure 2.2: Construction of a carbon nanotube from a graphene sheet. By wrapping **C** onto itself, a CNT is generated with axis parallel to **T**. The grey area becomes the CNT. Any CNT, characterized by indexes (n, m) , can be constructed in a similar way. In this case, it is a $(4,2)$ NT. \mathbf{a}_1 and \mathbf{a}_2 are the unit vectors of the graphene lattice. Nanotubes constructed along the zigzag and armchair dashed lines are non-chiral.

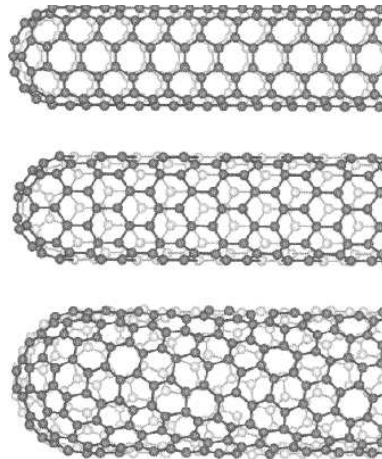


Figure 2.3: Examples of carbon nanotube geometries. From top to bottom: armchair, zigzag and a chiral nanotube.

called zigzag and armchair directions, respectively. They differ by a chiral angle of 30° . Figure 2.3 shows examples of an armchair, a zigzag and a chiral nanotube.

Graphene band structure

The electronic structure of carbon nanotubes can be derived from the band structure of graphene, which we describe here.

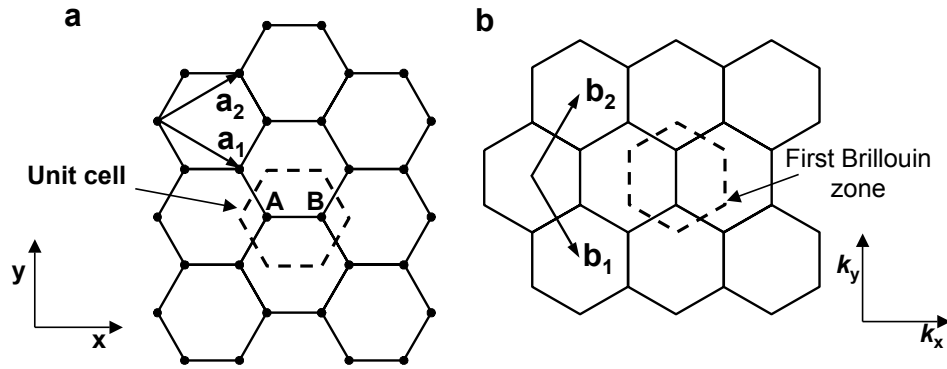


Figure 2.4: **a**, Real space atomic lattice of graphene. **b**, Reciprocal space lattice. In both cases the dashed lines denote the unit cells. The unit vectors satisfy $\mathbf{a}_i \cdot \mathbf{b}_j = 2\pi\delta_{i,j}$.

A graphene sheet consists of a two-dimensional array of carbon atoms arranged in an hexagonal lattice. Each carbon atom in graphene is covalently bonded to other three atoms, with which it shares one electron forming sp^2 ‘ σ -bonds’. The fourth valence electron of carbon occupies a p_z orbital. The p_z states mix together (‘ π -bonds’) forming delocalized electron states with a range of energies that includes the Fermi energy. These states are responsible for the electrical conductivity of graphene.

The real space geometry of graphene (a triangular Bravais lattice with a two-atom basis) is shown in Fig. 2.4a. There are two inequivalent sites in the hexagonal carbon lattice, labelled A and B. All other lattice sites can be mapped onto these two by a suitable translation using vectors \mathbf{a}_1 and \mathbf{a}_2 . The real space unit cell contains the two carbon atoms at A and B. Figure 2.4b shows the reciprocal space lattice, with the corresponding reciprocal space vectors and first Brillouin zone. P. R. Wallace calculated the band structure of graphene within a tight-binding approximation in 1947 [9]. Rather than giving here the explicit formula for the graphene band structure, and derive mathematically from it the band structure of carbon nanotubes (see, e.g., [10]), we will simply try to ‘visually’ understand the basic electronic properties of CNTs from the band structure of graphene.

The energy relation dispersion for graphene, $E(k_x, k_y)$, is plotted in Fig. 2.5a. Valence and conduction bands ‘touch’ each other at six points, which coincide with the corners of the hexagonal Brillouin zone. The Fermi surface reduces thus just to these six points. Because of this, graphene is called a semimetal, or zero band gap semiconductor. These special points, where conduction and valence bands meet, are called ‘K points’. The dispersion relation near these points is conical. Figure 2.5b shows a contour plot of the energy of the valence band

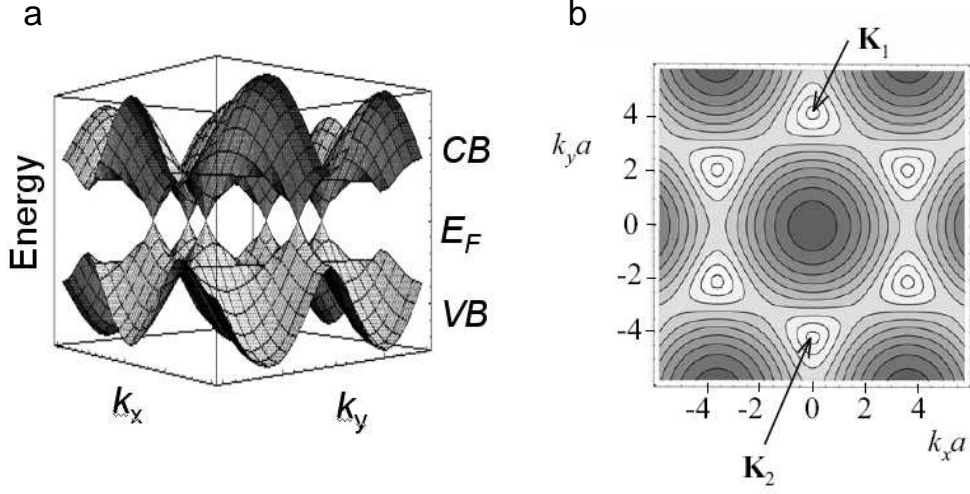


Figure 2.5: Graphene band structure. **a**, Energy dispersion relation for graphene. The valence (VB) and conduction (CB) bands meet at six points at the Fermi energy, E_F . **b**, Contour-plot of the valence band states energies in **a** (darker indicates lower energy). The hexagon formed by the six K points (white contour points) defines the first Brillouin zone of the graphene band structure. Outside this unit cell, the band structure repeats itself. The two inequivalent points, \mathbf{K}_1 and \mathbf{K}_2 are indicated by arrows (adapted from ref. [11]).

states. The circular contours around the K points reflects the conical shape of the dispersion relation around them. Only two of the six K-points are inequivalent (resulting from the two inequivalent atom sites of the graphene lattice), labelled \mathbf{K}_1 and $\mathbf{K}_2 = -\mathbf{K}_1$. In Fig. 2.5b, the lower two K-points on the hexagon sides can be reached from \mathbf{K}_1 by a suitable reciprocal lattice vector translation, so they are equivalent to \mathbf{K}_1 . Similarly, the two upper K-points are equivalent to \mathbf{K}_2 .

The electronic properties of a conductor are determined by the electrons near the Fermi energy. Therefore the shape and position of the dispersion cones near the K points is of fundamental importance in understanding electronic transport in graphene, and therefore in nanotubes. The two K points, \mathbf{K}_1 and \mathbf{K}_2 in Fig. 2.5b have coordinates $(k_x, k_y) = (0, \pm 4\pi/3a)$. The slope of the cones is $(\sqrt{3}/2)\gamma_0 a$, where $\gamma_0 \sim 2.7$ eV is the energy overlap integral between nearest neighbor carbon atoms [12].

Band structure of carbon nanotubes

The band structure of carbon nanotubes can be derived from that of graphene by imposing appropriate boundary conditions along the nanotube circumference.

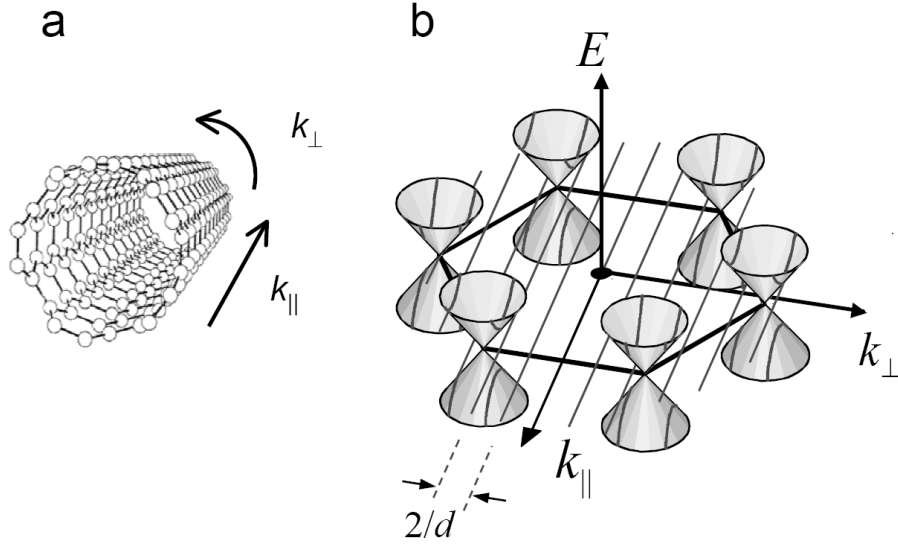


Figure 2.6: Quantized one-dimensional (1D) subbands. **a**, CNT and direction of k -axis. **b**, Low-energy band structure of graphene (near E_F), showing the one-dimensional subbands of CNTs obtained by imposing periodic boundary conditions along the NT circumference (adapted from [11]).

Typically, the diameters of carbon nanotubes (\sim few nm) are much smaller than their lengths (anywhere from hundreds of nm to several cm). This implies that there is a very large difference in the spacing between the quantized values of the wavevectors in the directions perpendicular, k_{\perp} , and parallel, k_{\parallel} , to the tube axis. In this section, we will regard k_{\parallel} to be effectively continuous (infinitely long NTs) and consider only the quantization effects due to the small diameter of NTs (section 2.3 will cover the quantum effects associated to finite length CNTs, which constitute the actual subject of this thesis).

By imposing periodic boundary conditions around the NT circumference we obtain the allowed values of k_{\perp} :

$$\mathbf{C} \cdot \mathbf{k} = \pi d k_{\perp} = 2\pi j \quad (2.3)$$

where d is the NT diameter and j is an integer number. The small diameter of CNTs makes the spacing in k_{\perp} to be rather large ($\Delta k_{\perp} = 2/d$), resulting in strong observable effects even at room temperature. The quantization of k_{\perp} leads to a set of 1-dimensional subbands in the longitudinal direction (intersection of vertical planes parallel to k_{\parallel} with the band structure of graphene). These are shown in Fig. 2.6b. The electronic states closest to the Fermi energy lie in the subbands closest to the K points. One of the most remarkable properties of

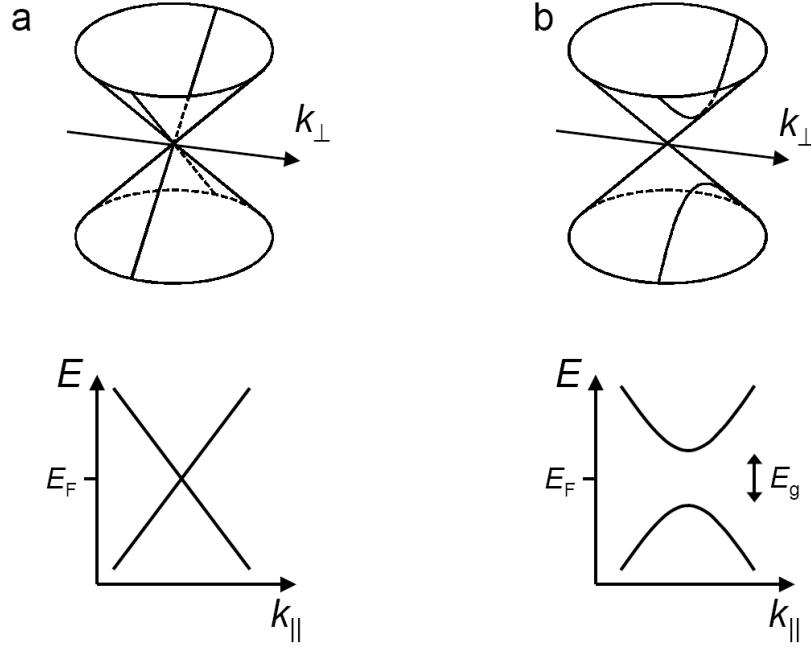


Figure 2.7: Low energy band diagrams for carbon nanotubes around the \mathbf{K}_1 point. **a**, For $p = 0$, there is an allowed value of k_{\perp} whose subband passes through \mathbf{K}_1 , resulting in a metallic nanotube and band structure. **b**, For $p = 1$, the closest subband to \mathbf{K}_1 misses it by $\Delta k_{\perp} = 2/3d$, resulting in a semiconducting nanotube with band gap E_g . In both figures, E_F refers to the value of the Fermi energy in graphene.

CNTs becomes apparent now: if a subband passes exactly through the middle of a dispersion cone, then the nanotube will be metallic. If not, then there will be an energy gap between valence and conduction bands and the nanotube will be a semiconductor. To first approximation, all nanotubes fall into one of these categories: either they are metallic or semiconductors. In fact, for a given (n, m) nanotube, we can calculate $n - m = 3q + p$, where q is an integer and p is -1, 0 or +1 [13]. If $p = 0$, then there is an allowed value of k_{\perp} that intercepts the K points, and the nanotube is metallic. The slope of the dispersion cones gives the Fermi velocity in metallic nanotubes: $dE/dk = \hbar v_F$, with $v_F \sim 8 \cdot 10^5$ m/s [14]. For $p = \pm 1$, there is no allowed value of k_{\perp} intercepting the K points, resulting then in a semiconducting nanotube (see Fig. 2.7). The closest k_{\perp} to the K points misses them by $\Delta k_{\perp} = \pm 2/3d$, for $p = \pm 1$, respectively. This means that the value of the band gap is: $E_g = 2(dE/dk)\Delta k_{\perp} = 2\gamma_0 a/(\sqrt{3}d) \sim 0.8$ eV/d[nm], independent of chiral angle. Of all carbon nanotubes, approximately 1/3 are metallic and 2/3 are semiconducting (see Fig. 2.8).

It is quite remarkable that carbon nanotubes can be metallic or semiconducting depending on chirality and diameter, despite the fact that there is no

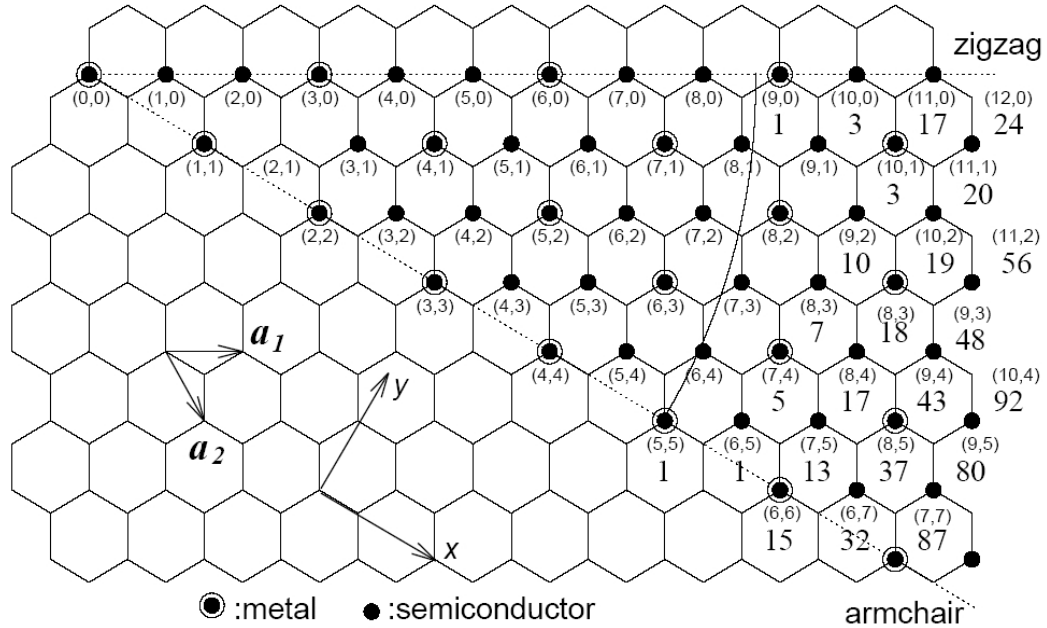


Figure 2.8: Possible nanotube wrapping vectors, characterized by (n, m) , with $n > m$. Black dots indicate semiconducting nanotubes and circled dots indicate metallic nanotubes (from ref. [13]).

difference in the local chemical bonding between the carbon atoms in the different tubes. This fact results from an elegant combination of quantum mechanics and the peculiar band structure of graphene.

Remarks on the band structure of carbon nanotubes

In the previous section we have seen how the band structure of CNTs can be derived from the band structure of graphene. Here we would like to emphasize some aspects of the CNT band structure which will be especially relevant for the experiments described in this thesis.

The low energy band structure of carbon nanotubes is doubly degenerate (at zero magnetic field). By this we mean that at a given energy there are two different orbital electronic states that can contribute to transport (there is also an additional two-fold degeneracy due to spin). This degeneracy has been interpreted in a semiclassical fashion as the degeneracy between clockwise (CW) and counter-clockwise (CCW) propagating electrons along the nanotube circumference [15]. Within this picture, CW and CCW electrons in CNTs have opposite classical magnetic moments associated with them, which, in the absence of a magnetic field, are degenerate (also opposite spin states are degenerate at

zero magnetic field). This orbital degeneracy plays a fundamental role in the transport properties of carbon nanotubes, as we will show in chapters 4 to 6.

In the presence of a magnetic field parallel to the NT axis, B_{\parallel} , the quantization condition (eq. 2.3) is modified:

$$\mathbf{C} \cdot \mathbf{k} + 2\pi\Phi/\Phi_o = 2\pi j \quad (2.4)$$

where $2\pi\Phi/\Phi_o$ is the Aharonov-Bohm phase acquired by the electrons while travelling around the nanotube circumference ($\Phi = B_{\parallel}\pi d^2/4$ is the magnetic flux threading the tube and $\Phi_o = h/e$ is the flux quantum). This means that the allowed k_{\perp} values are displaced with respect to their original positions by an amount $k_{\perp}(B_{\parallel}) - k_{\perp}(B_{\parallel} = 0) = \pi e B_{\parallel} d/2h$. This has very profound consequences for the electronic properties of nanotubes. Let's consider first the case of a metallic nanotube, for which the subbands pass through the cone vertices at zero field (Fig. 2.9a). The effect of B_{\parallel} is to shift the subbands away from the cone vertices, thus opening a bandgap (Fig. 2.9b). So we can transform a metallic nanotube into a semiconducting nanotube by means of a magnetic field, and back to a metallic nanotube once $\Phi = \Phi_o$. This is a very remarkable consequence of the quantum properties of carbon nanotubes. The magnetic field necessary to complete the whole cycle is very large for a small diameter nanotube (~ 5300 T for $d = 1$ nm), but it is accessible in the case of large multiwall nanotubes ($B_{\parallel} \sim 8T$ for $d \sim 25$ nm), as it has been recently shown [16]. Note that a finite B_{\parallel} doesn't break the subband degeneracy for metallic NTs, since the two subbands passing through the \mathbf{K}_1 and \mathbf{K}_2 points shift in the same direction.

The case of semiconducting nanotubes is perhaps more intriguing. Since $\mathbf{K}_2 = -\mathbf{K}_1$, the two lowest energy orbital subbands are on opposite sides of the cones at \mathbf{K}_1 and \mathbf{K}_2 (Fig. 2.9c). Because B_{\parallel} shifts both subbands in the same direction, one subband gets closer to the \mathbf{K}_2 point, and its band gap decreases, while the other subband shifts away from the \mathbf{K}_1 point, thereby increasing its band gap (Fig. 2.9d). The magnitude of this band gap change can be easily calculated:

$$\left| \frac{dE_g}{dB_{\parallel}} \right| = 2 \frac{dE_g}{dk_{\perp}} \frac{dk_{\perp}}{dB_{\parallel}} = 2\hbar v_F \frac{dk_{\perp}}{dB_{\parallel}} = 2 \frac{ev_F d}{4} \quad (2.5)$$

which is about 0.4 meV/T for $d = 1$ nm. This band gap change is small compared to typical band gaps of nanotubes (\sim hundreds of meV), but it is quite large compared to other energy scales routinely observed in low temperature transport experiments, such as the Zeeman splitting (~ 0.11 meV/T for g -factor $g = 2$).

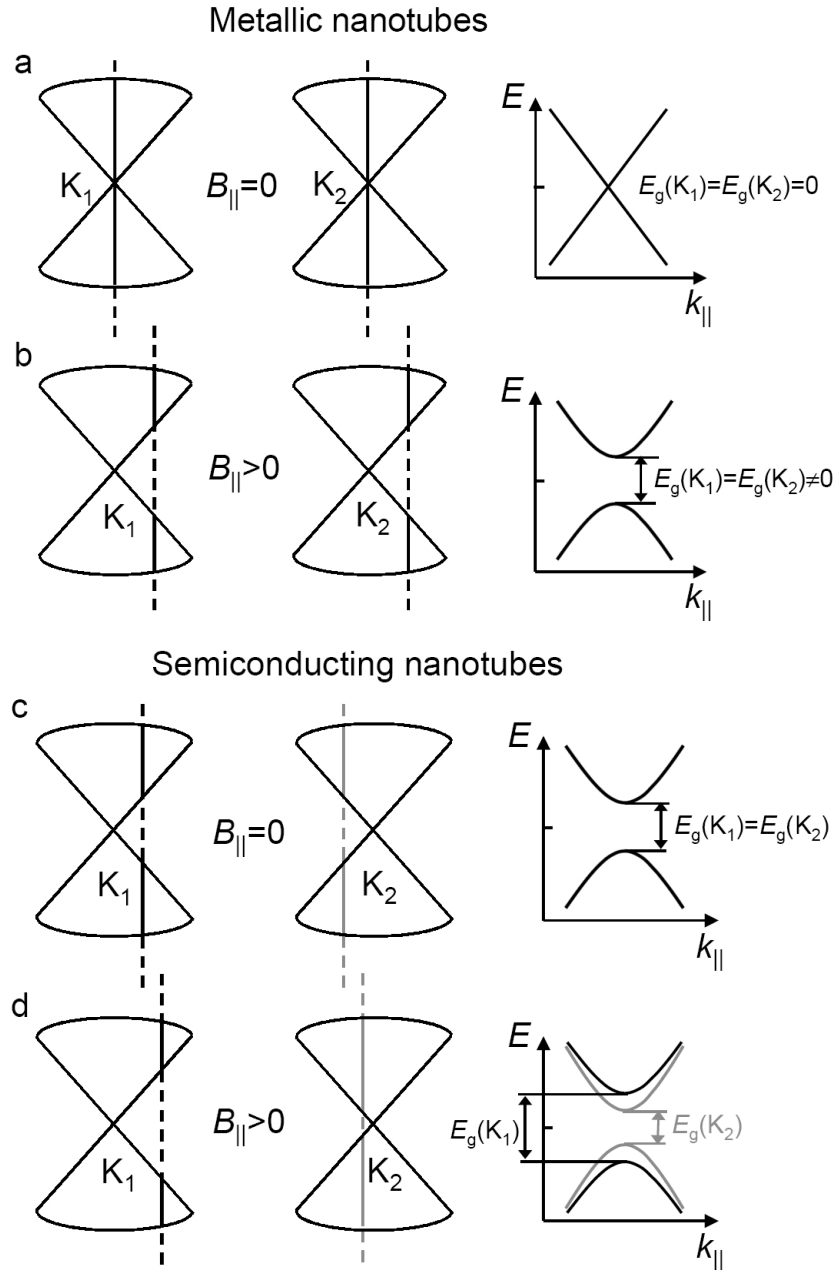


Figure 2.9: Changes in the nanotube band structure by an applied parallel magnetic field, B_{\parallel} (see main text). The vertical lines represent allowed k_{\perp} values intercepting the dispersion cones at \mathbf{K}_1 and \mathbf{K}_2 . **a, b**, A metallic nanotube is transformed into a semiconducting nanotube. **c, d**, Subband splitting in a semiconducting nanotube.

The subband splitting can be thought off as an orbital splitting due to electrons with opposite orbital magnetic moments, analogous to the Zeeman splitting for electrons with opposite spin magnetic moment. The quantity $ev_F d/4$ corre-

sponds to the orbital magnetic moment of an electron moving in a circumference of diameter d at a speed v_F [15]. Eventually, by increasing B_{\parallel} , we can convert a semiconducting nanotube into a metallic one (although this time only one subband will be metallic). The consequences of a parallel magnetic field on the transport through small band gap semiconducting NTs has been recently studied by Minot and coworkers [15]. In chapters 5 and 6 we too investigate these orbital magnetic effects and find that the interplay between the orbital magnetic moment and the spin magnetic moment gives rise to very interesting physics.

One last aspect of the nanotube band structure that we want to comment on relates to the classification of nanotubes as metals and semiconductors. We have already mentioned in the previous paragraph ‘small band gap nanotubes’. What do we mean by this? It turns out that not all metallic nanotubes are true metals. Some nanotubes which are metallic according to the quantization of the graphene band structure mentioned before, actually become small band gap semiconductors when a more realistic model is taken into account. This band gap (typically \sim tens of meV) is small compared to the usual NT band gaps (\sim eV), and has a smaller effect on the NT conductance properties at room temperature. These small band gaps can be intrinsic, such as curvature induced [17, 18] or inter-shell interactions in multiwall tubes [19], or be due to external perturbations, such as axial strain [20, 21] or twist [22]. While these small band gaps are often found in transport experiments [23, 15], it is in practice quite difficult to precisely determine their origin. Nevertheless, small band gap nanotubes can be very useful to study the magnetic effects mentioned above, because the degeneracy between the orbital subbands survives even in the presence of these perturbations.

2.2 Quantum dots

Quantum dots are essentially ‘small’ structures with a discrete set of ‘zero-dimensional’ energy states where we can place electrons. Now, quantum mechanics tells us that electrons in a finite size object have a discrete energy spectrum, so, in an experiment, a small structure behaves like a quantum dot (QD) if the separation between the energy levels is observable at the temperature we are working at. For most nanostructures this involves working at temperatures below a few Kelvin. Of course the lifetime of the energy levels must be long enough to be able to observe them too, and this means that the electrons must be (at least partially) confined. Because a quantum dot is such a general kind of system, there exist QDs of many different sizes and materials: for instance single molecules, metallic nanoparticles, semiconductor self-assembled quantum

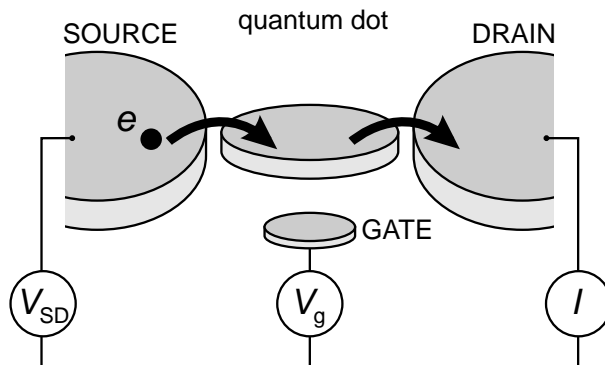


Figure 2.10: Schematic picture of a quantum dot. The quantum dot (represented by a disk) is connected to source and drain contacts via tunnel barriers, allowing the current through the device, I , to be measured in response to a bias voltage, V_{SD} and a gate voltage, V_g .

dots and nanocrystals, lateral or vertical dots in semiconductor heterostructures, semiconducting nanowires or carbon nanotubes. Quantum dots are mostly studied by means of optical spectroscopy or electronic transport techniques. In this thesis we have used the latter to study quantum dots defined in short segments of carbon nanotubes. But before discussing CNT QDs, we present here a general description of electronic transport through quantum dots.

In order to measure electronic transport through a quantum dot, this must be attached to a source and drain reservoirs, with which particles can be exchanged. (see Fig. 2.10). By attaching current and voltage probes to these reservoirs, we can measure the electronic properties of the dot. The QD is also coupled capacitively to one or more ‘gate’ electrodes, which can be used to tune the electrostatic potential of the dot with respect to the reservoirs.

A simple, yet very useful model to understand electronic transport through QDs is the constant interaction (CI) model [24]. This model makes two important assumptions. First, the Coulomb interactions among electrons in the dot are captured by a single constant capacitance, C . This is the total capacitance to the outside world, i.e. $C = C_S + C_D + C_g$, where C_S is the capacitance to the source, C_D that to the drain, and C_g to the gate. Second, the discrete energy spectrum is independent of the number of electrons on the dot. Under these assumptions the total energy of a N -electron dot with the source-drain voltage, V_{SD} , applied to the source (and the drain grounded), is given by

$$U(N) = \frac{[-|e|(N - N_0) + C_S V_{SD} + C_g V_g]^2}{2C} + \sum_{n=1}^N E_n(B) \quad (2.6)$$

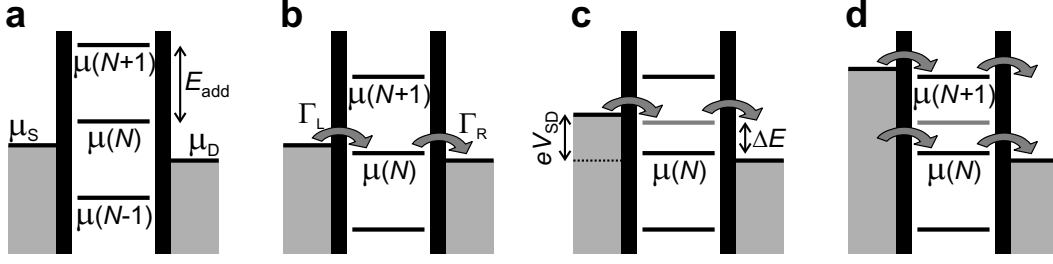


Figure 2.11: Schematic diagrams of the electrochemical potential of the quantum dot for different electron numbers. **a**, No level falls within the bias window between μ_S and μ_D , so the electron number is fixed at $N - 1$ due to Coulomb blockade. **b**, The $\mu(N)$ level is aligned, so the number of electrons can alternate between N and $N - 1$, resulting in a single-electron tunneling current. The magnitude of the current depends on the tunnel rate between the dot and the reservoir on the left, Γ_L , and on the right, Γ_R . **c**, Both the ground-state transition between $N - 1$ and N electrons (black line), as well as the transition to an N -electron excited state (gray line) fall within the bias window and can thus be used for transport (though not at the same time, due to Coulomb blockade). This results in a current that is different from the situation in **b**. **d**, The bias window is so large that the number of electrons can alternate between $N - 1$, N and $N + 1$, i.e. two electrons can tunnel onto the dot at the same time.

where $-|e|$ is the electron charge and N_0 the number of electrons in the dot at zero gate voltage. The terms $C_S V_{SD}$ and $C_g V_g$ can change continuously and represent the charge on the dot that is induced by the bias voltage (through the capacitance C_S) and by the gate voltage V_g (through the capacitance C_g), respectively. The last term of Eq. 2.6 is a sum over the occupied single-particle energy levels $E_n(B)$, which are separated by an energy $\Delta E_n = E_n - E_{n-1}$. These energy levels depend on the characteristics of the confinement potential. Note that, within the CI model, only these single-particle states depend on magnetic field, B .

To describe transport experiments, it is often more convenient to use the electrochemical potential, μ . This is defined as the minimum energy required to add an electron to the quantum dot:

$$\begin{aligned} \mu(N) &\equiv U(N) - U(N - 1) = \\ &= (N - N_0 - \frac{1}{2})E_C - \frac{E_C}{|e|}(C_S V_{SD} + C_g V_g) + E_N \end{aligned} \quad (2.7)$$

where $E_C = e^2/C$ is the charging energy. The electrochemical potential for different electron numbers N is shown in Fig. 2.11a. The discrete levels are spaced by the so-called addition energy, $E_{add}(N)$:

$$E_{add}(N) = \mu(N + 1) - \mu(N) = E_C + \Delta E. \quad (2.8)$$

The addition energy consists of a purely electrostatic part, the charging energy E_C , plus the energy spacing between two discrete quantum levels, ΔE . Note that ΔE can be zero, when two consecutive electrons are added to the same spin-degenerate level or if there are additional degeneracies present. Of course, for transport to occur, energy conservation needs to be satisfied. This is the case when an electrochemical potential level lies within the ‘bias window’ between the electrochemical potential (Fermi energy) of the source (μ_S) and the drain (μ_D), i.e. $\mu_S \geq \mu \geq \mu_D$ with $-|e|V_{SD} = \mu_S - \mu_D$. Only then can an electron tunnel from the source onto the dot, and then tunnel off to the drain without losing or gaining energy. The important point to realize is that since the dot is very small, it has a very small capacitance and therefore a large charging energy – for typical dots $E_C \approx$ a few meV. If the electrochemical potential levels are as shown in Fig. 2.11a, this energy is not available (at low temperatures and small bias voltage). So, the number of electrons on the dot remains fixed and no current flows through the dot. This is known as Coulomb blockade. The charging energy becomes important when it exceeds the thermal energy, $k_B T$, and when the barriers are sufficiently opaque such that the electrons are located either in the reservoirs or in the dot. The latter condition implies that quantum fluctuations in the number of electrons on the dot must be sufficiently small. A lower bound for the tunnel resistances R_t of the barriers can be found from the Heisenberg uncertainty principle. The typical time Δt to charge or discharge the dot is given by the RC -time. This yields $\Delta E \Delta t = (e^2/C)R_t C > h$. Hence, R_t should be much larger than the quantum resistance h/e^2 to sufficiently reduce the uncertainty in the energy.

It turns out that there are many ways to lift the Coulomb blockade. First, we can change the voltage applied to the gate electrode. This changes the electrostatic potential of the dot with respect to that of the reservoirs, shifting the whole ‘ladder’ of electrochemical potential levels up or down. When a level falls within the bias window, the current through the device is switched on. In Fig. 2.11b $\mu(N)$ is aligned, so the electron number alternates between $N - 1$ and N . This means that the N th electron can tunnel onto the dot from the source, but only after it tunnels off to the drain can another electron come onto the dot again from the source. This cycle is known as single-electron tunneling.

By sweeping the gate voltage and measuring the current, we obtain a trace as shown in Fig. 2.12a. At the positions of the peaks, an electrochemical potential level is aligned with the source and drain and a single-electron tunneling current

flows. In the valleys between the peaks, the number of electrons on the dot is fixed due to Coulomb blockade. By tuning the gate voltage from one valley to the next one, the number of electrons on the dot can be precisely controlled. The distance between the peaks corresponds to $E_C + \Delta E$, and can therefore give information about the energy spectrum of the dot.

A second way to lift Coulomb blockade is by changing the source-drain voltage, V_{SD} (see Fig. 2.11c). (In general, we keep the drain potential fixed, and change only the source potential.) This increases the bias window and also ‘drags’ the electrochemical potential of the dot along, due to the capacitive coupling to the source. Again, a current can flow only when an electrochemical potential level falls within the bias window. By increasing V_{SD} until both the ground state as well as an excited state transition fall within the bias window, an electron can choose to tunnel not only through the ground state, but also through an excited state of the N -electron dot. This is visible as a change in the total current. In this way, we can perform excited-state spectroscopy.

Usually, we measure the current or differential conductance while sweeping the bias voltage, for a series of different values of the gate voltage. Such a measurement is shown schematically in Fig. 2.12b. Inside the diamond-shaped region, the number of electrons is fixed due to Coulomb blockade, and no current flows. Outside the diamonds, Coulomb blockade is lifted and single-electron tunneling can take place (or for larger bias voltages even double-electron tunneling is possible, see Fig. 2.11d). Excited states are revealed as changes in the current, i.e. as peaks or dips in the differential conductance. From such a ‘Coulomb

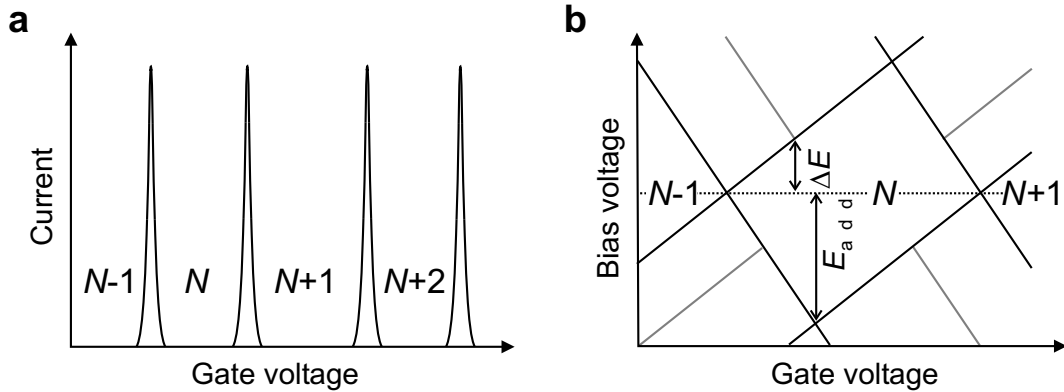


Figure 2.12: Transport through a quantum dot. **a**, Coulomb peaks in current versus gate voltage in the linear-response regime. **b**, Coulomb diamonds in differential conductance, dI/dV_{SD} , versus V_{SD} and V_g , up to large bias. The edges of the diamond-shaped regions (black) correspond to the onset of current. Diagonal lines emanating from the diamonds (gray) indicate the onset of transport through excited states.

diamond' the excited-state energy as well as the charging energy can be read off directly.

The simple model described above explains successfully how quantization of charge and energy leads to effects like Coulomb blockade and Coulomb oscillations. Nevertheless, it is too simplified in many respects. For instance, the model considers only first-order tunneling processes, in which an electron tunnels first from one reservoir onto the dot, and then from the dot to the other reservoir. But when the tunnel rate between the dot and the leads, Γ , is increased, higher-order tunneling via virtual intermediate states becomes important. Such processes, which are known as 'cotunneling', can be very useful in performing detailed spectroscopy, as shown in chapter 5, for example. Furthermore, the simple model does not take into account the spin of the electrons, thereby excluding for instance exchange effects. Also the Kondo effect, an interaction between the spin on the dot and the spins of the electrons in the reservoir, cannot be accounted for. A special type of Kondo effect is explored in chapter 6.

2.3 Carbon nanotube quantum dots

In section 2.1 we described the basic electronic properties of infinitely long nanotubes. Due to the quantization of momentum in the transversal direction, CNTs are usually treated as 1D objects. In an actual experiment, however, we measure NTs of finite length and, we can expect therefore that quantum effects associated with this finite length will be observable if we measure short enough NTs and cool them to sufficiently low temperature. Under these conditions, the 0D nature of the NT electronic states will be evident and CNTs will behave as quantum dots.

When two metallic electrodes are deposited on top of a CNT, tunnel barriers develop naturally at the NT-metal interfaces. The separation between the electrodes, L , determines then the QD length (see Fig. 2.13). A finite L results in quantized energy levels in the longitudinal direction, with an energy level separation ΔE . The strength of the NT-metal tunnel barriers determines the degree of confinement of electrons in the NT QD. For very opaque barriers, the tunnel rate between the QD and the reservoirs, Γ , is very small, resulting in a large lifetime of the electrons in the QD (or small energy broadening). If the barriers become more transparent (i.e., more transmissive), the energy levels get 'T-broadened'. For any QD, $h\Gamma < \Delta E$, in order to be able to observe clearly the discreteness of the energy spectrum. Depending on the ratio between the lifetime broadening and the charging energy, we can distinguish three different QD regimes (with

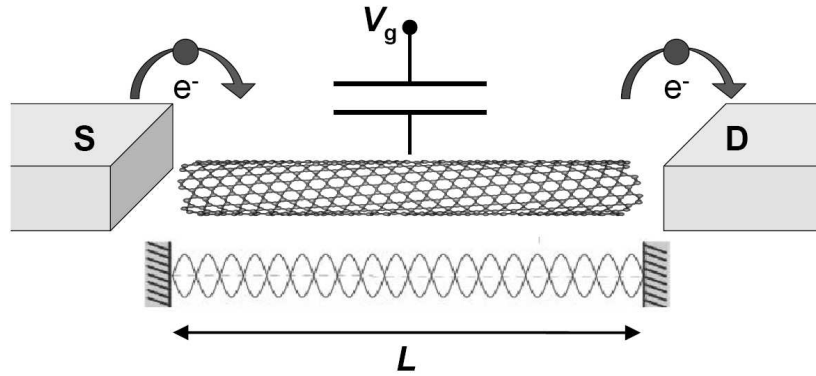


Figure 2.13: Schematic picture of a carbon nanotube quantum dot. Two metal electrodes, source (S) and drain (D), separated by a distance L are deposited on top of the tube. The QD is formed in the segment of nanotube in between the electrodes, leading to a quantized energy spectrum in the longitudinal direction. The NT is capacitatively coupled to a gate electrode (usually the back gate plane of the silicon substrate).

different typical phenomena associated with them):

1. $\hbar\Gamma \ll E_C$ (Closed QD regime) \longrightarrow Charging effects dominate transport (Coulomb blockade).
2. $\hbar\Gamma \leq E_C$ (Intermediate transparency regime) \longrightarrow Charging effects important, but higher-order tunneling processes significant too (cotunneling and Kondo effect).
3. $\hbar\Gamma \gg E_C$ (Open QD regime) \longrightarrow Quantum interference of non-interacting electrons (Fabry-Perot like interference).

The experiments described in this thesis explore these three regimes (chapters 3 and 8, 5 and 6, and 7, respectively).

The coupling between the NT and the metal leads depends on the contact material, NT diameter and metallic/semiconducting character of the NT. Certain materials, such as Ti or Au, make (generally) good contact to nanotubes (especially metallic ones). Others, like Al make pretty bad contact. It has recently been shown that Pd and Rh are very good materials to contact NTs [25, 26, 27]. The larger the diameter, the lower the contact resistance is (on average). It is also easier to contact metallic NTs than semiconducting ones because the latter typically develop a Schottky barrier at the NT-metal interface. Despite these guidelines, it is still not possible to obtain a desired contact resistance when depositing metal on top of a CNT. Usually a number of NT devices are fabricated

on a chip and we choose among them depending on the type of experiment to be performed.

If we assume hard wall boundary conditions, then the quantized values of the wavevector in the longitudinal direction, $k_{||}$, are separated by $\Delta k_{||} = \pi/L$. In the case of metallic nanotubes this leads to an energy level spacing, ΔE , given by

$$\Delta E = \frac{dE}{dk_{||}} \Delta k_{||} = \frac{hv_F}{2L} \quad (2.9)$$

It turns out that due to the high Fermi velocity in metallic CNTs, ΔE is actually quite large ($\Delta E \sim 1.7 \text{ meV}/L[\mu\text{m}]$), and, for typical L (\sim few hundreds of nm), the quantum behaviour of CNTs can be observed even at temperatures of a few K. Another interesting consequence of eq. 2.9 is that the energy level spacing in CNT QDs is constant, i.e., independent of the number of electrons, N . This doesn't occur in other types of QDs, such as those defined in 2-dimensional electron gases in semiconductor heterostructures, where the energy level spacing becomes very small as the QDs are filled with more and more e^- , and also the spectrum becomes more complicated as N increases. A NT QD can contain thousands of e^- and still have a relatively simple spectrum. Because of their small size, nanotubes in the closed QD regime have also rather large charging energies (typically $\sim 5\text{-}20 \text{ meV}$). These large charging energies, large energy level spacings and the simplicity of the spectrum make metallic NTs a very suitable system to study QD physics.

The constant interaction model together with eq. 2.9 for the energy spectrum is a good starting point to analyze measurements on NT QDs in the Coulomb blockade regime [6, 7]. However, more complete models are necessary to explain the spectrum of NT QDs, and especially the excitation spectrum energies. The CI model doesn't take into account exchange effects, for example, and eq. 2.9 doesn't take into account the double orbital degeneracy of the NT band structure. In chapter 4, a still simple, but more elaborated model, which takes into account these effects [28], is used to explain the spectrum of high quality metallic NT QDs.

Semiconducting CNTs are a complete different story. Chapter 3 reports the first observation of QD behaviour in a large band gap semiconducting NT QD. Theory indicates that semiconducting nanotubes are more susceptible to disorder than metallic ones [29, 30]. When a semiconducting NT device is cooled down to low temperature, disorder typically divides the NT into multiple islands, preventing the formation of a single, well-defined QD. In chapter 3 we show that the addition energy spectrum of semiconducting CNTs cannot be described by

the models mentioned above (at least near the band gap). To start with, the charging energy varies significantly (although smoothly) with N , which means that the CI model is not valid. Also the energy dispersion relation is not linear, but quadratic, so eq. 2.9 is not applicable. Moreover, a hard wall potential is not appropriate to describe electron confinement in semiconducting NTs, because of the weak screening due to the lack of charge carriers near the band gap and the 1-dimensionality of NTs. Altogether, the spectrum of semiconducting nanotubes is not understood, and requires further experimental and theoretical study.

2.4 Kondo effect

The only transport mechanism we have described in section 2.2, was sequential tunneling. This first-order tunneling mechanism gives rise to a current only at the Coulomb peaks, with the number of electrons on the dot being fixed between the peaks. This description is quite accurate for a dot with very opaque tunnel barriers. However, when the dot is opened, so that the resistance of the tunnel barriers becomes comparable to the resistance quantum, $R_Q \equiv h/e^2 = 25.8 \text{ k}\Omega$, higher-order tunneling processes have to be taken into account. These lead to quantum fluctuations in the electron number, even when the dot is in the Coulomb blockade regime.

An example of such a higher-order tunneling event is shown in Fig. 2.14a. Energy conservation forbids the number of electrons to change, as this would cost an energy of order $E_C/2$. Nevertheless, an electron can tunnel off the dot, leaving it temporarily in a classically forbidden ‘virtual’ state (middle diagram in Fig. 2.14a). This is allowed by virtue of Heisenberg’s energy-time uncertainty principle, as long as another electron tunnels back onto the dot immediately, so that the system returns the energy it borrowed. The final state then has the same energy as the initial one, but one electron has been transported through the dot. This process is known as (elastic) ‘cotunneling’ [31].

If the electron spin is taken into account, then events such as the one shown in Fig. 2.14b can take place. Initially, the dot has a net spin up, but after the virtual intermediate state, the dot spin is flipped. Unexpectedly, it turns out that by adding many spin-flips events of higher orders coherently, the spin-flip rate diverges. The spin on the dot and the electron spins in the reservoirs are no longer separate, they have become *entangled*. The result is the appearance of a new ground state of the system as a whole – a spin singlet. The spin on the dot is thus completely screened by the electron spins in the reservoirs.

This is completely analogous to the well-known Kondo effect, which occurs in

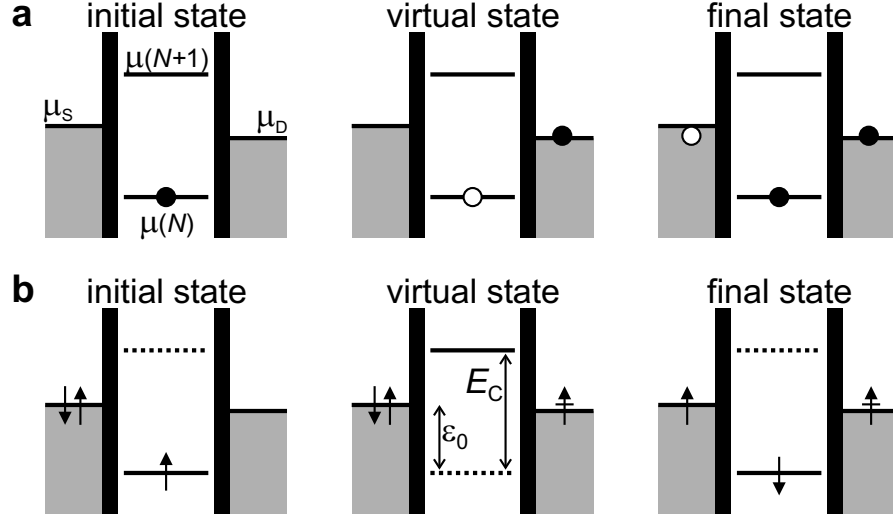


Figure 2.14: Higher-order tunneling events overcoming Coulomb blockade. **a**, Elastic cotunneling. The N th electron on the dot jumps to the drain to be immediately replaced by an electron from the source. Due to the small bias, such events give rise to a net current. **b**, Spin-flip cotunneling. The spin-up electron jumps out of the dot to be immediately replaced by a spin-down electron. Many such higher-order spin-flip events together build up a spin singlet state consisting of electron spins in the reservoirs and the spin on the dot. Thus, the spin on the dot is screened.

metals containing a small concentration of magnetic impurities (e.g. cobalt). It was observed already in the 1930's [32] that below a certain temperature (typically about 10 K), the resistance of such metals would grow. This anomalous behaviour was not understood, until in 1964 the Japanese theorist Jun Kondo explained it as screening of the impurity spins by the spins of the conduction electrons in the host metal [33]. The screening is accompanied by a scattering resonance at the Fermi energy of the metal, resulting in an increased resistance. In 1988, it was realized that the same Kondo effect should occur (at low temperatures) in quantum dots with a net spin [35, 36]. However, in quantum dots the scattering resonance is manifested as an increased probability for scattering from the source to the drain reservoir, i.e. as an increased conductance.

The Kondo effect appears below the so-called Kondo temperature, T_K , which corresponds to the binding energy of the Kondo singlet state. It can be expressed in terms of the dot parameters as

$$T_K = \frac{\sqrt{h\Gamma E_C}}{2k_B} e^{\pi\varepsilon_0(\varepsilon_0 + E_C)/h\Gamma E_C} \quad (2.10)$$

where Γ is the tunnel rate to and from the dot, and ε_0 is the energy level on the dot relative to the Fermi energy of the reservoirs. The great advantage of using

quantum dots, in general, to study the Kondo effect, is that they allow these parameters to be tuned *in situ* [34]. In the case of carbon nanotubes, the double orbital degeneracy results in new and exotic regimes of the Kondo effect, as is demonstrated in chapter 6.

The main characteristics of the Kondo effect in transport through a quantum dot are schematically depicted in Fig. 2.15. For an odd number of electrons on the dot, the total spin S is necessarily non-zero, and in the simplest case $S = 1/2$. However, for an even electron number on the dot – again in the simplest scenario – all spins are paired, so that $S = 0$ and the Kondo effect is not expected to occur. This ‘even-odd-asymmetry’ results in the temperature dependence of the linear conductance, G , as shown in Fig. 2.15a. In the ‘odd’ or ‘Kondo’ valleys the conductance increases as the temperature is lowered, due to the Kondo effect. In the ‘even’ valleys, on the other hand, the conductance decreases, due to a decrease of thermally excited transport through the dot.

The temperature dependence of the conductance in the middle of the Kondo valleys is shown in Fig. 2.15b. The conductance increases logarithmically with decreasing temperature [35], and saturates at a value $2e^2/h$ at the lowest temperatures [36, 37]. Although the dot has two tunnel barriers and the charging energy tends to block electrons from tunneling on or off, the Kondo effect enables electrons to pass unhindered through the dot. This complete transparency of the dot is known as the ‘unitary limit’ of conductance [38]. The Kondo resonance at the Fermi energy of the reservoirs is manifested as a zero-bias resonance in

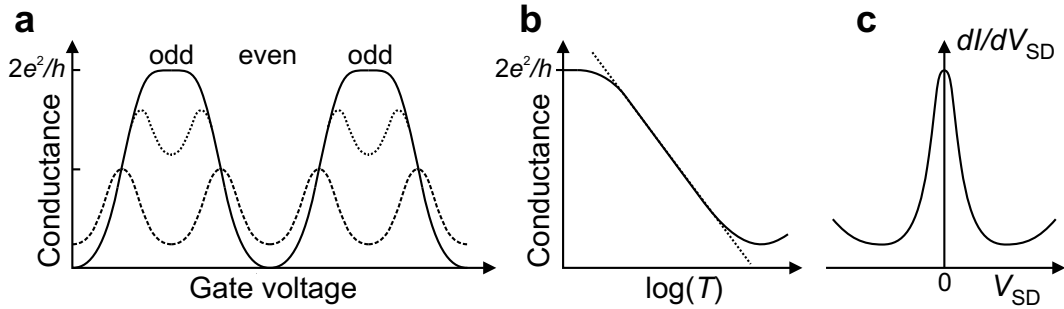


Figure 2.15: Schematic representation of the main characteristics of the Kondo effect in electron transport through a quantum dot. **a**, Linear conductance versus gate voltage, for $T \ll T_K$ (solid line), $T \lesssim T_K$ (dotted line), and $T \gg T_K$ (dashed line). The Kondo effect only occurs for odd electron number, resulting in an odd-even asymmetry between the different Coulomb valleys. **b**, In the odd (‘Kondo’) valleys the conductance increases logarithmically upon lowering the temperature, and saturates at $2e^2/h$. **c**, The Kondo resonance leads to a zero-bias resonance in the differential conductance, dI/dV_{SD} , versus bias voltage, V_{SD} .

the differential conductance, dI/dV_{SD} , versus V_{SD} , as shown in Fig. 2.15c. The full width at half maximum of this resonance gives an estimate of the Kondo temperature.

2.5 Device fabrication

It is quite difficult to overestimate the importance of a good sample fabrication procedure for the success of a physics experiment. This is, perhaps, even more true in nanoscience, where the intrinsically small size of the devices, makes them very sensitive to external influences. The fabrication of the nanotube devices used in the experiments described in this thesis requires state of the art nanofabrication facilities and techniques. Roughly speaking, the fabrication process can be divided in four parts: (i) fabrication of markers; (ii) nanotube deposition/growth; (iii) nanotube location and electrode fabrication, and (iv) room temperature characterization and sample bonding. Although each of these steps is not ‘*per se*’ difficult (however tedious it may be), so many things can go wrong at any of them that, at the end, the fabrication of a good device requires a considerable amount of careful concentration, practice, patience and, why not admit it, good luck.

Fabrication of markers

In all experiments the nanotubes are grown/deposited on top of oxidized silicon substrates. The Si-substrates are highly doped (p-doped in our case) so that they remain conductive at low temperatures and can serve as a backgate in our devices. The thickness of the thermally grown oxide is typically ~ 250 nm, and isolates the devices from the back gate. A set of markers is necessary to later locate the position of the nanotubes and for the fabrication of the electrodes. These include a set of electron beam lithography alignment markers (e-beam markers) and atomic force microscopy (AFM) markers. The patterning of these markers requires one e-beam lithography ‘cycle’ (Fig. 2.16), which consists of spinning a double layer of e-beam resist, e-beam lithography, development, metal evaporation and lift-off. The bottom layer of resist (poly-methyl methacrylate (PMMA) 350K 3% in chlorobenzene) is thicker and more sensitive to e-beam radiation, serves as a spacer and ensures a proper lift-off. The top resist layer (PMMA 950K 2% in chlorobenzene) is less sensitive and serves as the actual mask for metal evaporation. Once the resist is spun, a pattern is ‘written’ by irradiating the PMMA with a beam of electrons, which breaks the bonds in the polymer.

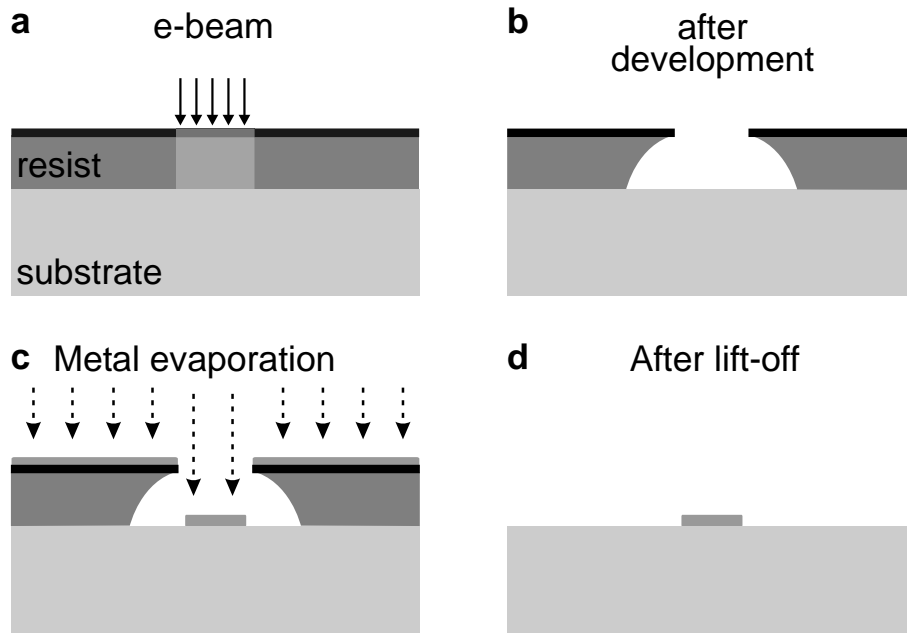


Figure 2.16: Schematic electron beam lithography cycle. **a**, Double layer of organic resist is spun on a substrate and a predefined pattern is irradiated with a beam of electrons. **b**, After development, an opening is left in the resist. **c**, Metal is evaporated on top of the substrate + remaining resist. **d**, The remaining resist is removed and the metal is left at the predefined positions.

The ‘exposed’ resist is removed from the substrate by immersing the sample in a developer (a 1:3 solution of methyl isobutyl ketone (MIBK) and iso-propyl alcohol (IPA)). Then the substrate is placed in an e-beam evaporator, where (Cr or Ti)/Pt (5/70 nm) is evaporated. Chromium or titanium are used as sticking layers for the platinum. We use Pt for the markers because they can withstand, without severe deformation, the high temperatures (~ 900 °C) during nanotube growth. After metal evaporation, the unexposed resist and excess metal is removed by immersing the sample in hot acetone (~ 55 °C). We have observed that further immersing the sample for ~ 10 minutes in dichloroethane (DCE) helps removing small amounts of PMMA residue left during the lift-off process. DCE should not be used with certain metals (such as Al) because it can react with them, and it should be handled with special care because of its high toxicity. After lift-off, we are left with a substrate which contains e-beam markers, AFM markers, as well as a series of optical and numerical markers to help handling and tagging of samples.

Carbon nanotube deposition/growth

We have used two methods to place nanotubes on the substrates: direct deposition from a solution, and chemical vapour deposition (CVD) growth. For the first one we put a small amount of carbon nanotube material in a bottle containing DCE and sonicate until the nanotube material has disentangled into separate nanotubes (typically ~ 30 min to 1 hour). Then a few droplets of solution are placed on a substrate and blown-dried with nitrogen. This process leaves nanotubes all over the substrate. It is easy and fast, but it has certain disadvantages, such as tuning the concentration of nanotubes, the fact that many times the nanotubes appear in ropes and not individually, and the random location in the deposition. Besides we have also noticed that it is harder to make good contact to deposited NTs than to CVD-grown tubes. For these reasons, most of our last experiments have been performed with carbon nanotubes grown by CVD. For the catalyst, 40 mg of $\text{Fe}(\text{NO}_3)_3 \cdot 9\text{H}_2\text{O}$, 2 mg of $\text{MoO}_2(\text{acac})_2$ (Sigma Aldrich), and 30 mg of Alumina nanoparticles (Degussa Aluminum Oxide C) are mixed in 30 ml of methanol and sonicated for ~ 1 hr. The resulting liquid catalyst is deposited onto the substrate with $0.5 \mu\text{m}^2$ openings in the PMMA resist (patterned on specific known locations by e-beam lithography) and blown dry. After lift-off in acetone, the substrate with patterned catalyst is placed in a 1-inch quartz tube furnace and the CVD is carried out at 900°C with 700 sccm H_2 , 520 sccm CH_4 for 10 min. Argon is flown during heating up and cooling down. The methane and hydrogen flows have been optimized to obtain long and clean nanotubes ($\sim 10 \mu\text{m}$) without amorphous carbon deposition. After growth, typically a few tubes have grown from each catalyst site and, since the catalyst particles are patterned in known locations, the location of the nanotubes on the substrate is also known.

Nanotube location and electrode fabrication

After the nanotube deposition/growth, the substrates are inspected by atomic force microscopy. All our devices have ‘customized electrodes’, i.e., we design electrodes individually for each nanotube device. While this requires a considerable amount of AFM time and design compared to, for example, depositing random grids of electrodes on the substrate, we find it very convenient in order to contact ‘nice looking’ individual nanotubes with a given diameter and length in between electrodes. We also typically choose straight segments of nanotubes (to prevent multiple quantum dot formation) located on ‘residue-free’ areas, to minimize switching behaviour. The AFM pictures determine the precise location

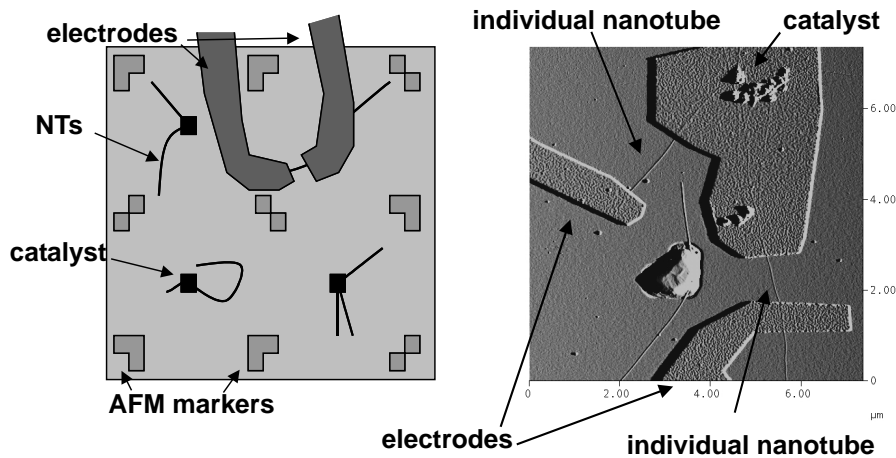


Figure 2.17: Fabrication process. Left: scheme of a substrate with the AFM markers, catalyst particles at predefined positions, grown nanotubes and designed electrodes. The separation between AFM markers is $6\mu\text{m}$. Right: Actual AFM picture of one of our devices.

of the nanotubes with respect to the predefined AFM markers. We import these pictures into a CAD program (Design CAD) and directly design the electrodes on top of the desired NTs. A subsequent e-beam lithography step is carried out to write the electrodes and evaporate the metal. The contact metal can be Cr/Au, Ti/Au, Pd, Ti/Al, etc... depending on the type of experiment. After lift-off, the sample is ready for optical inspection and room temperature characterization. In some cases we etch part of the SiO_2 in order to suspend the nanotubes. This is done by immersing the samples in buffered HF for $\sim 1 - 2$ min, transfer to water and followed by a gentle drying in hot IPA (to prevent the collapse of the nanotube due to surface tension effects).

Room temperature test and sample bonding

A typical sample substrate contains four cells, with about 4-8 devices per cell. If there are no problems with lift-off, the electrodes are placed on top of the NTs with nearly 100% yield. The devices are characterized electrically in a room temperature probe station, where the conductance is measured versus gate voltage to determine if the tubes are semiconducting or metallic and also how good is the contact to the nanotubes. After that, the chip is glued on a chip carrier and some selected devices are bonded. The sample is ready to be connected to the low temperature measurement setup.

References

- [1] Iijima, S. Helical Microtubules of Graphitic Carbon. *Nature* **354**, 56-58 (1991).
- [2] Iijima, S. & Ichihashi, T. Single-Shell Carbon Nanotubes of 1-Nm Diameter. *Nature* **363**, 603-605 (1993).
- [3] Bethune, D. S. *et al.* Cobalt-Catalyzed Growth of Carbon Nanotubes with Single-Atomic-Layerwalls. *Nature* **363**, 605-607 (1993).
- [4] Hamada, N., Sawada, S. & Oshiyama, A. New One-Dimensional Conductors - Graphitic Microtubules. *Phys. Rev. Lett.* **68**, 1579-1581 (1992).
- [5] Saito, R., Fujita, M., Dresselhaus, G. & Dresselhaus, M. S. Electronic-Structure of Chiral Graphene Tubules. *Appl. Phys. Lett.* **60**, 2204-2206 (1992).
- [6] Tans, S. J. *et al.* Individual single-wall nanotubes as quantum wires. *Nature* **386**, 474-477 (1997).
- [7] Bockrath, M. *et al.* Single-electron transport in ropes of carbon nanotubes. *Science* **275**, 1922-1925 (1997).
- [8] Thess, A. *et al.* Crystalline ropes of metallic carbon nanotubes. *Science* **273**, 483-487 (1996).
- [9] Wallace, P. R. The Band Theory of Graphite. *Phys. Rev.* **71**, 622-634 (1947).
- [10] Dresselhaus, M. S., Dresselhaus, G. & Eklund, P. C. *Science of Fullerenes and Carbon Nanotubes* (Academic Press, San Diego, 1996).
- [11] Minot, E. D. Tuning the band structure of carbon nanotubes. Ph.D. Thesis (2004).
- [12] White, C. T. & Mintmire, J. W. Density of states reflects diameter in nanotubes. *Nature* **394**, 29-30 (1998).
- [13] Dresselhaus, M. S., Dresselhaus, G. & Avouris, Ph. *Carbon Nanotubes: Synthesis, Structure, Properties, and Applications* (Springer, New York, 2001).
- [14] Lemay, S. G. *et al.* Two-dimensional imaging of electronic wavefunctions in carbon nanotubes. *Nature* **412**, 617-20 (2001).
- [15] Minot, E., Yaish, Y., Sazonova, V. & McEuen, P. L. Determination of electron orbital magnetic moments in carbon nanotubes. *Nature* **428**, 536-539 (2004).
- [16] U. C. Coskun *et al.*, *Science* **304**, 1132 (2004).

-
- [17] Kane, C. L. & Mele, E. J. Size, shape, and low energy electronic structure of carbon nanotubes. *Phys. Rev. Lett.* **78**, 1932-1935 (1997).
- [18] Ouyang, M., Huang, J. L., Cheung, C. L. & Lieber, C. M. Energy gaps in 'metallic' single-walled carbon nanotubes. *Science* **292**, 702-705 (2001).
- [19] Kwon, Y. K. & Tomanek, D. Electronic and structural properties of multiwall carbon nanotubes. *Phys. Rev. B* **58**, R16001-R16004 (1998).
- [20] Heyd, R., Charlier, A. & McRae, E. Uniaxial-stress effects on the electronic properties of carbon nanotubes. *Phys. Rev. B* **55**, 6820-6824 (1997).
- [21] Minot, E. D. *et al.* Tuning carbon nanotube band gaps with strain. *Phys. Rev. Lett.* **90**, 156401 (2003).
- [22] Yang, L. & Han, J. Electronic structure of deformed carbon nanotubes. *Phys. Rev. Lett.* **85**, 154-157 (2000).
- [23] Zhou, C. W., Kong, J. & Dai, H. J. Intrinsic electrical properties of individual single-walled carbon nanotubes with small band gaps. *Phys. Rev. Lett.* **84**, 5604-5607 (2000).
- [24] Kouwenhoven, L. P., Marcus, C. M., McEuen, P. L., Tarucha, S., Westervelt, R. M. & Wingreen, N.S. Electron transport in quantum dots, in *Mesoscopic Electron Transport*, edited by Sohn, L. L., Kouwenhoven, L. P. & Schön, G. (Kluwer, Series E **345**, 1997), p.105-214.
- [25] Javey, A., Guo, J., Wang, Q., Lundstrom, M. & Dai, H. Ballistic carbon nanotube field-effect transistors. *Nature* **424**, 654-7 (2003).
- [26] Mann, D., Javey, A., Kong, J., Wang, Q. & Dai, H. J. Ballistic transport in metallic nanotubes with reliable Pd ohmic contacts. *Nano Letters* **3**, 1541-1544 (2003).
- [27] Kim, W. *et al.* Electrical Contacts to Carbon Nanotubes Down to 1nm in Diameter. E-print available at <http://de.arxiv.org/abs/cond-mat/0505431>.
- [28] Oreg, Y., Byczuk, K. & Halperin, B.I. Spin configurations of a carbon nanotube in a nonuniform external potential. *Phys. Rev. Lett.* **85**, 365 (2000).
- [29] Ando, T & Nakanishi, T. Impurity scattering in carbon nanotubes - Absence of back scattering -. *J. Phys. Soc. Jpn.* **67**, 1704-1713 (1998).
- [30] McEuen, P. L., Bockrath, M., Cobden, D. H., Yoon, Y. & Louie, S. G. Disorder, pseudospins, and backscattering in carbon nanotubes. *Phys. Rev. Lett.* **83**, 5098-5101 (1999).

- [31] Averin, D. V. & Nazarov, Yu. V. in *Single Charge Tunneling - Coulomb Blockade Phenomena in Nanostructures*, edited by Grabert, H. & Devoret, M.H. (Plenum Press and NATO Scientific Affairs Division, New York, 1992), p. 217.
- [32] de Haas, W. J., de Boer, J. H. & van den Berg, G. J. *Physica* **1**, 1115 (1934).
- [33] Kondo, J. *Prog. Theor. Phys.* **32**, 37 (1964).
- [34] Kouwenhoven, L. P. & Glazman, L. I. *Physics World* **14**, 33 (2001).
- [35] Glazman, L. I. & Raikh, M. E. Resonant Kondo transparency of a barrier with quasilocal impurity states, *JETP Lett.* **47**, 452 (1988).
- [36] Ng, T. K. & Lee, P. A. On-site Coulomb repulsion and resonant tunneling, *Phys. Rev. Lett.* **61**, 1768 (1988).
- [37] Kawabata, A. *J. Phys. Soc. Jpn.* **60**, 3222 (1991).
- [38] van der Wiel, W. G. *et al.* *Science* **289**, 2105 (2000).

Chapter 3

Electron-hole symmetry in a semiconducting carbon nanotube quantum dot

P. Jarillo-Herrero, S. Sapmaz,
C. Dekker, L. P. Kouwenhoven, and H. S. J. van der Zant

Optical and electronic phenomena in solids arise from the behaviour of electrons and holes (unoccupied states in a filled electron sea). Electron-hole symmetry can often be invoked as a simplifying description, which states that electrons with energy above the Fermi sea behave the same as holes below the Fermi energy. In semiconductors, however, electron-hole symmetry is generally absent since the energy band structure of the conduction band differs from the valence band [1]. Here we report on measurements of the discrete, quantized-energy spectrum of electrons and holes in a semiconducting carbon nanotube [2]. Through a gate, an individual nanotube is filled controllably with a precise number of either electrons or holes, starting from one. The discrete excitation spectrum for a nanotube with N holes is strikingly similar to the corresponding spectrum for N electrons. This observation of near perfect electron-hole symmetry [3] demonstrates for the first time that a semiconducting nanotube can be free of charged impurities, even in the limit of few-electrons or holes. We furthermore find an anomalously small Zeeman spin splitting and an excitation spectrum indicating strong electron-electron interactions.

This chapter has been published in Nature **429**, 389 (2004).

3.1 Introduction

Carbon nanotubes can be metallic or semiconducting depending on their chirality. Electron transport through individual nanotubes has been studied for both classes [2]. Nanotubes of finite length have a discrete energy spectrum. Analogous to studies on semiconducting quantum dots, these discrete states can be filled with electrons, one by one, by means of a voltage applied to a nearby gate electrode [4]. Whereas metallic nanotubes have shown clean quantum dot (QD) behaviour [5, 6, 7], this has not been achieved in semiconducting single wall nanotubes (SWNTs). Theory indicates that semiconducting tubes are more susceptible to disorder than metallic ones [8, 9]. Disorder typically divides a semiconducting nanotube into multiple islands preventing the formation of a single, well-defined QD. Consequently, the electronic spectrum of semiconducting SWNTs has not been resolved before.

We report here on clean semiconducting tubes and focus on the regime of a few charge carriers (electrons or holes). We use high-purity carbon nanotubes (HiPco [10]), which are deposited with low density on a doped Si substrate (serving as a backgate) that has an insulating SiO₂ top layer [11, 12]. Individual nanotubes are electrically contacted with source and drain electrodes (50 nm Au on 5 nm Cr). We then suspend the nanotubes by etching away part of the SiO₂ surface [12]. We generally find that removing the nearby oxide reduces the amount of potential fluctuations (i.e. disorder) in the nanotubes, as deduced from transport characteristics.

3.2 A few electron-hole quantum dot

In this paper we focus on one particular semiconducting device that shows regular single QD behaviour for both few-hole and few-electron doping. The distance between the electrodes in this device is 270 nm (Fig. 3.1a). The dependence of the linear conductance on gate voltage shown in Fig. 3.1c is typical for semiconducting p and n-type behaviour [13, 14]. A low-temperature measurement around zero gate voltage (Fig. 3.1d) shows a large zero-current gap of about 300 meV in bias voltage, reflecting the semiconducting character of this nanotube. The zigzag pattern outside the semiconducting gap is due to Coulomb blockade [4]. These Coulomb blockade features are more evident in Fig. 3.1e, where a high-resolution measurement of the differential conductance shows the semiconducting gap with the first two adjacent Coulomb blockade diamonds.

The identification of the Coulomb diamonds for the first electron and first hole allows for an unambiguous determination of the particle number as we continue

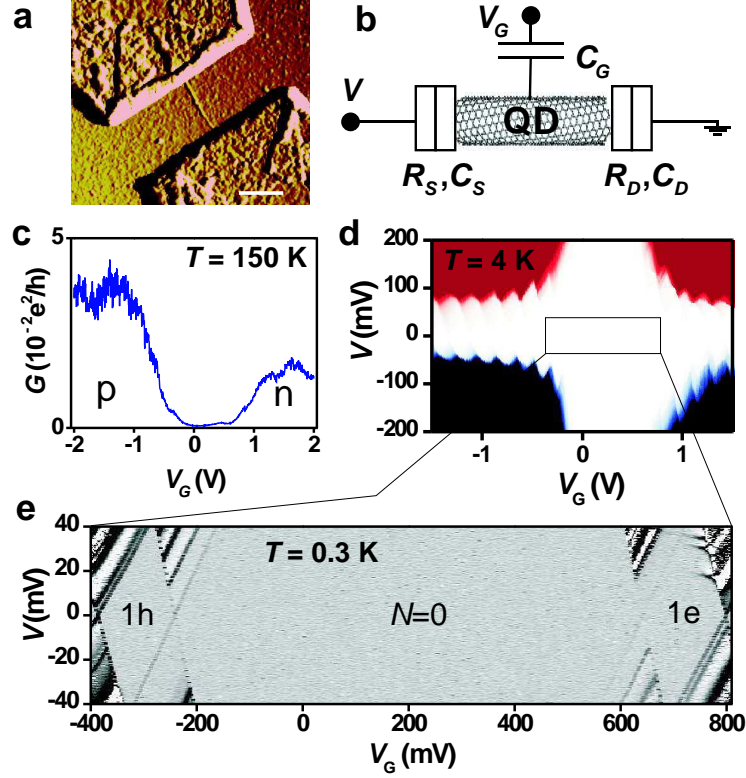


Figure 3.1: Sample and characterization. **a**, Atomic force microscope image of the device before suspension (scale bar, 200 nm). **b**, Device scheme: The nanotube QD is connected to source and drain electrodes via tunnel barriers characterized by resistances R_S , R_D and capacitances C_S , C_D . The backgate is represented by a capacitor C_G . The dc source-drain current, I , is recorded in the measurements as a function of source-drain voltage V and gate voltage V_G . Current-voltage ($I - V$) characteristics are numerically differentiated to obtain the differential conductance, dI/dV . **c**, Linear conductance, G , as a function of gate voltage, V_G , at a temperature, $T \sim 150$ K showing the p and n conducting regions separated by the semiconducting gap. **d**, Large-scale plot of the current (blue, negative; red, positive; white, zero) versus both V and V_G at $T = 4$ K. **e**, High-resolution measurement of the differential conductance as a function of V and V_G in the central region of **d** at 0.3 K. Between $V_G \sim -250$ and 650 mV, the nanotube QD is depleted entirely from mobile charge carriers. As V_G increases (decreases), one electron (hole) enters the dot as indicated in the right (left) Coulomb diamond.

to fill the QD by further changing the gate voltage. Figure 3.2a shows the filling of holes, one by one, up to 20 holes. The region for the first 2 holes is enlarged in Fig 3.2b. The regularity in the Coulomb diamonds indicates a nanotube that is free of disorder. A closer inspection shows that the size of the Coulomb diamonds varies periodically on a smooth background as the hole number increases

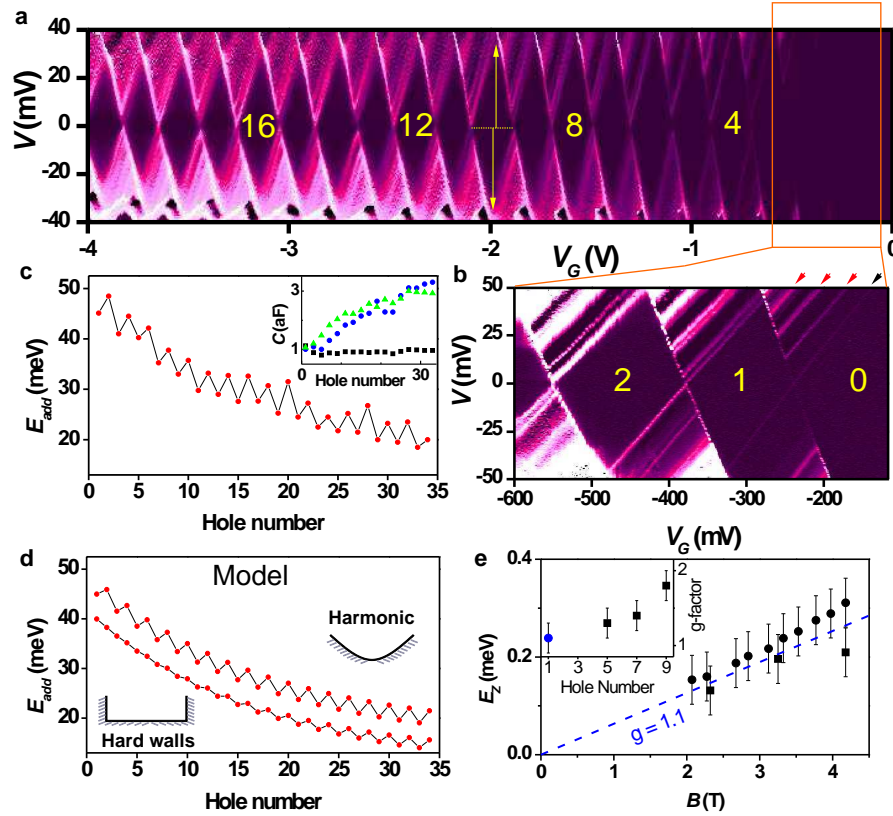


Figure 3.2: Few-hole semiconducting nanotube. **a**, Two-dimensional colour plot of dI/dV , vs. V and V_G at $T = 4$ K (black is zero, white is $3\mu\text{S}$). In the black diamond-shaped regions the number of holes, N , is fixed by Coulomb blockade. **b**, Zoom in taken at 0.3 K of the region with 0 , 1 , and 2 holes (white represents $dI/dV > 10$ nS). Lines outside the diamonds running parallel to the edges correspond to discrete energy excitations (the black (red) arrow points at the one electron ground (excited) states). **c**, Addition energy, E_{add} , vs. N . E_{add} is deduced from the diamond size for positive and negative V (i.e. half the sum of the yellow arrows in **a**). Inset, the capacitances C_S (green), C_D (blue) and C_G (black) vs. N . **d**, Calculation of the addition energy spectrum for a semiconducting nanotube (as an example we have taken a zig-zag $(35,0)$, with $E_{gap} \sim 259$ meV, $m_{eff} = 0.037m_e$ [3]) for a harmonic potential (top) and a hard-wall potential (bottom). The parameters for the harmonic potential are: $V(x = \pm 135$ nm) = $E_{gap}/2$ (see appendix). **e**, Zeeman splitting energy, E_Z , vs. magnetic field, B , for the one hole orbital states. The data result from two different types of measurements: (i) individual gate voltage traces at fixed bias (circles) and (ii) stability diagrams (squares, see also appendix). Inset: g -factor as a function of N . The point for $N = 1$ is the average of the data in Fig. 3.2e. The points for $N = 5, 7$ and 9 are obtained from co-tunneling (see appendix).

(Fig. 3.2c). The alternating, even-odd pattern in this addition energy, E_{add} , reflects the subsequent filling of discrete orbital states with two holes of opposite spin [4].

3.3 Electron-hole symmetry

We first focus on the additional discrete lines outside the Coulomb diamonds running parallel to its edges, as for instance indicated by arrows in Fig. 3.2b. Whereas the upper-left edge of the N -hole diamond reflects the ground state energy of the $(N+1)$ -hole, the extra lines located at higher voltages, V , represent the discrete excitation spectrum for $(N+1)$ -holes [4]. The spacing in V directly measures the energy separation between the excitations. Such discrete spectra were not obtained before for semiconducting nanotubes.

We now compare the excitation spectra for a particular hole (h) number with the same electron (e) number. The left and right columns in Fig. 3.3 show the spectra for, respectively, holes and electrons. The upper row compares the spectra for 1h and 1e. The yellow arrows in Fig. 3.3a point at the first 3 excited states for a single hole. (Note that only lines with positive slopes are observed because of asymmetric tunnel barriers [4].) Yellow arrows in Fig. 3.3b indicate the corresponding first 3 excitations for a single electron. (Figure 3.4 explains this correspondence.) Remarkably, we have simply mirror-imaged the arrows from the hole to the electron side without any adjustment of their spacing. We thus find that the 1h and 1e excitations occur at the same energy. Since one-particle systems are free from particle-particle interactions, this symmetry implies that the confinement potential for electrons is the same as for holes.

Electron-hole symmetry also survives interactions as demonstrated in the lower rows in Fig. 3.3. Again the arrows pointing at the hole excitations have simply been mirror-imaged to the electron side. Thus, we indeed find that the spectra for 2h and 2e and for 3h and 3e show virtually perfect electron-hole symmetry in the excitation spectra. From a closer look one can see that also the relative intensities of the excitation lines display electron-hole symmetry.

The quality of our data allows for a quantitative analysis. The addition energy is defined as the change in electrochemical potential when adding the $(N+1)$ charge to a QD containing already N charges. The constant-interaction (CI) model [4] gives $E_{add} = U + \Delta E$, where $U = e^2/C$ is the charging energy ($C = C_S + C_D + C_G$) and ΔE is the orbital energy difference between $N+1$ and N particles on the QD. In the case of a semiconductor QD the addition energy for adding the first electron to the conduction band equals $U + E_{gap}$. From the

observed gap size of 300 meV and $U \sim 50$ meV, we determine the semiconducting gap $E_{gap} \sim 250$ meV, which corresponds to a nanotube diameter of 2.7 nm [3]. AFM measurements, that usually underestimate the real height [15], indicate an apparent tube height of 1.70.5 nm.

Since two electrons with opposite spin can occupy a single orbital state, the CI model predicts an alternating value for E_{add} , where $E_{add} = U$ for $N = \text{odd}$, and $E_{add} = U + \Delta E$ for $N = \text{even}$. We indeed observe such an even-odd alternation in Fig. 3.2c with average $\Delta E \sim 4.3$ meV throughout the entire range of $N = 1$ to $N = 30$. Measurements of the Zeeman spin-splitting in a magnetic field (see appendix) confirm our assignment of even-odd particle number: Lines corresponding to ground states for odd N split (i.e. total spin =), whereas even- N lines do not split (i.e. total spin = 0). Figure 3.2e shows the value of the Zeeman energy for the one hole orbital states as a function of magnetic field. The data yield a reduced g -factor, $g \sim 1.1$, which is significantly lower than the value $g = 2$ reported on metallic nanotubes [5, 7]. (Some experiments on metallic nanotubes report deviations [16].) The reduction in g -factor disappears when adding holes. The inset shows that already for 9 holes the normal value is almost recovered. Lower g -factors are generally due to spin-orbit coupling, but this effect is small for carbon. It may hint at strong electron-electron interactions in the 1D-QD (see discussion below).

The addition energy spectrum indicates $\Delta E \sim 4.3$ meV for consecutive states as we fill the QD with holes. Previous spectra from metallic nanotubes have been analysed by considering a hard-wall potential in the nanotube, with an effective mass determined by the band structure. Our data show that this approach is not justified for semiconducting nanotubes. Lack of effective screening in 1D and the low number of mobile charges yield a gradual potential decay from the contacts [17]. We have computed the addition energy spectrum for a semiconducting nanotube whose gap is ~ 250 meV for two situations (Fig. 3.2d): hard-wall and harmonic potential of height $E_{gap}/2$ at the contacts [17]. For hard walls the level spacing increases slowly up to ~ 1.9 meV for $N = 34$. In the case of a harmonic potential, the level spacing is constant, as in the experiment, and equals 2.7 meV, in reasonable agreement with the experimental value ~ 4.3 meV (see also appendix).

On top of the predicted even-odd pattern, there is a monotonic decrease of the average charging energy with N , implying that the total capacitance is changing. We have performed a detailed analysis of the QD electrostatics following ref. [18]. The result is given in the inset to Fig. 3.2c. It shows that the change in C is mainly due to an increase in C_S and C_D . This increase can be assigned to a decrease of the tunnel barrier widths as $|V_G|$ increases, consistent with the simultaneous

increase of dI/dV in Fig. 3.2a,b. Indeed, dI/dV varies from $(5G\Omega)^{-1}$ in the first Coulomb peak to $(400k\Omega)^{-1}$ at large negative V_G .

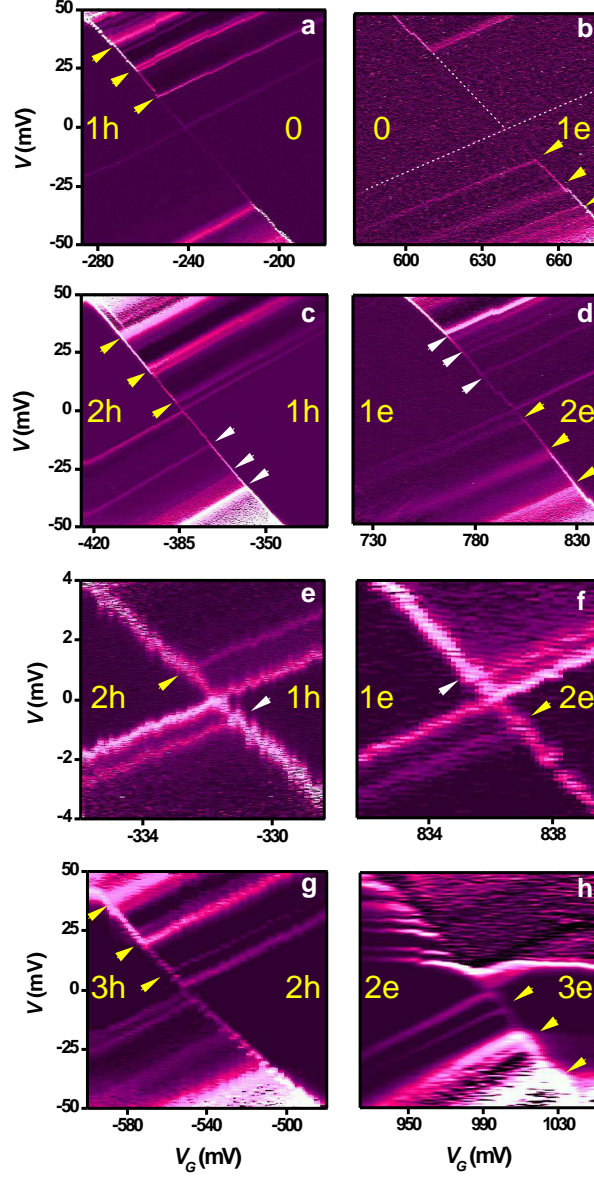


Figure 3.3: Excitation spectra for different electron and hole numbers demonstrating electron-hole symmetry. dI/dV is plotted versus (V, V_G) at $T = 0.3$ K. **a**, The transition from the 0 to 1h Coulomb diamonds. **b**, Corresponding transition from 0 to 1e. The white dotted lines in **b** are guides to the eye to indicate the diamond edge (not visible for this choice of contrast). **c** and **d**, same for 1-2h and 1-2e. **e** and **f**, Low-bias zoom in of the 1-2h and 1-2e crossings. **g** and **h**, Crossings corresponding to the 2-3h and 2-3e regions. (In **h**, the current switched between two stable positions for positive bias, with corresponding noise in dI/dV .)

The observation of electron-hole symmetry poses severe restrictions on the QD system: the effective masses for holes and electrons should be equal and the QD should be free of disorder. Scattering by negatively charged impurities, for example, is repulsive for electrons but attractive for holes, so it would break electron-hole symmetry. A symmetric band structure has been theoretically predicted for graphite materials and carbon nanotubes [3]. In contrast, the absence of scattering has come as a positive surprise.

Figure 3.4 clarifies the correspondence between the electron and hole excitation spectra. On the right side of Fig. 3.4b the situation for electrons is drawn (for $V_G > 0$) and on the left side for holes (for $V_G < 0$). The resulting excitations in transport characteristics as a function of V and V_G then lead to spectra as sketched in Fig. 3.4c and as measured in Fig. 3.3.

A detailed analysis of the excitation spectrum requires calculations that are beyond the scope of this paper. The constant-interaction model provides the parameter range for more exact models. The change in orbital energy when adding a charge is given by $\Delta E \sim 4.3$ meV, independent of N . ΔE is the scale for the energy difference between single-particle states. Excitations of a smaller energy scale have to be related to interactions. The likely interactions in semiconducting nanotubes are (1) Exchange interaction between spins (e.g. spin = 1 triplet states gain energy from the exchange interaction). Note that we observe an even-odd pattern, which seems to exclude ground states with spins $> 1/2$. Excited states, however, can have spins $> 1/2$. (2) Electron-phonon interactions. The vibrational modes in a suspended nanotube also have a discrete spectrum, which can show up in the excitation spectra [19]. Note that vibrational modes do not affect the addition energy spectrum of the ground states. (3) Electron-electron interactions. The value for the interaction strength parameter $U/\Delta E \sim 10$. Such a large $U/\Delta E$ ratio points to the presence of phenomena that are not captured by the CI model. Luttinger liquid models developed for finite length metallic nanotubes are not applicable to our few particle nanotubes. A more appropriate starting point are the exact calculations for 1D QDs. In the few particle regime the charge carriers tend to localize and maximize their separation, thereby forming a Wigner crystal [20]. In such a Wigner state, the spectrum consists both of high-energy single particle excitations and collective excitations at low energy [21], similar as in our experiment. Detailed calculations beyond the CI model and a comparison with the experimental results are necessary to establish the precise effect on transport from these interactions.

We thank R. E. Smalley and coworkers for providing the high-quality HiPco nanotubes, and S. De Franceschi, J. Kong, K. Williams, Y. Nazarov, H. Postma, S. Lemay and J. Fernandez-Rossier for discussions. We acknowledge the technical

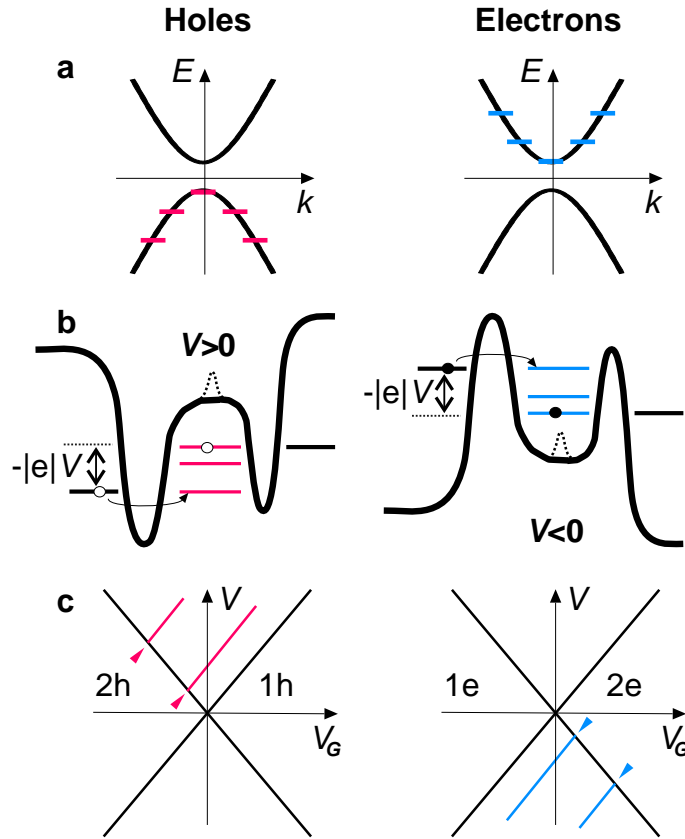


Figure 3.4: Electron-hole symmetry in semiconducting SWNTs. **a**, Band structure (energy E versus wave vector k) of a semiconducting nanotube illustrating symmetric valence and conduction bands. Due to quantum confinement, the carriers occupy a set of discrete energy states, shown on the left for hole doping and on the right for electron doping. **b**, Schematic energy diagrams showing transport of holes (left) and electrons (right) across a QD. The levels for the ground state and two excited states for $N = 2$ are drawn. The distance between equivalent levels on the right and left is the same due to equal effective electron and hole masses. The top hole level is accessed from the left for $V > 0$, whereas the top electron level aligns with the left lead Fermi energy for $V < 0$. The dotted line in the potentials shows the effect of a negatively charged scatterer, which breaks electron-hole symmetry. **c**, Excitation spectra resulting from the energy diagrams in **b**. New levels entering the bias window due to excited states lead to lines in the dI/dV plots that run parallel to the diamond edges. (Note that due to asymmetric barriers, only excitation lines with positive slope become visible.) These diagrams can be compared to the experiment in 3.3.

assistance of R. Schouten, B. van der Eenden and M. van Oossanen. Financial support is obtained from the Dutch organization for Fundamental Research on Matter (FOM), which is financially supported by the 'Nederlandse Organisatie

voor Wetenschappelijk Onderzoek' (NWO).

References

- [1] Ashcroft, N. W. & Mermin, N. D. Solid State Physics (Saunders College, Orlando, 1976).
- [2] Dekker, C. Carbon nanotubes as molecular quantum wires. *Phys. Today* **52**, 22-28 (1999).
- [3] Dresselhaus, M. S., Dresselhaus, G. & Eklund, P. C. Science of Fullerenes and Carbon Nanotubes (Academic Press, San Diego, 1996).
- [4] Kouwenhoven, L. P., Austing, D. G. & Tarucha, S. Few-electron quantum dots. *Rep. Prog. Phys.* **64**, 701-736 (2001).
- [5] Tans, S. J. *et al.* Individual single-wall nanotubes as quantum wires. *Nature* **386**, 474-477 (1997).
- [6] Bockrath, M. *et al.* Single-electron transport in ropes of carbon nanotubes. *Science* **275**, 1922-1925 (1997).
- [7] Cobden, D. H. & Nygård, J. Shell filling in closed single-wall carbon nanotube quantum dots. *Phys. Rev. Lett.* **89**, 046803-1-046803-4 (2002).
- [8] Ando, T & Nakanishi, T. Impurity scattering in carbon nanotubes - Absence of back scattering -. *J. Phys. Soc. Jpn.* **67**, 1704-1713 (1998).
- [9] McEuen, P. L., Bockrath, M., Cobden, D. H., Yoon, Y. & Louie, S. G. Disorder, pseudospins, and backscattering in carbon nanotubes. *Phys. Rev. Lett.* **83**, 5098-5101 (1999).
- [10] Bronikowski, M. J., Willis, P. A., Colbert, D. T., Smith, K. A. & Smalley, R. E. Gas-phase production of carbon single-walled nanotubes from carbon monoxide via the HiPco process: A parametric study. *J. Vacuum Sci. Technol. A* **19**, 1800-1805 (2001).
- [11] Fuhrer, M. S. *et al.* , Crossed nanotube junctions, *Science* **288**, 494-497 (2000).
- [12] Nygård, J. & Cobden, D. H. Quantum dots in suspended single-wall carbon nanotubes. *Appl. Phys. Lett.* **79**, 4216-4218 (2001).
- [13] Bachtold, A., Hadley, P., Nakanishi, T. & Dekker, C. Logic circuits with carbon nanotube transistors. *Science* **294**, 1317-1320 (2001)
- [14] Park, J. & McEuen, P. L. Formation of a p-type quantum dot at the end of an n-type carbon nanotube. *Appl. Phys. Lett.* **79**, 1363-1365 (2001).

- [15] Postma, H. W. C., Sellmeijer, A. & Dekker, C. Manipulation and imaging of individual single-wall carbon nanotubes with an atomic force microscope. *Adv. Mater.* **12**, 1299-1302 (2000).
- [16] Postma, H.W.C., Yao, Z., & Dekker, C. Electron addition and excitation spectra of individual single-wall carbon nanotubes. *J. Low Temp. Phys.* **118**, 495-507 (2000).
- [17] S. Heinze *et al.*, Carbon nanotubes as Schottky barrier transistors. *Phys. Rev. Lett.* **89**, 106801 (2002).
- [18] Grabert, H. & Devoret, M. H. *Single Charge Tunneling* (Plenum, New York, 1992).
- [19] Park, H. *et al.* Nano-mechanical oscillations in a single-C60 transistor. *Nature* **407**, 57-60 (2000).
- [20] Wigner, E. On the interaction of electrons in metals. *Phys. Rev.* **46**, 1002-1011 (1934).
- [21] Häusler, W. & Kramer, B. Interacting electrons in a one-dimensional quantum dot. *Phys. Rev. B* **47**, 16353-16357 (1993).
- [22] White, C. T. & Todorov, T. N. Carbon nanotubes as long ballistic conductors. *Nature* **393**, 240-242 (1998).
- [23] Kogan, A. *et al.* Measurements of Kondo and spin splitting in single-electron transistors. *Phys. Rev. Lett.* **93**, 166602 (2004).

3.4 Appendix

This appendix contains additional discussion and data, and was published as Supplementary Information to the main text in the corresponding publication (see Chapter title's page).

Model calculations

In the main text we show model calculations of the addition energy, E_{add} , for two types of electrostatic potential in the nanotube: hard-wall versus a parabolic potential (Fig. 3.2d). In both cases, we assume a zig-zag $(n, m) = (0, 35)$ nanotube (taken such that the theoretical band gap, $E_{gap} \sim 259$ meV, is close to the experimental value $E_{gap} \sim 250$ mV). From the band structure of this nanotube we obtain $m_{eff} \sim 0.037m_e$ (ref. [3] main text). The effective mass, m_{eff} , is an important parameter for the value of the level spacing. We note that

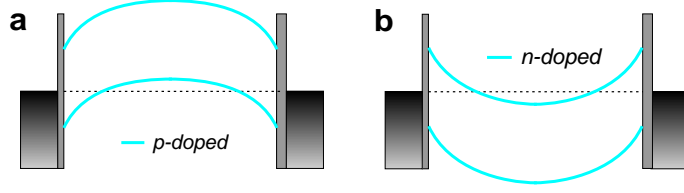


Figure 3.5: Band diagram scheme in the nanotube for negative, **a**, and positive, **b**, gate voltage.

m_{eff} is the same for a given semiconducting gap and approximately independent of chirality. In the case of a hard-wall potential, the level spacing is given by $\Delta E_n = E_n - E_{n-1} = \hbar^2 \pi^2 (2n - 1) / 2m_{eff} L^2$, where L is the length of the nanotube. This value of ΔE_n increases with n , which is not observed in the data. In contrast, for a harmonic potential, the level spacing is constant, and equal to $\hbar\omega_o$. We determine $\hbar\omega_o$ by requiring the potential height at the nanotube edges to be equal to half the band gap, $E_{gap}/2 = 1/2 m_{eff} \omega_o^2 (L/2)^2$. The important point is that the potential is gradually decaying into the nanotube (ref. [17] main text, see Fig. 3.5 for a scheme of the band diagram in the nanotube for both negative and positive gate voltages). We find that only experimentally determined parameters (E_{gap} and L) enter the model calculations. To simulate the monotonic decrease of the charging energy with N , we have fitted the odd values of the addition energy [$E_{add}(N_{odd}) = U$]. Then $E_{add}(N + 1) = U(N + 1) + \Delta E_n$, with $(N + 1) = \text{even}$. We note that we keep the harmonic potential constant as we fill the QD with holes. Screening will start to play a role as we add more and more charges to the nanotube and will gradually change the harmonic potential into a hard-wall potential. Moreover, in the calculations we have included spin degeneracy for each orbital state and an extra factor of 2 to account for the two 1D modes in the nanotube.

Scattering and disorder

Here we show additional data from another semiconducting device which shows regular quantum dot behaviour and where the discrete spectrum can be discerned. We discuss also the importance of disorder. The symmetry in the electron-hole excitation spectrum (Fig. 3.3) shows that there is absence of significant charged scatterers in the device as discussed in the main text. This is especially important since semiconducting nanotubes are much more sensitive to disorder than metallic ones. It should also be noted that the diameter of the nanotube described in the main text is rather large. It is known that large diameter nanotubes are less sensitive to disorder than small diameter ones [22]. For com-

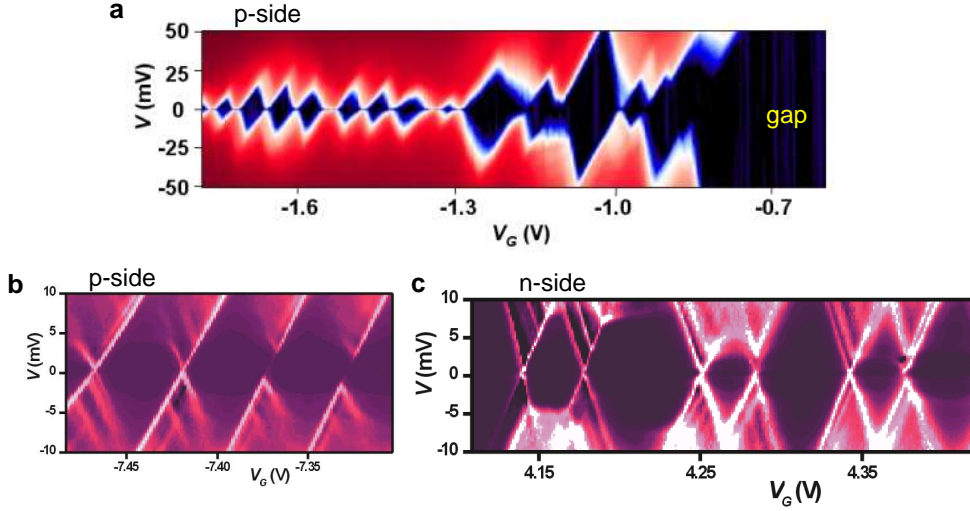


Figure 3.6: Differential conductance plot for a different semiconducting nanotube device. **a**, Few hole regime. **b**, Large hole number regime. **c** High electron number regime.

parison, we show additional data corresponding to a CVD-grown, non-suspended semiconducting nanotube. The estimated band gap is ~ 800 meV (corresponding to ~ 1 nm diameter). Fig. 3.6a shows the few-hole Coulomb diamonds (the current is plotted in log-color scale) in the p -doped region at $T = 4$ K, next to the semiconducting gap. The number of holes could not be exactly determined. For $N \geq 6 - 8$ the nanotube exhibits single quantum dot behaviour. However, the pattern becomes irregular as the quantum dot is near full depletion. This is a general feature of most of the studied semiconducting devices. We believe that as the QD is depleted, the holes or electrons tend to localize due to a lack of screening of the disorder potential, consequently forming multiple islands. Fig. 3.6, b and c, show Coulomb diamonds (differential conductance) deep in the p -side ($N_h \sim 100$) and in the n -side ($N_e \sim 40$) at $T = 300$ mK for the same device in a different cool down. The discrete spectrum is very clearly visible. We can conclude, then, that single QD behaviour can be observed in semiconducting nanotubes both in the few-charge carrier regime (main text) and in the regime with many particles (Fig. 3.6, b and c). In order to study clean nanotubes in the few charge-carriers regime, it may be important to select large diameter nanotubes. We have observed in other (metallic) samples that also suspending the nanotubes yields in general more stable devices. This seems to be an advantage also in the case of semiconducting nanotubes.

Zeeman splitting

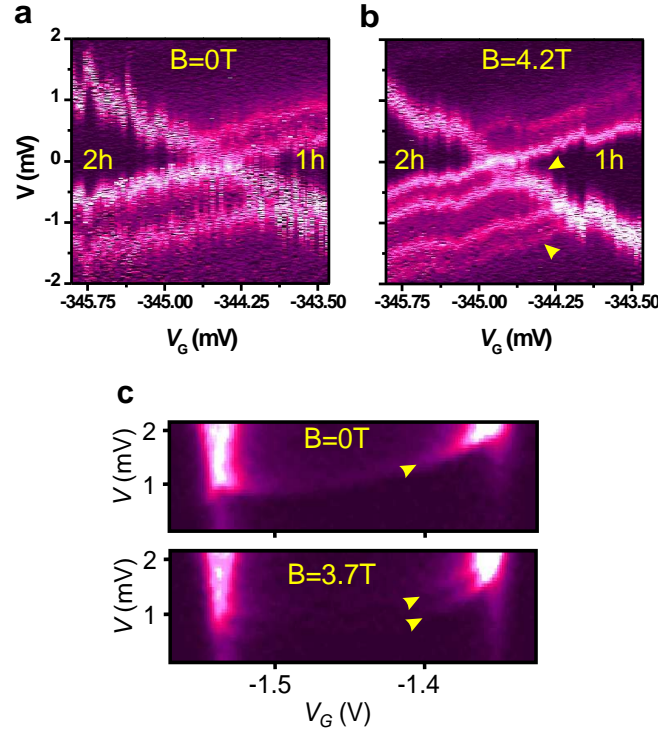


Figure 3.7: Zeeman splitting in a magnetic field B . **a**, Color-scale differential conductance plot in the 1-2 electron region at zero field. **b**, Same as **a**, but at $B = 4.2$ T. **c** Zeeman splitting in the inelastic cotunneling regime.

We show here dI/dV versus (V, V_G) at low energies in the 1-2 holes region at zero (Fig. 3.7a) and finite (Fig. 3.7b) magnetic field, showing the Zeeman splitting for $N = 1$ (indicated by the yellow arrows). For $N = 2$ no Zeeman splitting is observed, as expected. We have performed an analysis of the inelastic cotunneling data (raw data shown in Fig. 3.7c) in a magnetic field [23], from which we obtain the g -factor as we increase the number of holes. (Note that the Zeeman splitting can be observed only for $N_h = \text{odd}$.) We have data for $N = 5, 7$ and 9 , where the onset of inelastic-cotunneling is clearly observable. These are plotted in the inset to Fig. 3.2e.

Chapter 4

Electronic excitation spectrum of metallic carbon nanotubes

S. Sapmaz, P. Jarillo-Herrero, J. Kong,
C. Dekker, L. P. Kouwenhoven, and H. S. J. van der Zant

We have studied the discrete electronic spectrum of closed metallic nanotube quantum dots. At low temperatures, the stability diagrams show a very regular four-fold pattern that allows for the determination of the electron addition and excitation energies. The measured nanotube spectra are in excellent agreement with theoretical predictions based on the nanotube band structure. Our results permit the complete identification of the electron quantum states in nanotube quantum dots.

This chapter has been published in *Physical Review B* **71**, 153402 (2005).

4.1 Introduction

Since their discovery [1] carbon nanotubes (NTs) have emerged as prototypical one-dimensional conductors [2]. At low temperatures, NT devices form quantum dots (QDs) where single-electron charging and level quantization effects dominate [3, 4]. A continuous improvement in device fabrication and NT quality has enabled the recent observation of two-electron periodicity in 'closed' QDs [5] and four-electron periodicity in 'open' single- and multi-wall NT QDs [6, 7]. Theoretically, the low-energy spectrum of single wall nanotube (SWNT) QDs has been modeled by Oreg *et al.*, [8]. Experiments on open NT QDs are compatible with this model, but the presence of the Kondo effect and broadening of the energy levels prevents the observation of the full spectrum [9]. An analysis of the electronic excitations is therefore still lacking.

The two-fold degenerate, low-energy band structure of a metallic SWNT is schematically shown in Fig. 4.1a. Quantization along the nanotube axis leads to a set of single particle states that are equally spaced because of the linear dispersion relation [10]. The combination of the two bands and the spin yields a four-fold periodicity in the electron addition energy. The simplest model to describe QDs is the Constant Interaction (CI) model [11], which assumes that the charging energy is constant and independent of the occupied single particle states. To describe NT QDs the CI-model has been extended [8] to include five independent parameters: the charging energy E_C , the quantum energy level separation Δ , the subband mismatch δ (see Fig. 4.1a), the exchange energy J and the excess Coulomb energy dU . Fig. 4.1c illustrates the meaning of the last two parameters. An independent verification of the Oreg model [8] requires the observation of the ground state addition energies and of, at least, two excited states. Such a study has not been reported.

Here we investigate the excitation spectrum of closed SWNT QDs. Not only the ground but also the complete excited state spectrum of these QDs has been measured by transport-spectroscopy experiments, enabling us to determine all five parameters independently. With these, the remaining measured excitation energies are well predicted leading to a complete understanding of the spectrum, without adjustable parameters.

4.2 Four-fold shell filling

HiPco [12] and CVD [13] grown NTs were used for the fabrication of the devices. HiPco tubes were dispersed from a dichloroethane solution on an oxidized, *p*-doped Si substrate. The CVD nanotubes were grown from catalyst particles on

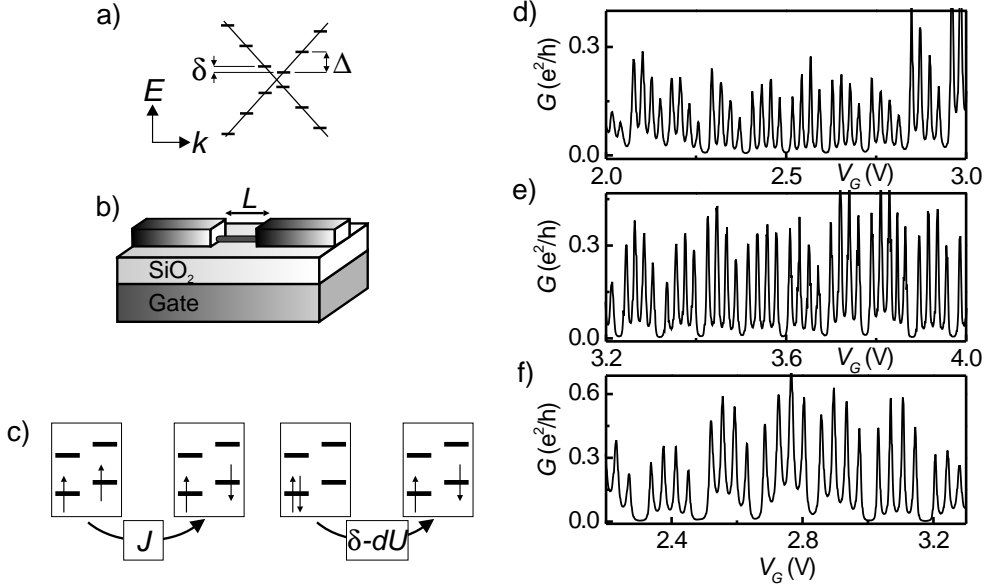


Figure 4.1: (a) Low-energy band structure of a metallic SWNT. In a finite length SWNT, the wave vector k is quantized along the tube axis which leads to a set of quantized energy levels separated by Δ in each band. δ is the mismatch between the two bands. (b) Schematic diagram of the device geometry. (c) Meaning of J (left) and dU (right). The exchange energy favors spin alignment and dU is the extra charging energy associated with placing two electrons in the same energy level. (d), (e), and (f) Conductance as a function of gate voltage in the linear response regime at 4 K for three different CVD grown samples. The NT lengths are 500, 680 and 760 nm, respectively.

predefined positions. Individual NTs were located by atomic force microscopy (AFM) with respect to predefined marker positions and electrodes were designed on top of straight segments of NTs. The highly doped silicon is used as a backgate to change the electrostatic potential of the NT QD (see Fig. 4.1b). We have fabricated NT devices with lengths in between contacts, L , varying from 100 nm to 1 μm .

Four-electron shell filling has been observed in over 15 samples. In some cases the four-fold pattern extended over more than 60 electrons added to the QD. Figs. 4.1d-f show representative examples of Coulomb Blockade (CB) oscillations [14] in the linear response regime. Clearly, the Coulomb peaks are grouped in sets of four reflecting the two-fold character of the NT bandstructure.

In the following, we focus on three different devices exhibiting similar four-fold periodicity in CB oscillations. These samples (A, B and C) had high enough contact resistances so that not only the electron ground states but also their excited states could be resolved. Together they provide enough information to

determine all the parameters in the model. We discuss the results of these three samples separately.

4.3 HiPCO nanotubes

Sample A- This device is made from a HiPco NT [12] with $L = 180$ nm and a diameter of 1.1 nm as determined by AFM. It is contacted by evaporating Cr/Au (5/75 nm) electrodes. Fig. 4.2a shows the current, I , as a function of source-drain bias voltage, V , and gate voltage, V_G . In the light-colored diamond-shaped regions, the current is blocked due to CB and the number of electrons is fixed. The clear four-fold periodicity makes it possible to assign the number of electrons in the last occupied shell. The sizes of the diamonds form an interesting pattern, namely a repetition of small/medium/small/big. This pattern is a consequence of the large subband mismatch compared to the exchange energy, as we show below.

The addition energy is defined as the change in electrochemical potential ($\Delta\mu_N$) when adding the $(N + 1)$ charge to a quantum dot already containing N charges [11]. The addition energy is obtained by multiplying the diamond width, ΔV_G , by a conversion factor, α (≈ 0.017), which relates the gate voltage scale to the electrochemical potential [14].

The Oreg-model yields the following equations for the addition energy of the N -th electron added [15]:

$$\Delta\mu_1 = \Delta\mu_3 = E_C + dU + J \quad (4.1)$$

$$\Delta\mu_2 = E_C + \delta - dU \quad (4.2)$$

$$\Delta\mu_4 = E_C + \Delta - \delta - dU. \quad (4.3)$$

To extract all five parameters, two more equations are needed. These are provided by the excitation spectrum. In Fig. 4.2c we show the numerical derivative of Fig. 4.2a (i.e., the differential conductance) for the first group of four. Excited states of the electrons are visible for all diamonds. The value of a particular excitation energy equals the bias voltage at the intersection between the excitation line and the Coulomb diamond edge (see Fig. 4.2c). The dotted (white) arrows in diamond one and two in Fig. 4.2c correspond to the first excitation for one and two electrons extra on the NT QD respectively. The theoretical values of these two energies are

$$\Delta\mu_1^{\text{ex}} = \delta, \Delta\mu_2^{\text{ex}} = \delta - J - dU. \quad (4.4)$$

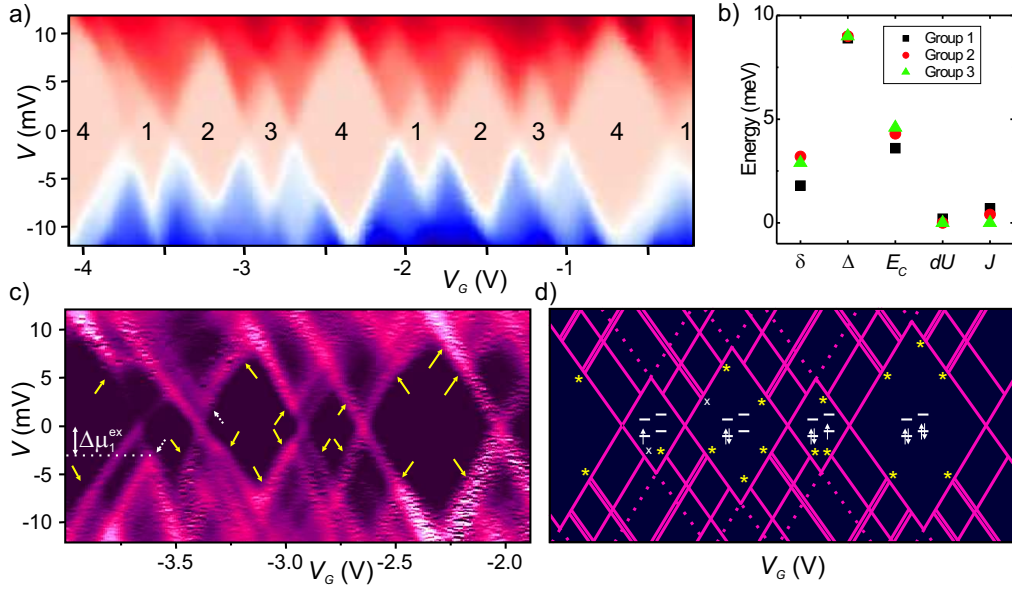


Figure 4.2: Sample A (a) Current as a function of V and V_G at $T = 300$ mK. Current goes from -40 nA to $+40$ nA. (b) Values of the parameters for three different groups of four (see text). (c) The differential conductance (dI/dV) for the first group from (a). Black is zero and bright is $>12 \mu\text{S}$. Lines running parallel to the diamond edges correspond to discrete energy excitations. The excitation energies corresponding to the dotted (white) arrows have been used to deduce the model parameters. The predicted excitations are indicated by (yellow) normal arrows. (d) Calculated spectrum for sample A. The stars correspond to the normal (yellow) arrows in (c) and x corresponds to the dotted (white) arrow. The white diagrams indicate the ground state spin filling.

Equations (4.1)-(4.4) allow us to uniquely determine the five unknown parameters from the experimental data alone. We find $E_C = 4.3$ meV, $\Delta = 9.0$ meV, $\delta = 3.2$ meV, $J = 0.4$ meV and $dU \approx 0$ meV. The values of the parameters do not vary significantly between the different groups, as shown in Fig. 4.2b. The theoretically expected value for the level spacing is $\Delta = \hbar v_F / 2L$ [3]. With $v_F = 8.1 \cdot 10^5$ m/s [16] and $L = 180$ nm, we find 9.3 meV in excellent agreement with the experimental value.

Figure 4.2d shows the calculated spectrum of the NT QD using the parameters deduced from the experiment. Some excitations are split by the exchange energy. The stars in the calculated spectrum correspond to the arrows in the experimental data. The excitations denoted with x were used for obtaining the parameters and correspond to the dotted (white) arrows in Fig. 4.2c. The calculated spectrum resembles the measured one strikingly well.

4.4 CVD nanotubes

Sample B- This sample is CVD grown [13] with a diameter of 1.3 nm and $L = 500$ nm defined by Cr/Au contacts (5/40 nm). After contacting, the entire NT segment in between electrodes is suspended by etching away part of the SiO_2 [17]. We have measured the differential conductance, dI/dV , as a function of V and V_G at 300 mK (Fig. 4.3a). Again regular four-fold patterns are visible in the Coulomb diamonds.

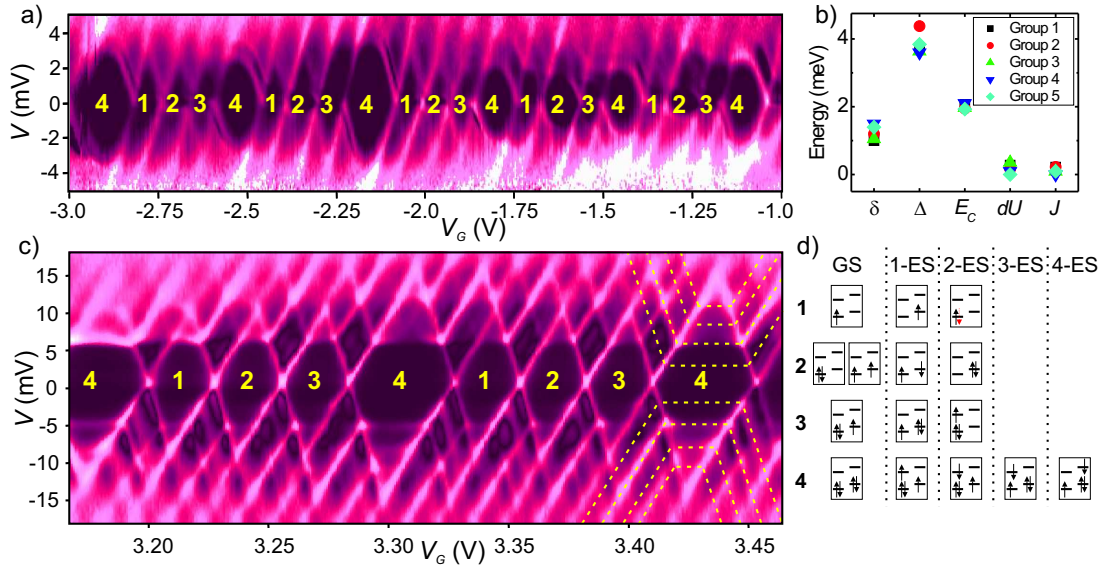


Figure 4.3: Differential Conductance of sample B (a) and C (c) as a function of V and V_G measured at 300 mK. Black represents $dI/dV \sim 0$, while lighter tones correspond to a higher conductance. Dashed lines in (c) indicate the excited states together with inelastic cotunneling. (b) Obtained parameters for sample B. (d) Electron quantum states of the NT QD. The numbers on the left denote the ground state (GS) number of electrons in the last occupied shell. The left column indicates the GS electron configuration (note that the two-electron GS is degenerate). Columns on the right denote the excited state (ES) configuration. Up to four ES are visible in the large Coulomb diamonds [22]. The dotted (red) arrow in the second ES for one electron corresponds to an electron excited from the lower shell.

The evolution of the Coulomb peaks as a function of the magnetic field (not shown here) gives information about the spin filling of the states [18]. We find that the filling is the same as sample A. Excited states of the QD are visible in all groups of four. The model parameters have been extracted using the same analysis as described above. The result is shown in Fig. 4.2b. The average values

are $E_C = 2.0$ meV, $\delta = 1.2$ meV, $J = 0.1$ meV, $dU = 0.2$ meV and $\Delta = 3.0$ meV. The value of Δ corresponds to a length of 440 nm [3], in good agreement with the NT length between contacts. Furthermore, in all groups of four at least one more excitation remains for a comparison between theory and experiment. In all cases we find good agreement [19].

Sample C- This NT is CVD grown [13] with a diameter of 2.7 nm and $L = 750$ nm. The contacts are made by evaporating Ti/Au (20/40 nm). Fig. 4.3c shows dI/dV as a function of V and V_G . A very regular pattern of Coulomb diamonds with four-fold periodicity is displayed together with the excited states. In addition, up to three inelastic co-tunneling lines [20] are visible (horizontal lines inside the Coulomb diamonds in Fig. 4.3c).

The observation of three equally sized small diamonds and the fact that the excitations have the same energy for all four charge states indicate that $\delta \approx J + 2dU$. We find $E_C = 6.6$ meV, $\Delta = 8.7$ meV, $\delta \approx J = 2.9$ meV, and $dU \approx 0$ meV. Theoretically a level separation of 8.7 meV indicates a NT QD length of ~ 200 nm, while the distance between contacts is 750 nm. This may suggest that sample C consists of a QD with NT leads connecting it to the contacts. This is consistent with the large value for E_C . Remarkably, all the predicted excitation lines are present in the spectrum [21]. Therefore all the electron states can be assigned (Fig. 4.3d).

In summary, we have presented a complete analysis of the electronic spectrum in closed NT QDs. Samples with different lengths, production process (CVD and HiPco) and contact material all exhibit four-fold periodicity in the electron addition energy. The very regular Coulomb traces and stability diagrams enable the determination of the ground and excited state electron energies. Knowing precisely the spectrum of nanotube quantum dots is of fundamental importance in experiments involving the application of high frequency radiation such as photon-assisted tunneling and coherent control of the electron quantum states.

We thank R. E. Smalley and coworkers for providing the high-quality HiPco nanotubes, and C. Meyer, W. Wetzels, M. Grifoni, R. Hanson, K.A. Williams, Yu. V. Nazarov and S. De Franceschi for discussions. Financial support is obtained from the Dutch organization for Fundamental Research on Matter (FOM).

References

- [1] S. Iijima, Nature (London) **354**, 56 (1991).
- [2] For reviews, see C. Dekker, Phys. Today **52**, No. 5, 22-28 (1999); P.L. McEuen, Phys. World, June, 31-36 (2000).

- [3] S.J. Tans *et al.*, Nature (London) **386**, 474 (1997).
- [4] M. Bockrath *et al.*, Science **275**, 1922 (1997).
- [5] D.H. Cobden and J. Nygård, Phys. Rev. Lett. **89**, 46803 (2002).
- [6] W. Liang, M. Bockrath, and H. Park, Phys. Rev. Lett. **88**, 126801 (2002).
- [7] M.R. Buitelaar *et al.*, Phys. Rev. Lett. **88**, 156801 (2002).
- [8] Y. Oreg, K. Byczuk, and B.I. Halperin, Phys. Rev. Lett. **85**, 365 (2000).
- [9] The Kondo effect shifts the position of the Coulomb peaks towards each other. The level broadening smears out the excitation spectrum.
- [10] M.S. Dresselhaus, G. Dresselhaus, P.C. Eklund, *Science of Fullerenes and Carbon Nanotubes* (Academic Press, San Diego, 1996).
- [11] L.P. Kouwenhoven, D.G. Austing and S. Tarucha, Rep. Prog. Phys. **64**, 701 (2001).
- [12] M.J. Bronikowski *et al.*, J. Vac. Sci. Technol. A **19**, 1800 (2001).
- [13] J. Kong, H.T. Soh, A.M. Cassell, C.F. Quate, H. Dai, Nature (London) **395**, 878 (1998).
- [14] H. Grabert and M.H. Devoret, *Single Charge Tunneling* (Plenum, New York, 1992).
- [15] This set of equations corresponds to singlet ground state for $N = 2$. The triplet case is incompatible with experimental data.
- [16] S.G. Lemay *et al.*, Nature (London) **412**, 617 (2001).
- [17] J. Nygård and D. H. Cobden, Appl. Phys. Lett. **79**, 4216 (2001).
- [18] R. M. Potok *et al.*, Phys. Rev. Lett. **91**, 16802 (2003).
- [19] The data show a very weak excitation around $200 \mu\text{eV}$. The origin of this excitation might be vibrational [H. Park *et al.*, Nature (London) **407**, 57 (2000)] corresponding to the first longitudinal mode in this suspended NT.
- [20] S. De Franceschi *et al.*, Phys. Rev. Lett. **86**, 878 (2001).
- [21] The experimental value of $\Delta\mu$ for the large Coulomb diamond is $\sim 15\%$ larger than deduced from the spectrum. The small Coulomb diamonds and the complete excitation spectrum is in perfect agreement with theory.
- [22] There is more than one degenerate configuration for some of the excited states. For simplicity we only show one of them.

Chapter 5

Electronic transport spectroscopy of carbon nanotubes in a magnetic field

P. Jarillo-Herrero, J. Kong, H. S. J. van der Zant,
C. Dekker, L. P. Kouwenhoven, and S. De Franceschi

We report magnetic field spectroscopy measurements in carbon nanotube quantum dots exhibiting four-fold shell structure in the energy level spectrum. The magnetic field induces a large splitting between the two orbital states of each shell, demonstrating their opposite magnetic moment and determining transitions in the spin and orbital configuration of the quantum dot ground state. We use inelastic cotunneling spectroscopy to accurately resolve the spin and orbital contributions to the magnetic moment. A small coupling is found between orbitals with opposite magnetic moment leading to anticrossing behavior at zero field.

This chapter has been published in *Physical Review Letters* **94**, 156802 (2005).

5.1 Introduction

The remarkable electronic behavior of carbon nanotubes (CNTs) originates from a particular combination of the symmetry properties of the graphene band structure and the quantization of momentum imposed by periodic boundary conditions along the nanotube circumference [1]. This symmetry results in a four-fold degenerate shell structure in the energy spectrum of CNT quantum dots (QDs). In early experiments on CNT QDs [3, 4], however, this symmetry was not observed, presumably due to the presence of defects. Improvements in the quality of CNTs and advances in nanofabrication techniques have enabled the recent observation of four-fold degeneracy in the spectrum of CNT QDs [5, 6]. An interesting effect related to the symmetry of the graphene band structure is the modulation of the energy gap in CNTs when placed in a parallel magnetic field, B . This effect, predicted early on [7], has only been recently observed in CNT QDs [8, 9]. These studies, however, did not show evidence of four-fold symmetry and the link between the energy spectrum and the B -evolution of the QD states was not established.

Here we report B -dependent electronic transport spectroscopy measurements on CNT QDs exhibiting four-fold shell structure. We show that: (i) each shell consists of two orbitals with opposite magnetic moment; (ii) the splitting of the orbital states with B accounts for all the observed transitions in the spin and orbital configuration of the CNT QD; (iii) a weak coupling exists between orbitals with opposite magnetic moment resulting in level repulsion at $B=0$; (iv) Zeeman and orbital contributions to the electron magnetic moment can be distinguished by inelastic-cotunneling spectroscopy.

5.2 Semiconductor carbon nanotube quantum dots

The electronic structure of CNTs can be derived from the two-dimensional band structure of graphene. The continuity of the electron wave function around the CNT circumference imposes the quantization of the wave-vector component perpendicular to the CNT axis, k_{\perp} . This leads to a set of one-dimensional subbands in the longitudinal direction. Due to symmetry, for a given subband at $k_{\perp}=-k_o$ there is a second degenerate subband at $k_{\perp}=k_o$. Figure 5.1a shows in black solid lines the schematic 1D band structure of a gapped CNT near the energy band gap. Both valence and conduction bands have two degenerate subbands, labelled as “+” and “-”. Ajiki and Ando [7] predicted that the orbital degeneracy should

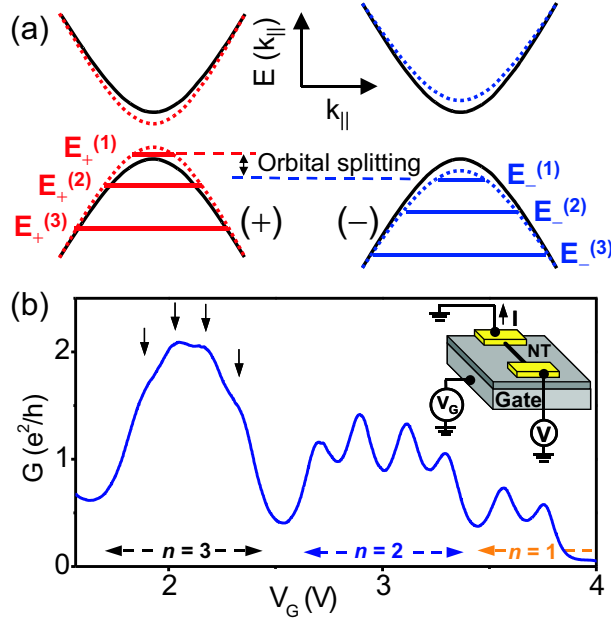


Figure 5.1: (a) Schematic band structure of a CNT near its energy gap. Black lines represent the one-dimensional energy dispersion relation, $E(k_{\parallel})$, at $B=0$ (k_{\parallel} is the wave vector along the CNT axis). The valence (conduction) band has two degenerate maxima (minima). Size quantization in a finite-length CNT results in a set of discrete levels with both spin and orbital degeneracy. The degeneracy is lifted by a magnetic field parallel to the CNT. The 1D subbands (and the corresponding levels) at finite B are represented by red and blue dotted (solid) lines. Only the orbital splitting of the energy levels is shown in this figure. (b) Linear conductance, G , vs gate voltage, V_G taken at $T=8\text{K}$. Inset: Device scheme.

be lifted by a magnetic field parallel to the CNT axis (Fig.1a). This effect can be understood by noting that, due to clockwise and anti-clockwise motion around the tube, electrons in degenerate “+” and “-” subbands should have opposite orbital magnetic moments, μ_{orb} . In the case of finite-length CNTs, a discrete energy spectrum is expected from size quantization. The level spectrum of a CNT QD can then be described as two sets of spin-degenerate levels, $E_+^{(n)}$ and $E_-^{(n)}$, where $n=1,2,3\dots$ is the quantum number in the longitudinal direction (see Fig. 5.1a). In the absence of inter-subband mixing, $E_+^{(n)} = E_-^{(n)}$ at $B=0$, and a four-fold degenerate shell structure is expected for every n . Below we show that a finite coupling can exist, resulting in a small orbital splitting even at $B=0$.

The four-fold shell filling emerges in a measurement of the linear conductance, G , versus gate voltage, V_G . This is shown in Fig. 5.1b for a QD device fabricated from a metallic nanotube with a small band gap [8, 10, 11]. G exhibits Coulomb

blockade oscillations [2] corresponding to the filling of the “valence” band of the CNT. From left to right, electrons are consecutively added to the last three electronic shells, $n=3, 2$ and 1 , respectively. The shell structure is apparent from the V_G -spacing between the Coulomb oscillations. The addition of an electron to a higher shell requires an extra energy cost corresponding to the energy spacing between shells. This translates into a larger width of the Coulomb valley associated with a full shell [12]. The first group of four Coulomb peaks on the left-hand side of Fig. 5.1b ($n=3$) are strongly overlapped due to a large tunnel coupling to the leads and Kondo effect [13]. The coupling decreases with V_G , becoming very small near the band gap, which lies just beyond the right-hand side of the V_G -range shown [14]. Due to this small coupling, the Coulomb peaks associated with the last two electrons in $n=1$ are not visible (see Fig. 5.2b).

5.3 Evolution of the ground state of the quantum dot with magnetic field

The shell structure breaks up at finite B (Fig. 5.2a). In each group of four Coulomb peaks, the first (last) two peaks shift towards lower (higher) V_G . This behavior demonstrates the strong B -dependence of the orbital levels described in Fig. 5.1a. The magnetic field shifts the “ $-$ ” orbital levels down in energy, while the “ $+$ ” orbitals are shifted up due to their opposite μ_{orb} . Consequently, the addition of the first (last) two electrons to a shell results in a pair of Coulomb peaks shifting toward lower (higher) V_G . For each shell, μ_{orb} can be extracted from the shift, $\Delta V_G(n)$, in the position of the corresponding Coulomb peaks. Neglecting the Zeeman splitting, we use the relation $e\alpha\Delta V_G(n) = |\mu_{orb}(n)\cos\varphi\Delta B|$, where ΔB is the change in B , φ is the angle between the nanotube and B , and α is a capacitance ratio extracted from non-linear measurements. The values obtained (0.90, 0.80 and 0.88 meV/T, for $n=1, 2$ and 3 , respectively) are an order of magnitude larger than the electron spin magnetic moment ($1/2g\mu_B=0.058$ meV/T for $g=2$), and in good agreement with an estimate of μ_{orb} based on the nanotube diameter [15].

The strong B -dependence of the orbital states induces changes in the orbital and spin configuration of the QD similar to previous findings in semiconducting QDs [16]. These are reflected as kinks in the evolution of the Coulomb peaks with B (Fig. 5.2b). Remarkably, a fully consistent description of the B -dependent energy spectrum and the ground state spin/orbital configuration can be obtained through a careful analysis of all the kinks in Fig. 5.2b, as illustrated by the diagrams in Fig. 5.3. As an example, we examine the non-trivial evolution of

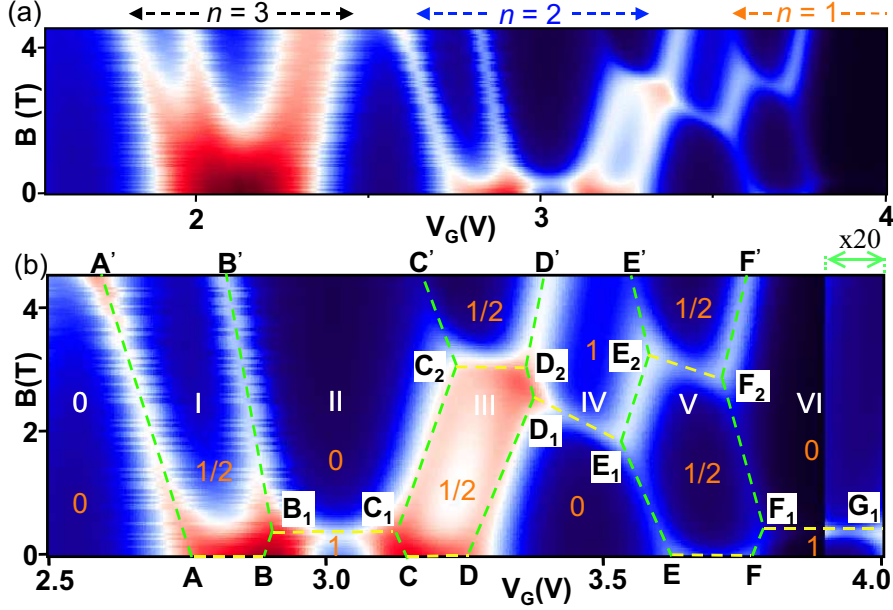


Figure 5.2: (a) G vs B on a color scale at $T=0.34\text{K}$ for the V_G range shown in Fig. 5.1b. Red, white and blue indicate high, intermediate and low G , respectively. The conductance range is 0 (dark blue) to $3e^2/h$ (dark red). (b) Zoom-in of (a) Here G ranges from 0 (dark blue) to $2e^2/h$ (dark red). The green dashed lines highlight the evolution of the Coulomb peaks with B . They are labelled as AA', BB'... and FF'. These divide the plot in different Coulomb blockade regions indicated by the number of electrons in the last two shells (white numbers 0 to VI). The high- G regions (indicated by yellow dashed lines) in between Coulomb peaks are due to Kondo effect. Orange numbers indicate the spin in each region. On the right side, the G is multiplied by 20, so that the triplet-singlet transition is clearly seen along F_1G_1 .

Coulomb peak CC' (notation defined in Fig. 5.3 caption). Segment CC_1 separates the triplet state in region II from the spin 1/2 state in region III. The incoming electron tunnels into the $E_-^{(2)}$ orbital, with spin down, so the slope of the CC_1 segment is “ $-\mu_{orb}^{(2)} + 1/2g\mu_B$ ”, as noted underneath the corresponding arrow. At B_1C_1 , a triplet-singlet transition occurs. Therefore C_1C_2 separates the singlet state in region II from the spin 1/2 state in region III. Now the incoming electron tunnels into the $E_+^{(2)}$ orbital state with spin up, so the slope of C_1C_2 is “ $\mu_{orb}^{(2)} - 1/2g\mu_B$ ”. Interestingly, at C_2 a kink related to an inter-shell orbital crossing occurs. C_2C' also separates the singlet state in region II from the spin 1/2 state in region III (as C_1C_2), but the incoming electron tunnels into the $E_-^{(1)}$ state and with spin up, so the slope changes direction and has a value “ $-\mu_{orb}^{(1)} - 1/2g\mu_B$ ”. The rest of the diagrams can be followed in a similar manner [17].

Note that kinks in Fig. 5.2b are connected by conductance ridges crossing the

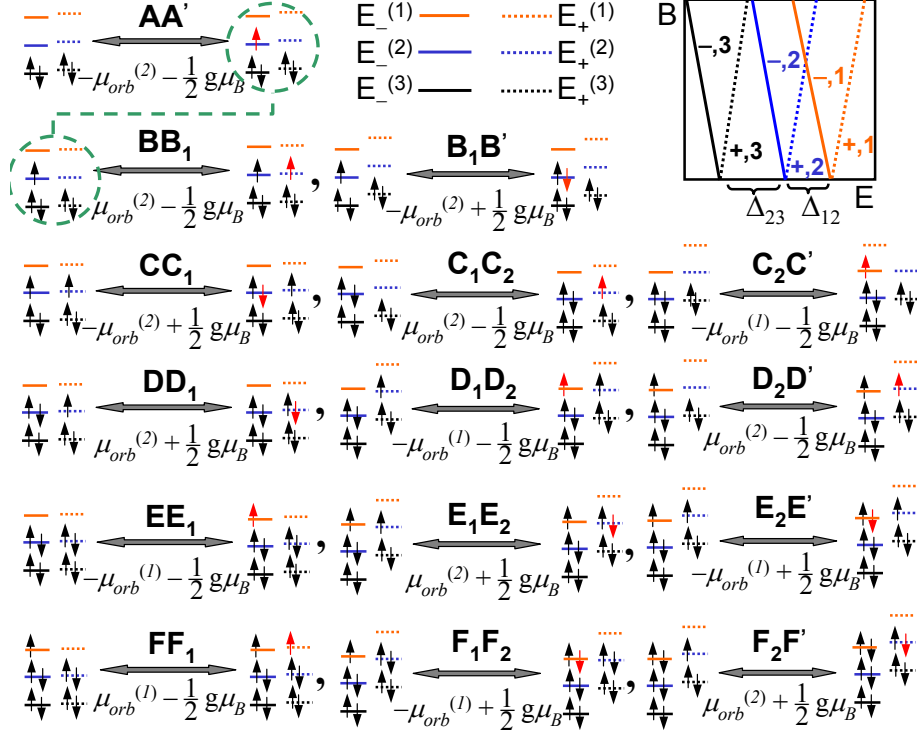


Figure 5.3: Diagrams representing the orbital and spin configuration in the different regions of Fig. 5.2b. Each row follows the B -evolution of a given Coulomb peak. Each section in a given row shows two diagrams (separated by a double arrow). These represent the ground state configuration in the two regions separated by the corresponding segment of the Coulomb peak evolution with B . In the diagrams, different colors refer to different shells: orange, blue and black for $n=1, 2$ and 3 , respectively (in our discussion here $n=3$ is always filled). The last added electron is displayed in red, all the others in black. Note that, for each diagram, the final state is the same as the initial state for the diagram immediately below (as indicated by the connected green dashed circles). We use solid (dotted) lines to represent levels with positive (negative) μ_{orb} , shifting down (up) with B (Zeeman splitting is neglected because it is an order of magnitude smaller than the orbital splitting). The slope corresponding to the B -evolution of the Coulomb peaks is also indicated under the double arrow. Top-right inset: qualitative energy spectrum of the CNT QD as a function of B (Zeeman splitting neglected). Since $\Delta_{1,2} \neq \Delta_{2,3}$, the energy spectrum is not periodic and the $G(B, V_G)$ pattern in Fig. 5.2 exhibits four-fold symmetry only for $B < 2T$.

Coulomb valleys. The enhancement of G at these ridges is due to Kondo effects of different origins. At B_1C_1 , D_1E_1 , and F_1G_1 the Kondo effect arises from singlet-triplet degeneracy [18]. At AB , CD , and EF an enhanced Kondo effect is observed in relation to orbital degeneracy [13]. The Kondo ridges at C_2D_2 and E_2F_2 are

due to the recovery of orbital degeneracy between $E_-^{(2)}$ and $E_+^{(1)}$ [13]. Note that, as a result of electron-hole symmetry, region III (three electrons in shell $n=2$) and region V (one electron in shell $n=1$) have a certain degree of mirror symmetry, both in terms of the slope of the Coulomb peaks' evolution with B and the Kondo ridges.

5.4 Inelastic cotunneling spectroscopy

The data shown so far have been explained in terms of a B -induced splitting of orbital degeneracy, as if the two orbital states of every shell were indeed degenerate at $B=0$. A small zero-field orbital splitting may in fact exist and be masked by the Kondo effect at AB, CD, and EF. In order to investigate this possibility, we considered a different device, which happened to have a much smaller coupling to the leads and hence much weaker Kondo effect. This device also exhibits four-fold periodicity in the Coulomb peaks' pattern. Fig 4c shows a Coulomb diamond corresponding to one electron in a shell at $B=80\text{mT}$ [19]. Inside the diamond, single electron tunneling is suppressed and transport occurs via higher order cotunneling processes. A sharp increase in the differential conductance, dI/dV , is observed at a bias $|V| = V_{in} \sim 190\mu\text{V}$, denoting the onset of inelastic cotunneling (IC) [20, 21, 22]. The IC transition takes place between the two spin-degenerate orbital levels of the same shell thereby indicating the existence of a finite splitting at $B=0$. Before discussing the B -dependence of the IC edges we note that a weak Kondo peak is also present at $V=0$ (top inset in Fig. 4a). This Kondo effect arises from the single-electron occupancy of the spin degenerate orbital ground state.

At finite B , both the Kondo peak and the IC edges split due to Zeeman spin splitting. This is shown in Fig. 5.4a, where dI/dV is plotted vs (V,B) for V_G at the center of the Coulomb diamond [19]. In order to identify the dI/dV steps more clearly, Fig. 5.4b shows the numerical derivative of the dI/dV plot in Fig. 5.4a (i.e. d^2I/dV^2 vs V and B). IC steps in Fig. 5.4a turn into peaks ($V>0$) or dips ($V<0$) in Fig. 5.4b. The zero-bias Kondo peak evolves into two dI/dV steps at $V = g\mu_B B/e$ ($g = 2$). These correspond to IC processes in which the spin state of the QD is flipped, i.e. from $|-, \uparrow\rangle$ (ground state) to $|-, \downarrow\rangle$ (excited state). Each of the two dI/dV steps associated with inter-orbital IC splits by $g\mu_B B/e$ and they move further apart due the increasing orbital splitting, $2\mu_{orb}B\cos\varphi$ ($\varphi = 33^\circ$). We estimate $2\mu_{orb} \sim 350\mu\text{eV/T}$ i.e. ~ 3 times the Zeeman splitting [23]. The inner inter-orbital steps correspond to IC from $|-, \uparrow\rangle$ to $|+, \uparrow\rangle$, and evolve with a slope $\pm 2\mu_{orb}/e$. The outer inter-

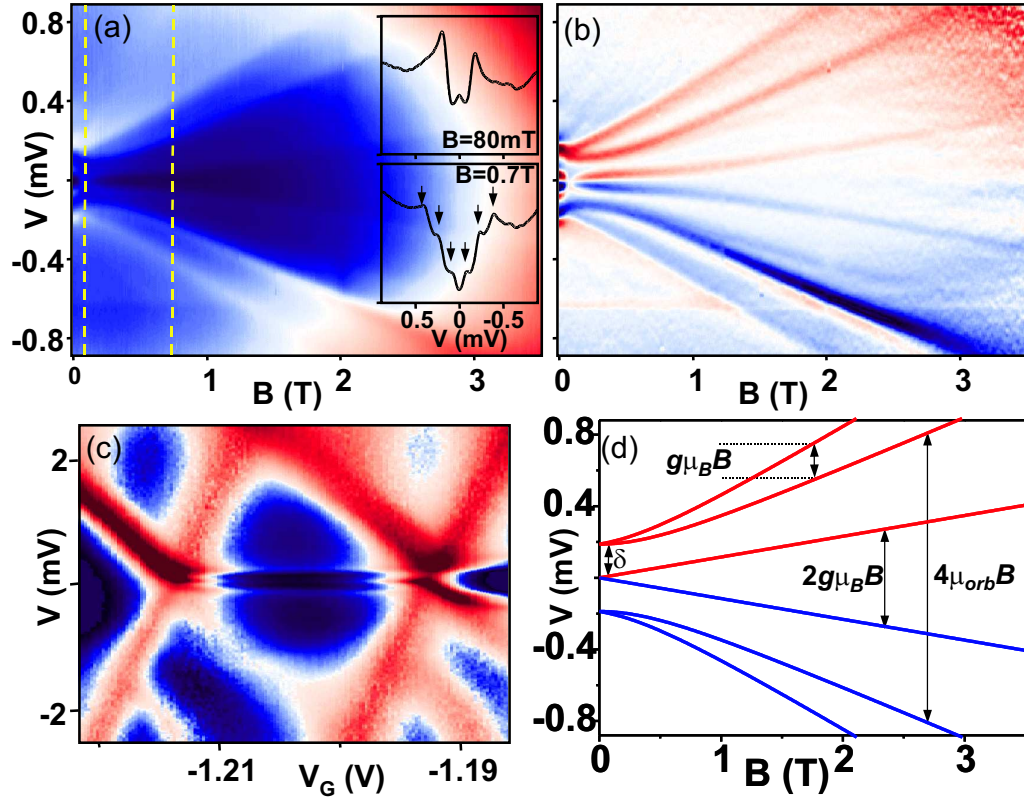


Figure 5.4: (a) Color-plot of the differential conductance, dI/dV , vs bias, V , and B , measured in the center of the Coulomb diamond (see (c)) at $T=30$ mK. The yellow dashed lines indicate the traces shown in the top and bottom insets. Insets: (top) dI/dV trace taken at $B=80$ mT, showing the onset of inter-orbital IC and a small zero bias peak due to ordinary spin 1/2 Kondo effect. The vertical axis scale spans from 0.02 to $0.08 e^2/h$. (bottom) Same as top inset, but at $B=0.7$ T, showing the six IC steps. (b) Numerical derivative of the dI/dV plot in (a). The two inner lines result from Zeeman splitting of the Kondo peak at $B=0$. The outer lines represent the B -evolution of the spin-split orbital levels. (c) dI/dV vs V and V_G , for a single electron in a shell at $B=80$ mT. (d) Calculated B -dependence of the IC spectrum for a single electron in a spin degenerate level for two coupled orbitals. Red (blue) lines indicate upwards (downwards) steps in dI/dV with increasing V .

orbital steps correspond to IC from $|-, \uparrow\rangle$ to $|+, \downarrow\rangle$, and evolve with a slope $\pm(2\mu_{orb} + g\mu_B B)/e$. The six steps (“Zeeman”, “orbital” and “orbital+Zeeman”) can be seen in the bottom inset to Fig. 5.4a. Such separation between the orbital and Zeeman contributions to the magnetic moment of electrons in CNTs has not been shown before. An important consequence of the angular dependence of the orbital splitting is that researchers have now two “semi-independent” knobs to control the energy spectrum of CNT QDs (B controls the Zeeman splitting and

the angle nanotube- B controls the orbital splitting).

The evolution of the outer IC peaks is non-linear at low B , indicating an anti-crossing between the “+” and “-” orbital levels. Such IC spectrum can be readily modelled using a Hamiltonian that includes an inter-orbital coupling besides orbital and Zeeman terms. The corresponding energy eigenstates are: $E = \pm\sqrt{(\delta/2)^2 + (\mu_{orb}B\cos\varphi)^2} \pm 1/2g\mu_B B$ (the 4 possible sign combinations). The IC spectrum calculated with this simple model (Fig. 5.4d) clearly accounts for the experimental data. The non-linear evolution of the orbital splitting with B constitutes direct evidence that the so-called “subband level mismatch”, usually denoted by δ [5], is due to a small, but finite, quantum mechanical coupling between the two orbital subbands in carbon nanotubes.

We finally comment on the reproducibility of the results shown. $G(B, V_G)$ patterns with a strong orbital contribution to the magnetic moment of electrons (similar to that in Fig. 5.2b) have been measured in all devices (five from three different fabrication runs) where four-fold shell filling was observed [24]. Our study demonstrates that the spin and orbital configuration of CNT QDs can be understood and controlled by means of a magnetic field. This will prove very useful in a variety of experiments with CNT QDs, such as the study of the Kondo effect in degenerate systems or the interaction between orbital states at high B .

Financial support is obtained from the Dutch organization for Fundamental Research on Matter (FOM).

References

- [1] N. Hamada, S.I. Sawada and A. Oshiyama, Phys. Rev. Lett. **68**, 1579 (1992).
- [2] For reviews, see C. Dekker, Phys. Today **52**, No. 5, 22-28 (1999); P.L. McEuen, Phys. World, June, 31-36 (2000); C. Schönenberger and L. Forro, *ibid.*, 37-41 (2000).
- [3] S.J. Tans *et al.*, Nature (London) **386**, 474 (1997).
- [4] M. Bockrath *et al.*, Science **275**, 1922 (1997).
- [5] W. Liang, M. Bockrath, and H. Park, Phys. Rev. Lett. **88**, 126801 (2002).
- [6] M.R. Buitelaar, A. Bachtold, T. Nussbaumer, M. Iqbal, C. Schönenberger, Phys. Rev. Lett. **88**, 156801 (2002).
- [7] H. Ajiki and T. Ando, J. Phys. Soc. Jpn **62**, 1255 (1993).
- [8] E. Minot *et al.*, Nature (London) **428**, 536 (2004).
- [9] U. C. Coskun *et al.*, Science **304**, 1132 (2004).

-
- [10] This band gap can be due to different perturbations, such as curvature or strain. The measured value of the band gap is $\sim 30\text{meV}$.
 - [11] The fabrication is similar to that reported in P. Jarillo-Herrero *et al.*, Nature (London) **429**, 389 (2004).
 - [12] From measurements in the non-linear regime (not shown), we estimate $\Delta_{1,2} \sim 3\text{meV}$, and $\Delta_{2,3} \sim 5\text{meV}$, where $\Delta_{n,n+1} \equiv E_+^{(n)} - E_+^{(n+1)} = E_-^{(n)} - E_-^{(n+1)}$. The Coulomb charging energy is $U \sim 5\text{meV}$.
 - [13] P. Jarillo-Herrero *et al.* Nature **434**, 484 (2005).
 - [14] Ti/Au electrodes typically lead to p-doped nanotubes at $V_G = 0$ (see H.T. Soh *et al.*, App. Phys. Lett. **75**, 627 (1999)), whose onset of conductance depends on the specific device considered.
 - [15] From the value for $n = 1$, we extract a nanotube diameter $D = 4\mu_{orb}/ev_F = 4.5\text{nm}$, in agreement with the measured diameter of $4.0 \pm 0.5\text{nm}$ as determined by atomic force microscopy. For this device $\varphi = 37^\circ$.
 - [16] S. Tarucha, D.G. Austing, T. Honda, R.J. van der Hage and L.P. Kouwenhoven, Phys. Rev. Lett. **77**, 3613 (1996).
 - [17] The presence of Kondo effect causes appreciable shifts in the position of the Coulomb peaks. This accounts for the quantitative discrepancies between the slopes in Fig. 2b and those quoted in Fig. 3. To estimate μ_{orb} , we take the average slope between the two Coulomb peaks that correspond to the addition of the electrons to the same orbital state (e.g. AA' and B₁B').
 - [18] S. Sasaki *et al.*, Nature (London) **405**, 764 (2000).
 - [19] At $B < 80\text{mT}$, the Ti/Au electrodes become superconducting. The features related to the superconductivity in the contacts (see Figs. 4a,b) will be reported elsewhere.
 - [20] H. Grabert and M.H. Devoret, Single Charge Tunneling (Plenum, New York, 1992).
 - [21] S. De Franceschi *et al.*, Phys. Rev. Lett. **86**, 878 (2001).
 - [22] A. Kogan *et al.*, Phys. Rev. Lett. **93**, 166602 (2004).
 - [23] For this device, the measurements are not taken next to the small-band gap, and this is possibly the reason why the value of μ_{orb} is smaller than expected from the nanotube diameter (2.7nm) [8] (see also [24]).
 - [24] Still, in some V_G ranges, the patterns exhibit large variations in μ_{orb} , even for consecutive shells. This might be due to defects, which could distort the band structure enough to render the simple picture in Fig. 1a invalid.

Chapter 6

Orbital Kondo effect in carbon nanotubes

P. Jarillo-Herrero, J. Kong, H. S. J. van der Zant,
C. Dekker, L. P. Kouwenhoven, and S. De Franceschi

Progress in the fabrication of nanometer-scale electronic devices is opening new opportunities to uncover the deepest aspects of the Kondo effect [1], one of the paradigmatic phenomena in the physics of strongly correlated electrons. Artificial single-impurity Kondo systems have been realized in various nanostructures, including semiconductor quantum dots [2, 3, 4], carbon nanotubes [5, 6] and individual molecules [7, 8]. The Kondo effect is usually regarded as a spin-related phenomenon, namely the coherent exchange of the spin between a localized state and a Fermi sea of electrons. In principle, however, the role of the spin could be replaced by other degrees of freedom, such as an orbital quantum number [9, 10]. Here we demonstrate that the unique electronic structure of carbon nanotubes enables the observation of a purely orbital Kondo effect. We use a magnetic field to tune spin-polarized states into orbital degeneracy and conclude that the orbital quantum number is conserved during tunneling. When orbital and spin degeneracies are simultaneously present, we observe a strongly enhanced Kondo effect, with a multiple splitting of the Kondo resonance at finite field and predicted to obey a so-called $SU(4)$ symmetry.

This chapter has been published in Nature **434**, 484 (2005).

6.1 Introduction

The simplest Kondo system consists of a localized, spin-1/2 electron coupled to a Fermi sea via a Heisenberg-like exchange interaction [1]. This simple system can be realised with a quantum dot (QD) device [2, 3, 4], which is a small electronic island connected to metallic leads via two tunnel barriers (see Fig. 6.1a). Below a characteristic temperature T_K , the so-called Kondo temperature, a many-body singlet state is formed between the QD spin and the surrounding conduction electrons (Fig. 6.1a). This state adds a resonant level at the Fermi energy of the electrodes enabling the tunneling of electrons across the QD. Such a Kondo

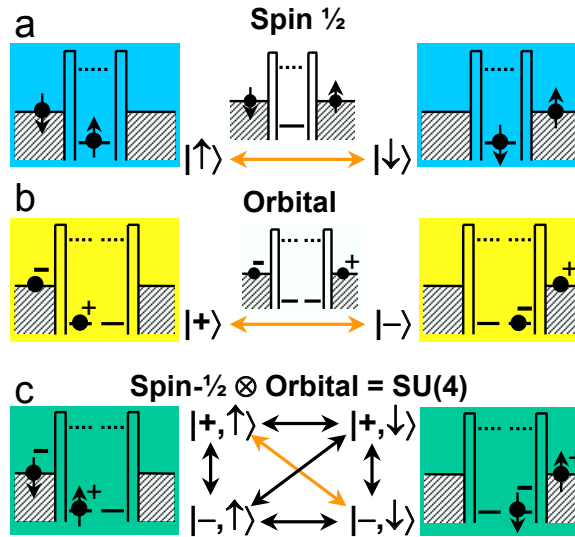


Figure 6.1: Spin, orbital and SU(4) Kondo effect in a quantum dot (QD) with an odd number of electrons. The left (right) panels in **a-c** represent initial (final) ground states. **a**, Schematic illustration of a spin-flip cotunneling process connecting the two states, $|\uparrow\rangle$ and $|\downarrow\rangle$, from a single orbital state. The intermediate virtual state is shown in the central diagram. This cotunneling event is one of many higher-order processes that add up coherently resulting in the screening of the local spin. **b**, Cotunneling process for spinless electrons for two degenerate orbital states, labelled $|+\rangle$ and $|-\rangle$. The depicted process flips the orbital quantum number from $|+\rangle$ to $|-\rangle$ and vice versa. The coherent superposition of orbital-flip processes leads to the screening of the local orbital quantum number. **c**, QD with two spin-degenerate orbitals leading to an overall four-fold degeneracy. Spin and/or orbital states can flip by one-step cotunneling processes, indicated by black arrows in the central diagram; the orange arrow refers to the cotunneling event connecting the two states depicted in the green diagrams. These processes lead to the entanglement of spin and orbital states resulting in an enhanced SU(4) Kondo effect.

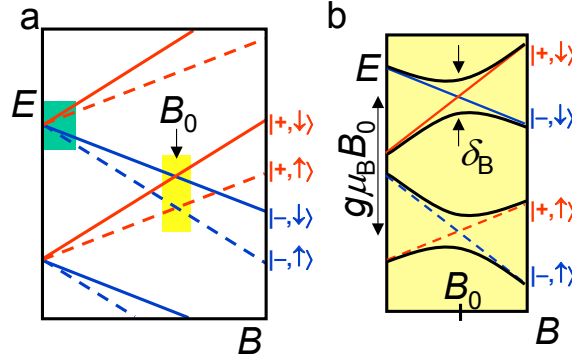


Figure 6.2: **a**, Qualitative single-particle energy spectrum of a CNT QD in a magnetic field. Red (blue) lines represent orbital states shifting up, $|+\rangle$, (down, $|-\rangle$) in energy. Dashed (solid) lines represent spin up (down) states. The yellow rectangle highlights the region where a purely orbital Kondo effect can occur due to a level-crossing (at $B = B_0$) between spin-polarized states. The green rectangle highlights the SU(4) Kondo region. **b**, Zoom in on the yellow rectangle in **a**. A finite coupling, δ_B , between $|+\rangle$ and $|-\rangle$ states causes an anticrossing (black lines). At high B , δ_B is smaller than the Zeeman splitting, $g\mu_B B$.

resonance can lead to a strong enhancement of the conductance overcoming the Coulomb blockade effect [2, 3, 4]. In principle, a Kondo effect may also occur in the absence of spin if another quantum number, e.g. an orbital degree of freedom, gives rise to a degeneracy (Fig. 6.1b). In this case, Kondo correlations lead to the screening of the local orbital “polarization”, and an orbital singlet is formed through a combination of orbital states. In the presence of both spin and orbital degeneracy, quantum fluctuations lead to a strong mixing of these two degrees of freedom (Fig. 6.1c). This increased degeneracy yields an enhancement of T_K [11]. In the low-temperature limit, this system is described by a Hamiltonian obeying SU(4)-symmetry, that is, the spin and charge degrees of freedom are fully entangled and the state of the electron is represented by a 4-component “hyperspin” [12, 13, 14, 15].

An orbital degeneracy is naturally expected in the electronic structure of carbon nanotubes [16] (CNTs). This degeneracy can intuitively be viewed to originate from the two equivalent ways electrons can circle around the graphene cylinder, that is, clockwise and anti-clockwise [17]. The rotational motion confers an orbital magnetic moment to the electrons. Consequently, the orbital degeneracy can be split by a magnetic field, B , parallel to the nanotube axis. (Experimental evidence for this effect, originally predicted by Ajiki and Ando [18], has been recently reported [17, 19, 20, 21].) We label the orbital states of a CNT QD as $|+\rangle$ or $|-\rangle$ according to the sign of the energy shift they experience under an applied

B . Size quantization due to the finite CNT length results in two sets of orbital levels, $E_+^{(n)}$ and $E_-^{(n)}$ where $n = 1, 2, 3$ is the quantization number. $E_+^{(n)} = E_-^{(n)}$ at $B = 0$ (assuming no orbital mixing), resulting in a four-fold degeneracy when including spin. The orbital and spin degeneracies are simultaneously lifted by a parallel B (Fig. 6.2d). The use of B allows tuning new degeneracies in connection with the crossing between levels from different shells. Here we are particularly interested in the crossing between states with the same spin polarisation, of the type indicated by the yellow rectangle in Fig. 6.2d. We show below that the two-fold orbital degeneracy originating from such a crossing gives rise to a purely orbital Kondo effect. We then consider the case of concomitant spin and orbital degeneracy at $B = 0$ (green rectangle in Fig. 6.2d) and present evidence for an $SU(4)$ Kondo effect.

6.2 Orbital Kondo effect

In a measurement of the linear conductance, G , as a function of gate voltage, V_G , the four-fold shell structure leads to consecutive groups of four closely-spaced Coulomb blockade oscillations [6, 22]. The B -evolution of such oscillations is shown in Fig. 6.3a for a CNT QD device (described in the inset and corresponding caption) in a V_G -region encompassing two adjacent shells. Coulomb peaks (highlighted by green lines) appear as lines running from bottom to top and denote the sequential addition of electrons to the QD; the electron number increasing from left to right. The observed pattern is explained in detail on the basis of the single-particle spectrum in Fig. 6.2d, and taking into account the Coulomb interaction between electrons (see appendix).

The Coulomb peaks move to the left or right when increasing B , corresponding to adding the last electron to a $|-\rangle$ or $|+\rangle$ orbital, respectively. When the ground state configuration of the QD changes, kinks appear in the B -evolution of the Coulomb peaks. The two enhanced-conductance ridges at $B = B_0 \sim 6$ T, bounded by two such kinks and highlighted by dotted yellow lines, are due to the crossing between $|-\rangle$ and $|+\rangle$ states as described in Fig. 6.2d. A detailed analysis (see appendix) indicates that along these ridges the QD ground state is doubly degenerate, with the last added electron occupying the level crossing between $|+, \uparrow\rangle$ and $|-, \uparrow\rangle$ (left ridge) or between $|+, \downarrow\rangle$ and $|-, \downarrow\rangle$ (right ridge).

In the region near the degeneracy point, we are able to measure a small coupling between orbital states [21], resulting in level repulsion at $B = B_0$. The energy splitting is directly observed in the spectroscopy data of Fig. 6.3b where the differential conductance, dI/dV , is shown versus B and bias voltage, V .

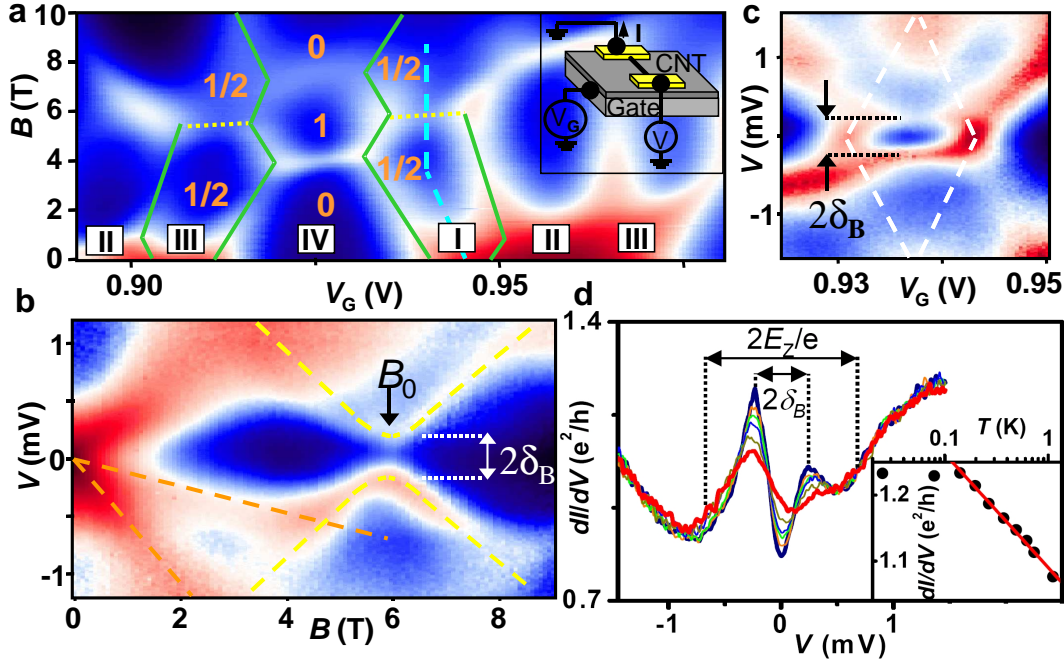


Figure 6.3: Orbital Kondo effect. **a**, Color-scale representation of the linear conductance, G , versus B and V_G at $T \sim 30$ mK (G increases from dark blue to dark red). The green lines highlight the B -evolution of the Coulomb peaks. The dotted yellow lines highlight regions of enhanced conductance due to Kondo effect. Roman labels indicate the number of electrons on the last occupied shell near $B = 0$. Orange numbers indicate the spin of the ground state. Inset: device scheme. Carbon nanotubes were grown by chemical vapour deposition on p -type Si substrates with a 250nm-thick surface oxide. Individual nanotubes were located by atomic force microscopy and contacted with Ti/Au electrodes (typical separation 100-800 nm) defined by e-beam lithography. The highly-doped Si substrate was used as a back-gate. **b**, Color-scale plot of the differential conductance, dI/dV , versus V and B along the dashed blue line in **a**. The field splits the Kondo resonance into multiple peaks. The two orange lines highlight the evolution of the peaks associated with the spin and orbital splitting, respectively. The spectroscopy features are more pronounced for $V < 0$, most likely due to asymmetric tunnel barriers [30]. The yellow lines highlight the orbital anticrossing at $B = B_0 = 5.9$ T. **c**, Coulomb diamond for 1 electron on the last occupied shell at $B = 5.9$ T. **d**, dI/dV vs V at different T , from 25 mK (thick blue trace) to 1.1 K (thick red trace), at the anticrossing point ($B = 5.9$ T, $V_G = 937$ mV). Orbital splitting, δ_B , and Zeeman splitting, E_Z , are visually compared. The split Kondo peaks decrease with increasing T . Inset: peak height vs T evaluated for the left peak.

In this measurement V_G and B are simultaneously varied in order to follow the middle of the Coulomb valley (dashed blue line in Fig. 6.3a). Here, single-electron tunneling is suppressed and the spectroscopy is based on higher-order cotunneling

processes, which lead to an enhancement of dI/dV every time V equals an internal excitation energy [23]. We focus on the high- B region of Fig. 6.3b. As B is swept across B_0 , the anti-crossing between $|+, \downarrow\rangle$ and $|-, \downarrow\rangle$ (depicted in Fig. 6.2b) shows up in the two dI/dV ridges highlighted by dashed yellow lines. The level spacing, corresponding to half the distance between these lines, reaches a minimum value $\delta_B = 225$ mV at $B = B_0 = 5.9$ T. In a measurement of dI/dV versus (V, V_G) at 5.9 T, shown in Fig. 6.3c, the higher-order peaks appear as horizontal ridges inside the Coulomb diamond. Their spacing, $2\delta_B$, is independent of V_G while their height increases towards the edges of the diamond.

An individual dI/dV versus V trace taken in the middle of the diamond is shown in Fig. 6.3d, together with traces measured at higher temperature, T . The strong overshoot of the dI/dV peaks and their $\log-T$ dependence (inset) indicate an important contribution from Kondo correlations. The observed behaviour is characteristic of a split Kondo resonance, i.e. a Kondo resonance associated with two quasi-degenerate states, in line with recent theoretical predictions [24] and experiments [25]. It is important to note that the Zeeman spin splitting, $E_Z = g\mu_B B_0$, is three times larger than δ_B , indicating that the Kondo effect originates entirely from orbital correlations occurring at the crossing between two spin polarized states, $|+, \downarrow\rangle$ and $|-, \downarrow\rangle$. This conclusion is in agreement with the zero-field data that we show below. The large Zeeman splitting ensures also that the observed orbital Kondo resonance provides a conducting channel only for $|\downarrow\rangle$ electrons, thereby acting as a high-transmission spin filter [12, 13, 14]. On the other hand, the conductance enhancement that occurs for three-electron shell filling originates from $|+, \uparrow\rangle$ and $|-, \uparrow\rangle$ states and hence it allows only tunnelling of $|\uparrow\rangle$ electrons. Switching from one degeneracy to the other is controlled by simply switching the gate voltage, which then causes the CNT QD to operate as a bipolar spin filter.

6.3 SU(4) Kondo effect

We now centre our attention on the zero-field regime, where both orbital and spin degeneracies are expected (green rectangle in Fig. 6.2d). The Coulomb oscillations corresponding to the filling of a single shell are shown in Fig. 6.4a for a different CNT QD device. The four oscillations are clearly visible at 8 K (red trace). At lower T , the conductance exhibits a pronounced enhancement in regions I and III, i.e., for 1 and 3 electrons on the shell, and the corresponding Coulomb blockade valleys completely disappear at 0.3 K (black trace). This conductance enhancement is a hallmark of Kondo correlations. From the T -dependence (fully

shown in the appendix) we estimate $T_K = 7.7$ K, an unusually high value that can be ascribed to the enhanced degeneracy [11]. The important contribution of the orbital degree of freedom becomes apparent from the B -dependence of G (Fig. 6.4e). If this Kondo effect was determined by spin only (this could be the case if one of the orbitals was coupled weakly to the leads), G should decrease on a field scale $B \sim k_B T_K / g \mu_B \sim 6$ T due to Zeeman splitting [26]. In contrast, G decays on a much smaller scale, $B \sim k_B T_K / 2 \mu_{orb} \sim 0.5$ T, which is determined by the orbital splitting (an estimate of the orbital magnetic moment, μ_{orb} , is given below).

In the non-linear regime, a single zero-bias Kondo resonance appears in regions I and III (Fig. 6.4b). Contrary to the result in Fig. 6.3c, no orbital splitting is observed due to the much larger T_K ($k_B T_K > \delta$ [12, 13, 21]). In region II, we observe two peaks at finite bias, reflecting the already known splitting of a singlet-triplet Kondo resonance [27]. To show that the Kondo resonance in I and III arises from simultaneous orbital and spin Kondo correlations we investigate the effect of lifting spin and orbital degeneracies at finite B . As opposed to an ordinary spin-1/2 Kondo system (where the Kondo resonance splits in two peaks, separated by twice the Zeeman energy [3, 4, 5, 6, 7, 8]) we find a fundamentally different splitting. At $B = 1.5$ T (Fig. 6.4c), multiple split peaks appear in regions I and III as enhanced- dI/dV ridges parallel to the V_G -axis. In region I, the large zero-bias resonance opens up in four peaks that move linearly with B and become progressively smaller (Fig. 6.4d). The two inner peaks are due to Zeeman splitting, i.e. to higher-order cotunneling from $|-, \uparrow\rangle$ to $|-, \downarrow\rangle$ ($|-\rangle$ is the lower-energy orbital). The two outer peaks arise from cotunneling from orbital $|-\rangle$ to orbital $|+\rangle$. In the latter case, inter-orbital cotunneling processes can occur either with or without spin flip. (The corresponding substructure [21], however, is not resolved due to the broadening of the outer peaks.) Similar multiple splittings of the Kondo resonance have been observed also in several other samples. According to recent calculations [28], the observed multiple splitting of the Kondo resonance constitutes direct evidence of $SU(4)$ symmetry, which implies the concomitant presence of spin as well as orbital Kondo correlations, confirming our previous finding.

The slope $|dV/dB|$ of a conductance peak (Fig. 6.4d) directly yields the value of the magnetic moment associated with the splitting. We obtain a spin magnetic moment $\mu_{spin} = |dV/dB|_{spin} = 0.06$ meV/T $\sim \mu_B$ from the inner peaks, and an orbital magnetic moment $\mu_{orb} = |dV/dB|_{orb} / \cos \varphi = 0.8$ meV/T $\sim 13 \mu_B$ from the outer peaks (φ is the angle between the nanotube and B) [17]. The same value of μ_{orb} follows from the splitting of the Kondo resonance in region III (Fig. 6.4c). In this case, however, no Zeeman splitting is observed. Here, the magnetic field

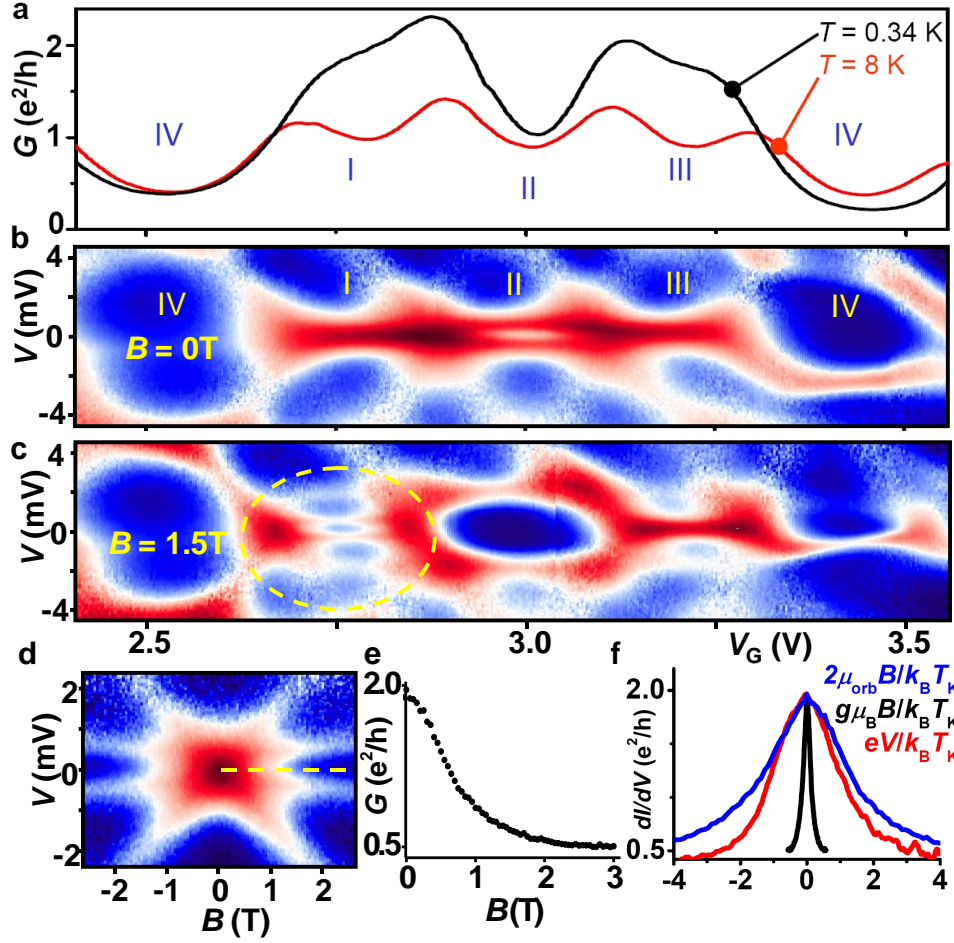


Figure 6.4: Spin \otimes orbital Kondo effect. **a**, Linear conductance, G , vs V_G at $T = 8$ K and 0.34 K. **b**, Color-scale plot of dI/dV vs (V, V_G) at $T = 0.34$ K and $B = 0$ (dI/dV increases from blue to red). **c**, Same as **b**, but at $B = 1.5$ T. The circle indicates the 4-fold splitting in region I. **d**, Color-scale plot of dI/dV versus (V, B) in the center of Coulomb valley I. The Kondo peak appears as a bright spot at $(V, B) = (0, 0)$, and splits in 4 peaks at finite B , following the simultaneous splitting of the orbital and spin states. **e**, B -dependence of G taken from the zero-bias dashed yellow line in **d**. G decreases on a ~ 0.5 T scale, i.e. ~ 12 times faster than expected from Zeeman splitting. **f**, G vs normalized Zeeman energy, $g\mu_B B/k_B T_K$ (black trace), and vs normalized orbital splitting, $2\mu_{orb} B/k_B T_K$ (blue trace). $T_K = 7.7$ K as deduced from a fit of $G(T)$. (Note that $G(B) = 0.5G(0)$ when $2\mu_{orb} B/k_B T_K \sim 1$). To compare the suppression due to B with the one due to V , we also show a measurement of dI/dV vs normalized bias voltage, $eV/k_B T_K$ (red trace). The blue and red traces fall almost on top of each other, implying that lifting the orbital degeneracy suppresses the Kondo effect. This demonstrates that the simultaneous degeneracy of orbital and spin states forms the origin of the strongly enhanced Kondo effect at $B = 0$.

induces a transition from SU(4) to a spin-based SU(2) Kondo effect for which $k_B T_K$ remains larger than the Zeeman energy, hindering the splitting of the Kondo resonance up to a few Tesla. Finally, we note that both the one-electron SU(4) and the two-electron singlet-triplet Kondo effects are characterized by a four-fold degeneracy, which results in an enhanced T_K [27]. Apart from this, the two phenomena are fundamentally very different. The singlet-triplet Kondo effect is a spin phenomenon in which the role of the orbital degree of freedom is simply to provide the basis for the construction of spin-singlet and triplet two-particle states (see also appendix).

Since orbital Kondo correlations can only arise if the orbital quantum number is conserved during tunneling, our experimental finding of orbital Kondo physics in CNT QDs raises an interesting question concerning the nature of the dot-lead coupling. In our devices, the metal contacts are deposited on top of the CNT and the QD is formed in the segment between them [29]. It is possible that when electrons tunnel out of the QD, they enter first the nanotube section underneath the contacts, where they dwell for some time before moving into the metal. Since the orbital quantum number is likely conserved in a CNT-CNT tunnel process, this intermediate step may account for the observed orbital Kondo effect.

We thank G. Zaránd, R. Aguado and J. Martinek for helpful discussions. Financial support is obtained from the Dutch organization for Fundamental Research on Matter (FOM), which is financially supported by the ‘Nederlandse Organisatie voor Wetenschappelijk Onderzoek’ (NWO).

References

- [1] Hewson, A. C. *The Kondo Problem to Heavy Fermions* (Cambridge University Press, Cambridge, 1993).
- [2] Goldhaber-Gordon, D. *et al.* Kondo effect in a single-electron transistor. *Nature* **391**, 156-159 (1998).
- [3] Cronenwett, S. M., Oosterkamp, T. H. & Kouwenhoven, L. P. A tunable Kondo effect in quantum dots. *Science* **281**, 540-544 (1998).
- [4] Schmid, J., Weis, J., Eberl, K. & von Klitzing, K. A quantum dot in the limit of strong coupling to reservoirs. *Physica B* **256-258**, 182-185 (1998).
- [5] Nygård, J., Cobden, D. H., & Lindelof, P. E. Kondo physics in carbon nanotubes. *Nature* **408**, 342-346 (2000).
- [6] Buitelaar, M. R. *et al.* Multi-wall carbon nanotubes as quantum dots. *Phys. Rev. Lett.* **88**, 156801 (2002).

-
- [7] Park, J. *et al.* Coulomb blockade and the Kondo effect in single-atom transistors. *Nature* **417**, 722-725 (2002).
- [8] Liang, W. *et al.* Kondo resonance in a single-molecule transistor. *Nature* **417**, 725-729 (2002).
- [9] Cox, D. L. & Zawadowski, A. Exotic Kondo effects in metals: magnetic ions in a crystalline electric field and tunnelling centers. *Adv. Phys.* **47**, 599-942 (1998).
- [10] Kolesnychenko, O. Yu., de Kort, R., Katsnelson, M. I., Lichtenstein, A. I. & van Kempen, H. Real-space imaging of an orbital Kondo resonance on the Cr(001) surface. *Nature* **415**, 507-509 (2002).
- [11] Inoshita, T., Shimizu, A., Kuramoto, Y. & Sakaki, H. Correlated electron transport through a quantum dot: the multiple-level effect. *Phys. Rev. B* **48**, 14725-14728 (1993).
- [12] Borda, L. *et al.* SU(4) Fermi liquid state and spin filtering in a double quantum dot system. *Phys. Rev. Lett.* **90**, 026602 (2003).
- [13] Zaránd, G., Brataas, A. & Goldhaber-Gordon, D. Kondo effect and spin filtering in triangular artificial atoms. *Solid State Comm.* **126**, 463-466 (2003).
- [14] López, R. *et al.* Probing spin and orbital Kondo effects with a mesoscopic interferometer. *Phys. Rev. B* **71**, 115312 (2005).
- [15] Sasaki, S. *et al.* Enhanced Kondo effect via tuned orbital degeneracy in a spin artificial atom. *Phys. Rev. Lett.* **93**, 017205 (2004).
- [16] Dresselhaus, M. S., Dresselhaus, G. & Eklund, P. C. *Science of Fullerenes and Carbon Nanotubes* (Academic Press, San Diego, 1996).
- [17] Minot, E., Yaish, Y., Sazonova, V. & McEuen, P.L. Determination of electron orbital magnetic moments in carbon nanotubes. *Nature* **428**, 536-539 (2004).
- [18] Ajiki, H. & Ando, T. Electronic states of carbon nanotubes. *J. Phys. Soc. Jpn* **62**, 1255-1266 (1993).
- [19] Zaric, S. *et al.* Optical signatures of the Aharonov-Bohm phase in single-walled carbon nanotubes. *Science* **304**, 1129-1131 (2004).
- [20] Coskun, U. C. *et al.* h/e magnetic flux modulation of the energy gap in nanotube quantum dots. *Science* **304**, 1132-1134 (2004).
- [21] Jarillo-Herrero, P. *et al.* Electronic transport spectroscopy of carbon nanotubes in a magnetic field. *Phys. Rev. Lett.* **94**, 156802 (2005).

-
- [22] Liang, W., Bockrath, M. & Park, H. Shell filling and exchange coupling in single-walled carbon nanotubes. *Phys. Rev. Lett.* **88**, 126801 (2002).
- [23] De Franceschi, S. *et al.*, Electron cotunneling in a semiconductor quantum dot. *Phys. Rev. Lett.* **86**, 878-881 (2001).
- [24] Paaske, J., Rosch, A. & Wölfle, P. Nonequilibrium transport through a Kondo dot in a magnetic field: perturbation theory. *Phys. Rev. B* **69**, 155330 (2004).
- [25] Pasupathy, A. N. *et al.* The Kondo effect in the presence of ferromagnetism. *Science* **306**, 86-89 (2004).
- [26] Costi, T. A. Kondo effect in a magnetic field and the magnetoresistivity of Kondo alloys. *Phys. Rev. Lett.* **85**, 1504-1507 (2000).
- [27] Sasaki, S. *et al.* Kondo effect in an integer-spin quantum dot. *Nature* **405**, 764-767 (2000).
- [28] Choi, M.-S., López, R. & Aguado, R. SU(4) Kondo effect in carbon nanotubes. *Phys. Rev. Lett.* **95**, 067204 (2005).
- [29] Mann, D. *et al.* Ballistic transport in metallic nanotubes with reliable Pd ohmic contacts, *Nano Lett.* **3**, 1541-1544 (2003).
- [30] Bonet, E., Deshmukh, M. M. & Ralph, D. C. Solving rate equations for electron tunneling via discrete quantum states. *Phys. Rev. B* **65**, 045317 (2002).
- [31] A zero bias anomaly in the context of an orbital degeneracy has been discussed by Wilhelm, U., Schmid, J., Weis, J. & Klitzing, K.v. Experimental evidence for spinless Kondo effect in two electrostatically coupled quantum dot systems. *Physica (Amsterdam)* **14E**, 385 (2002). No temperature or magnetic field dependence data were reported, precluding a direct comparison with predictions for Kondo effect.
- [32] Eto, M. Enhancement of Kondo effect in multilevel quantum dots. E-Print available at <http://xxx.lanl.gov/abs/cond-mat/0408159>.
- [33] van der Wiel, W.G. *et al.* Two-stage Kondo effect in a quantum dot at a high magnetic field. *Phys. Rev. Lett.* **88**, 126803 (2002).
- [34] Pustilnik, M., Avishai, Y. & Kikoin, K. Quantum dots with even number of electrons: Kondo effect in a finite magnetic field. *Phys. Rev. Lett.* **84**, 1756-1759 (2000).
- [35] Giuliano, D. & Tagliacozzo, A. Spin fractionalization of an even number of electrons in a quantum dot. *Phys. Rev. Lett.* **84**, 4677 (2000).

- [36] Eto, M. & Nazarov, Yu.V. Enhancement of Kondo effect in quantum dots with an even number of electrons. *Phys. Rev. Lett.* **85**, 1306-1309 (2000).
- [37] Pustilnik, M. & Glazman, L.I. Conduction through a quantum dot near a singlet-triplet transition. *Phys. Rev. Lett.* **85**, 2993 (2000).
- [38] Pustilnik, M. & Glazman, L.I. Kondo effect in real quantum dots. *Phys. Rev. Lett.* **87**, 216601 (2001).
- [39] Izumida, W., Sakai, O. & Tarucha, S. Tunneling through a quantum dot in local spin singlet-triplet crossover region with Kondo effect. *Phys. Rev. Lett.* **87**, 216803 (2001).
- [40] Hofstetter, W. & Schoeller, H. Quantum Phase Transition in a Multilevel Dot. *Phys. Rev. Lett.* **88**, 16803 (2001).
- [41] Pustilnik, M., Glazman, L.I. & Hofstetter, W. Singlet-triplet transition in a lateral quantum dot. *Phys. Rev. B* **68**, 161303(R) (2003).
- [42] Hofstetter, W. & Zaránd, G. Singlet-triplet transition in lateral quantum dots: A numerical renormalization group study. *Phys. Rev. B* **69**, 235301 (2004).
- [43] Golhaber-Gordon, D. *et al.*, From the Kondo regime to the mixed-valence regime in a single-electron transistor. *Phys. Rev. Lett.* **81**, 5225 (1998).

6.4 Appendix

This appendix contains extensive additional discussion and some more data, and was published as Supplementary Information to the main text.

Orbital degeneracy & Kondo effect

In this section we explain the similarities and differences between the following types of Kondo effect that arise in the presence of an orbital degeneracy: two-level spin Kondo effect (TLS-Kondo), orbital Kondo effect (O-Kondo), SU(4) Kondo effect and singlet-triplet Kondo effect (ST-Kondo).

The presence of a degeneracy in the ground state is essential to all Kondo effects. In a QD, the simplest Kondo effect occurs for the case of a single electron in a spin-degenerate ($s=1/2$) orbital level [2, 3, 4]. A degeneracy may also arise from degenerate orbitals. If this orbital degree of freedom is conserved during tunneling, then the orbital quantum number can behave as a spin, and one uses the term ‘pseudospin’. The quantum fluctuations of this pseudospin can give rise to an O-Kondo [9, 10, 31] effect similar to the usual spin $1/2$ Kondo effect.

In the main text we study the Kondo effect that arises from this orbital pseudospin for a single electron in a CNT QD. This pseudospin gives rise to SU(4)-Kondo when spin degeneracy is also present and to purely O-Kondo when spin degeneracy is removed. At zero field, spin and orbital pseudospin play an equivalent role and they entangle effectively with each other via cotunneling processes. Note that any of the four degenerate states is accessible via a first order cotunneling process from any of the other states (see Fig. 6.1c). As a result of this strong entanglement the state of the dot can be mapped onto a four-component ‘hyper-spin’ space where the Hamiltonian takes a highly symmetric form that transforms according to the SU(4) group [12, 13, 14]. We therefore denote the present effect as SU(4)-Kondo. The corresponding phase shift associated with the transmission of electrons across the dot is $\pi/4$. This sets an upper limit to the conductance of $G = 2e^2/h[\sin^2(1/2 \cdot \pi/2) + \sin^2(1/2 \cdot \pi/2)] = 2e^2/h$. It is worth noting that the same value for the maximum conductance is also obtained for the ordinary spin 1/2 and O-Kondo effects, but this time due to a $\pi/2$ phase shift and the corresponding symmetry is SU(2) ($G = 2e^2/h[\sin^2(1 \cdot \pi/2)] = 2e^2/h$) [11, 12, 13, 14, 15, 32].

The four-fold degeneracy in the SU(4)-Kondo effect leads to a Kondo temperature much higher than in the ordinary spin 1/2 case [11, 12, 13, 14, 15, 32]. A similar enhancement of T_K occurs for the TLS-Kondo and ST-Kondo effects, where the degeneracy is also four-fold. In these cases, however, the physics is fundamentally different. Basically none of these Kondo effects would exist for spinless electrons, while the SU(4)-Kondo would be reduced to an SU(2) orbital Kondo effect in the absence of spin.

The ST-Kondo effect occurs for two electrons in the dot, due to the degeneracy between two-particle singlet and triplet states. It was discovered in semiconductor quantum dots [27, 33] giving rise to extensive theoretical work [34, 35, 36, 37, 38, 39, 40, 41]. In the ST-Kondo effect the orbital degree of freedom does not act as a pseudospin. Instead, it simply provides the extra orbital necessary to form the two-particle triplet state. In contrast to the SU(4)-Kondo effect, here the 4 states for ST-Kondo are not all mutually connected via a first-order cotunneling process. For example, the $S_z = +1$ triplet state, $|\uparrow\uparrow\rangle$, cannot go to the triplet $S_z = -1$, $|\downarrow, \downarrow\rangle$ via a first order cotunneling process, since for this process $|\Delta S_z| = 2$. The symmetry of the ST-Kondo effect is not SU(4) as it can be deduced from the analysis of the corresponding phase shifts [41, 42]. It is worth noting that we also observe the ST-Kondo effect in our devices in the case when 2 electrons occupy a shell (this occurs at finite field, $B \sim 0.35$ T, for region II (not shown), and at zero field for the shell on the left side of Fig. 6.6). In our nanotube devices, as well as in semiconductor vertical quantum dots [27], the upper limit to the

conductance is $G = 4e^2/h$ [37, 39]. Consistent with this expectation we observe a Kondo-enhanced conductance larger than the one channel limit of $2e^2/h$ (note the peak conductance of $3e^2/h$ for the shell on the left in Fig. 6.6).

The TLS-Kondo and SU(4) Kondo effects are more difficult to distinguish experimentally at zero field. They occur both for a single electron in the dot. In both cases the upper limit to the conductance is $2e^2/h$ and there is a similar enhancement of T_K due to orbital degeneracy. Recent calculations [28] show that the distinction is possible at finite B because the Kondo resonance splits in two for TLS-Kondo (TLS-Kondo gives rise to no orbital Kondo resonance) while it splits in 6 for SU(4) Kondo. These results are in agreement with our experiments. Besides this, the Kondo effect at large B , due to the recovery of degeneracy between orbital states with equal spin polarization, proves the presence of orbital Kondo correlations in CNTs at zero field. Even in the presence of a coupling, δ , between orbital states, since $\delta < k_B T_K$ (at $B = 0$), the conditions for the observations of an SU(4) Kondo effect are fulfilled [12].

Single particle energy spectrum & $G(V_G, B)$ spectroscopy

In this section we show how we identify the orbital Kondo effect shown in Fig. 6.3 with the degeneracy between the equally polarized orbital states $|+, \downarrow\rangle$ and $|-, \downarrow\rangle$ (neglecting the orbital coupling). Figure 6.5a shows the same single particle energy spectrum as in Fig. 6.2d, where we have added the labels A, B, C and D. Δ is the energy spacing between consecutive shells. The diagrams in Fig. 6.5b represent the orbital and spin configuration of the CNT QD with one electron in the highest energy shell (the lower energy shells are fully occupied) at (E, B) positions A to D. In Fig. 6.5c, the correspondence between the single particle energy spectrum and a $G(V_G, B)$ diagram (representing the measurements shown in Fig. 6.3a) is shown. U is the charging energy.

At zero field (A), the electron occupies a four-fold degenerate state, giving rise to an SU(4) Kondo effect. This shows up in Fig. 6.5c as a conductance ridge inside the Coulomb blockade area. As the magnetic field is increased, the degeneracy is broken (B) and the electron occupies the lowest energy level, that is $|-, \uparrow\rangle$. At C, there is a level crossing between states $|-, \uparrow\rangle$ and $|+, \downarrow\rangle$. Due to the exchange interaction, the kink in the B -evolution of the corresponding Coulomb peak appears at a lower value of the magnetic field (C' in Fig. 6.5b,c), when the single particle states have not crossed yet. This kink denotes a singlet to triplet transition in the region where the QD is occupied by four electrons (full shell). The singlet-triplet transition for a full shell occurs because one of the two electrons in energy level $|+\rangle$ (specifically $|+, \downarrow\rangle$) promotes to energy level

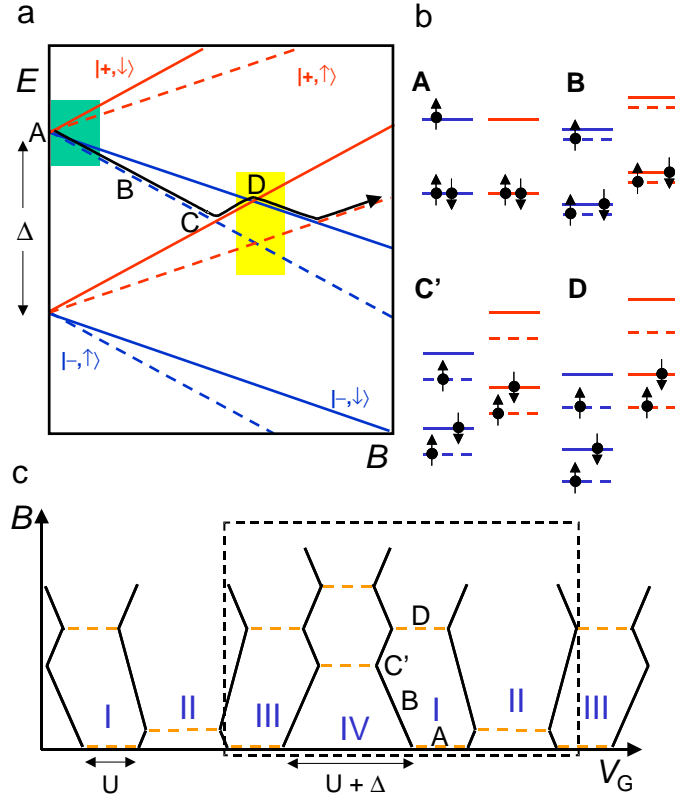


Figure 6.5: Single particle energy spectrum & $G(V_G, B)$ spectroscopy (see text).

$|-, \uparrow\rangle$ (from the next unoccupied shell) as soon as their energy difference is less than the exchange interaction. An enhanced conductance ridge is observed correspondingly (see also Fig. 6.3a). From C' on, the last added electron to the QD occupies the state $|+, \downarrow\rangle$, until a new level crossing occurs at D, between $|+, \downarrow\rangle$ and $|-, \downarrow\rangle$. Here the single electron can occupy any of the two orbital states, but in both cases with spin down. A purely orbital Kondo effect can then take place and a conductance ridge is seen (see Fig. 6.5c and Fig. 6.3a). A similar Kondo effect can take place in region III. In this case, however, Kondo effect takes place between states $|+, \uparrow\rangle$ and $|-, \uparrow\rangle$. In a clean CNT, without disorder, this Kondo effect should take place at the same magnetic field value. Therefore a gate controlled bipolar low-impedance spin filter can, in principle, be realized [12]. By changing the gate voltage (from region I to III), we can change the filter polarity while the enhanced conductance due to Kondo effect ensures the low impedance.

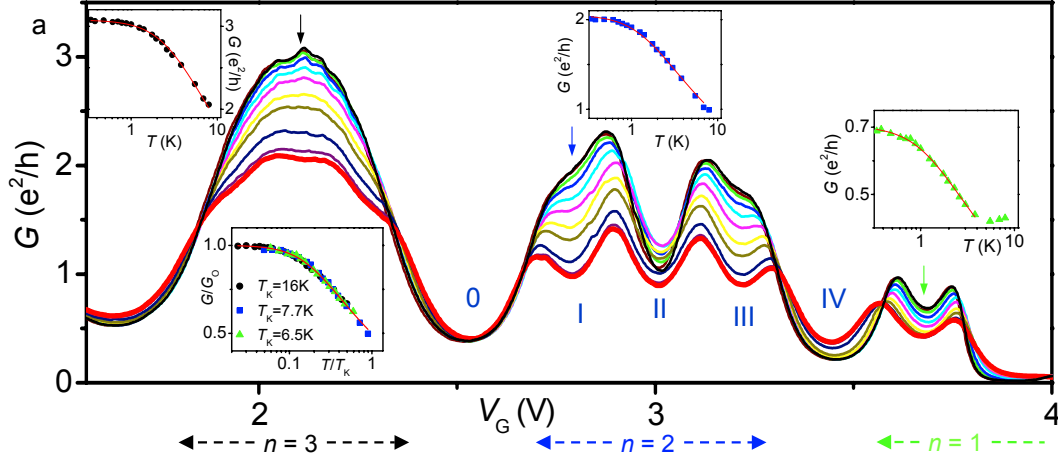


Figure 6.6: Temperature dependence of the linear conductance G (see text).

Temperature dependence

Here we show the T -dependence of the linear conductance data shown in Fig. 6.4a at $B = 0$ (Fig. 6.6). Starting from $T = 8$ K (thick red trace), G increases by lowering T in the regions corresponding to partially filled shells and decreases for full shells. In the center of valleys I and III, G exhibits a characteristic logarithmic T -dependence with a saturation around $2e^2/h$ at low T , indicating a fully-developed Kondo effect (see Fig 6.6, top central inset). Similar T -dependences, although with different values of G_0 and T_K , are observed for the neighbouring shells. The coupling to the leads increases as V_G decreases (the measurements are taken on the ‘valence band’ of the small band gap) [21]. From fits to the formula $G = G_0/(1 + (2^{1/s} - 1)(T/T_K)^2)^s$ [43], with $s=0.21$, taken at the V_G values indicated by arrows in Fig. 6.6, we find $T_K = 6.5, 7.7,$ and 16 K, respectively. These Kondo temperatures are an order of magnitude higher than those previously reported for nanotube QDs [5, 6] and comparable to those reported for single-molecule devices [7, 8]. Such high T_K values, and the fact that G exceeds $2e^2/h$ (the one-channel conductance limit) for two particles, are signatures of non-conventional Kondo effects (see Orbital degeneracy & Kondo effect above). The bottom inset in Fig. 6.6 shows the normalized conductance, G/G_0 , versus normalized temperature, T/T_K , for different shells and for both one and two electrons in the shell. The observed scaling reflects the universal character of the Kondo effect. The low-temperature behaviour is fully determined by a single energy scale, T_K , independent of the spin and orbital configuration responsible for the Kondo effect.

Chapter 7

Quantum supercurrent transistors in carbon nanotubes

P. Jarillo-Herrero, J. A. van Dam, and L. P. Kouwenhoven

Electronic transport through nanostructures is greatly affected by the presence of superconducting leads [1, 2, 3]. If the interface between the nanostructure and the superconductors is sufficiently transparent, a dissipationless current (supercurrent) can flow through the device due to the Josephson effect [4, 5]. A Josephson coupling, as measured via the zero-resistance supercurrent, has been obtained via tunnel barriers, superconducting constrictions, normal metals, and semiconductors. The coupling mechanisms vary from tunneling to Andreev reflection [6, 7, 8, 5]. The latter process has always occurred via a normal-type system with a continuous density of states. Here we investigate a supercurrent flowing via a discrete density of states, i.e., the quantized single particle energy states of a quantum dot [9], or artificial atom, placed in between superconducting electrodes. For this purpose, we exploit the quantum properties of finite-sized carbon nanotubes [10] (CNTs). By means of a gate electrode, successive discrete energy states are tuned ON and OFF resonance with the Fermi energy in the superconducting leads, resulting in a periodic modulation of the critical current and a non-trivial correlation between the conductance in the normal state and the supercurrent. We find, in good agreement with existing theory [11], that the product of the critical current and the normal state resistance becomes an oscillating function, in contrast to being constant as in previously explored regimes.

This chapter has been submitted to Nature.

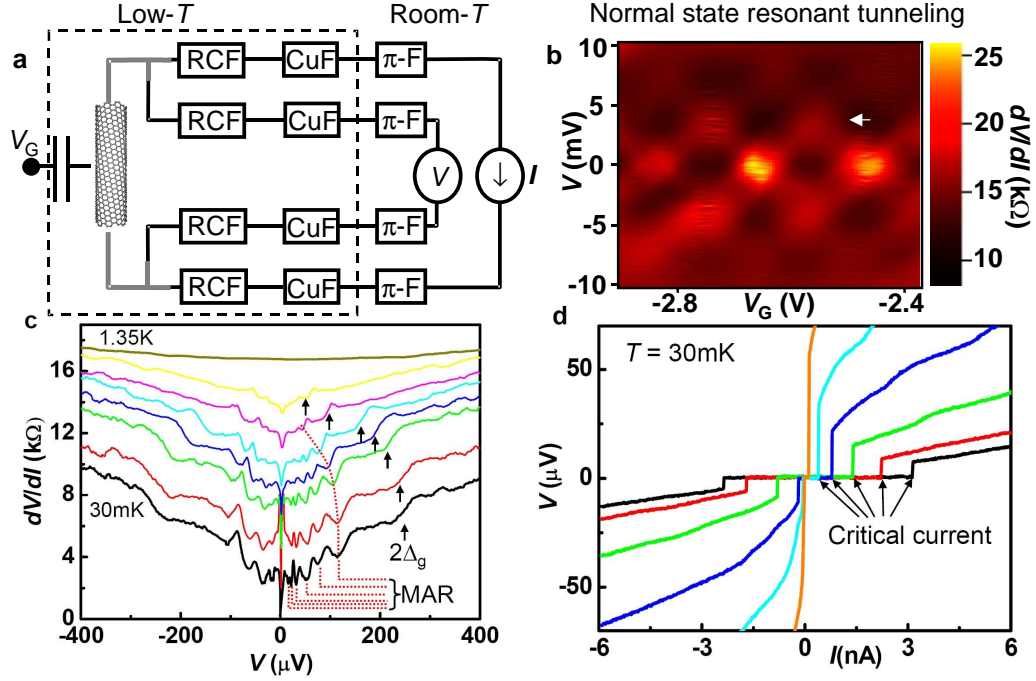


Figure 7.1: Measurement scheme and basic sample characterization. **a**, Diagram showing the measurement circuit. Grey represents Ti/Al electrodes (10nm/60nm). Titanium ensures a good electrical contact to the CNT, while aluminium becomes superconducting below $\sim 1.3\text{K}$, well above the base temperature of our dilution refrigerator. The CNTs are probed in a four-terminal geometry (current bias, voltage measurement). An important element is the incorporation of three sets of filters for each measurement wire: a copper-powder filter (Cu-F) for high frequency noise, π -filters for intermediate frequencies and a two-stage RC filter to suppress voltage fluctuations at low frequencies. The dashed box region indicates the low temperature part of the circuit. The rest is at room temperature. **b**, Color-scale plot of the differential resistance, dV/dI , versus measured voltage, V , and gate voltage, V_G at $T = 4.2\text{ K}$. The white arrow indicates the energy separation between discrete quantum levels in the CNT. **c**, Differential resistance versus measured source-drain voltage, V , at different temperatures (0.030, 0.47, 0.7, 0.88, 1.02, 1.18, 1.22 and 1.35 K, from bottom to top). The curves are offset for clarity (by $2\text{k}\Omega$, for 0.47 and 0.7 K, and by $1\text{k}\Omega$ for the rest). The features present in all curves below 1.3 K are due to the induced superconducting proximity effect. The arrows indicate the superconducting gap at $V = 2\Delta_g/e \sim 250\mu\text{V}$. The dotted lines indicate multiple Andreev reflection (MAR) processes, which manifest as dips in dV/dI . **d**, $V(I)$ -characteristics at base temperature showing the modulation of the critical current, I_C , with V_G ($V_G = -2.59, -2.578, -2.57, -2.563, -2.555$ and -2.541 V from black to orange). For currents larger than I_C the system goes into a resistive state (abrupt jump from zero to finite V).

7.1 Introduction

In artificial atoms current can flow via discrete states according to the general process of resonant tunneling, i.e., resonant when the Fermi energy in the leads is aligned with discrete energy states [9]. The maximum conductance, G , through a single spin-degenerate energy level depends on the coupling to the leads. For the case of phase-coherent tunneling, G can reach $2e^2/h$, when charging effects are unimportant. If charging effects are significant, still $G = 2e^2/h$ can be achieved (even off-resonance) by means of the Kondo effect [12], which establishes spin coherence between the quantum dot (QD) and the leads. An entirely new situation arises in the case of superconducting leads, i.e., when two superconductors are coupled via a discrete single particle state. As we show below, the conductance can reach infinity, that is, a supercurrent can flow through the QD. So, far beyond the perfect conductance level of $2e^2/h$ occurring when the transmission probability reaches one. This zero resistance state is peculiar since just a single discrete state, that can be occupied only with two spin degenerate electrons simultaneously, is available for coupling the collective macroscopic states in the leads. In contrast to previously accessible regimes, we can study Josephson coupling for ON and OFF resonant tunneling, which enables a transistor-like control of the supercurrent through the quantum dot.

The carbon nanotube devices are fabricated by means of standard nanofabrication techniques and geometries (e-beam lithography to define customized electrodes on CNTs grown by chemical vapour deposition on top of oxidized silicon substrates [13] with two extra important ingredients: the choice of superconducting material and a multiple-stage filtering system to suppress electronic noise over a wide frequency range (see Fig. 7.1a and appendix for details).

7.2 Quantum supercurrent transistor action

The quantum behaviour of electrons in carbon nanotubes in good contact with metallic electrodes emerges clearly in a measurement of the differential resistance, dV/dI , versus measured source-drain voltage, V and gate voltage, V_G , as shown in Fig. 7.1b for one of our devices in the normal state. The differential resistance exhibits a pattern of high and low conductance regions, typical of nanotube devices well coupled to the leads [14, 15], with a characteristic voltage scale, $V \sim 3.5$ mV. This energy corresponds to the energy level separation between the discrete electronic states due to the finite length of the CNT, $\Delta E = \hbar v_F/2L$, where \hbar is Planck's constant, $v_F = 8.1 \cdot 10^5$ m/s is the Fermi velocity in the CNT, and L its length. The value obtained from this measurement, $L \sim 480$ nm,

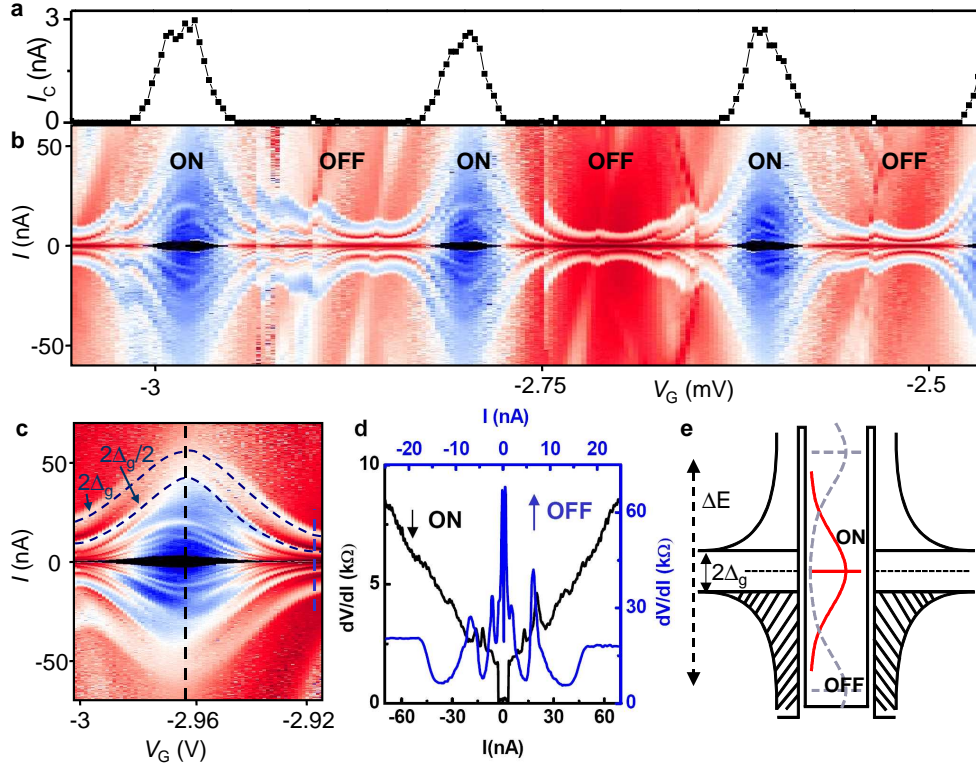


Figure 7.2: Quantum supercurrent transistor. **a**, Variation of the critical current, I_C , with gate voltage, V_G , extracted from **b** (see **c** and Fig. 7.3a for high resolution). I_C is measured as the upper half-width of the black region around $I = 0$. **b**, Color-scale representation (in log scale) of $dV/dI(I, V_G)$ at $T = 30$ mK (black is zero, i.e. supercurrent region, and dV/dI increases from dark blue to white and red; the scale can be inferred from **d**). Both dV/dI and I_C exhibit a series of quasiperiodic modulations with V_G as the energy levels in the CNT QD are tuned ON and OFF resonance with respect to the Fermi energy in the superconducting leads. The sharp vertical features are caused by random charge switches and shift the diagram horizontally. The narrow tilted features present in the OFF regions (for example at $V_G \sim -2.87$ V) occur reproducibly and are associated with Fano resonances [29] (see appendix). **c**, High-resolution $dV/dI(I, V_G)$ plot of the left-most resonance region in **b**. The modulation of I_C (black central region) as well as multiple Andreev reflection (up to several orders, the first two are highlighted by the dashed blue lines) are clearly visible. **d**, Two representative $dV/dI(I)$ curves, taken from **c** at the vertical black and blue dashed lines, illustrating the different behaviour of the differential resistance in the ON (black curve/axis) and OFF (blue curve/axis) resonance case. **e**, Schematic diagram showing a strongly coupled QD in between two superconducting leads. The gate voltage tunes the position of the Lorentzian level from the ON (red curve) to the OFF (grey dashed curve) state.

is in good agreement with the length of the nanotube segment in between the metallic electrodes, 470 nm. When the sample is cooled down below the superconducting critical temperature of the electrodes ($\sim 1.3\text{K}$), the electronic transport through the nanotube is strongly affected due to the superconducting proximity effect [1, 16, 17, 18, 19], which can be viewed as the leakage of Cooper pairs from a superconductor into a normal metal-type material. This proximity effect is evident from the observation of multiple Andreev reflections (MAR) [20] and the flow of a supercurrent through the device (Figs. 7.1c,d). We note that we have observed similar supercurrents in 4 out of 7 measured metallic CNT devices with room temperature resistances below $35\text{k}\Omega$ (see appendix for additional data and magnetic field dependence). The most interesting feature of this supercurrent is that its maximum value (critical current, I_C) can be strongly modulated by means of a gate electrode [21], as shown in Fig. 7.1d. Since the CNTs are metallic, this means that the supercurrent transistor action must have a different mechanism than in conventional semiconductor structures. It is also remarkable that the gate voltage necessary to change from maximum to minimum I_C is of only $\sim 50\text{ mV}$, much smaller than the typical gate voltages necessary to significantly vary the charge density of semiconducting carbon nanotubes [22] or nanowires with similar geometries [23].

In order to establish the origin of the modulation of I_C , it is important to characterize the sample over a larger gate voltage range. A measurement of $dV/dI(I, V_G)$ (Fig. 7.2b) shows a non-monotonic, quasi-periodic set of low differential resistance regions, where I_C is largest, in between regions of high dV/dI , where I_C is strongly suppressed (Fig. 7.2a). This pattern follows closely the low-bias pattern of Fig. 7.1b, but now the vertical axis is current, instead of voltage. The correspondence between the two patterns indicates that the modulation of I_C is due to the tuning ON and OFF resonance with gate voltage of the energy levels in the CNT with respect to the Fermi energy in the leads (as shown schematically in Fig. 7.2e). Such Josephson transistor mechanism, purely due to the discrete nature of the energy levels in a nanostructure (in this case finite-sized CNTs), has not been previously observed.

Before turning to a more quantitative description, we note that the modulation of I_C is followed by a series of dV/dI peaks and dips moving up and down in the current axis. These are better seen in the high-resolution measurement shown in Fig. 7.2c and reflect the multiple Andreev reflection processes (see also Fig. 7.1c) taking place at the CNT-metal interfaces. MAR processes occur at voltages $V = 2\Delta_g/en$ (Δ_g is the superconducting energy gap, e is the electron charge, n an integer number). The dV/dI curves in fact occur at constant voltage in this current-biased sample (see appendix). Two individual dV/dI traces

are shown in Fig. 7.2d for the ON and OFF resonance situations. In both cases dV/dI exhibits oscillations due to MAR, but the overall behaviour of dV/dI is very different. In the ON resonance case, dV/dI decreases with decreasing $|I|$ (on average) until it “switches” to zero when $\sim I_C$ is reached. For the OFF case, dV/dI increases with decreasing $|I|$ (except at the MAR points), until $|I|$ reaches a very strongly suppressed value of I_C (barely visible in Fig. 7.2d, see Fig. 7.3). From the normal state resistance values in the ON and OFF resonant cases, we can conclude that the dV/dI changes between these qualitative behaviours at values of $dV/dI \sim h/(2e^2) \sim 13 \text{ k}\Omega$, i.e., once the resistance per channel of the CNT becomes of the order of the quantum of resistance (see also appendix).

7.3 Correlation between critical current and normal state conductance

The correlation between the critical current and the normal state resistance, R_N , is well studied in S - “normal metal” - S (SNS) structures. As a matter of fact, for short junctions in diffusive systems and ideal NS interfaces, $I_C R_N \sim \Delta_g/e$, i.e. constant [5]. The situation differs when one considers a single discrete energy level. In this case, the conductance is given by $G_N = (4e^2/h)T_{BW}$, where $T_{BW} = \Gamma_1\Gamma_2/((\epsilon_R/h)^2 + 0.25\Gamma^2)$ is the Breit-Wigner transmission probability, $\Gamma_{1,2}$ are the tunnel rates through the left/right barriers ($\Gamma = \Gamma_1 + \Gamma_2$), and ϵ_R is the energy of the resonant level relative to the Fermi energy in the leads. (Note that we have added a factor of 4 in G_N to account for the spin and orbital degeneracy of the CNT electronic states [10, 24, 15, 25].) Beenakker and van Houten [11] have studied the lineshape for the critical current in such a system. For the case of a wide resonance, $h\Gamma \gg \Delta_g$, they obtained $I_C = I_0[1 - (1 - T_{BW})^{1/2}]$, with $I_0 = 2e\Delta_g/h$. Experimentally, we can vary the position of the resonant level by means of a gate voltage, $\epsilon_R \propto V_G$, as shown for the normal state conductance in Fig. 7.3b. From the maximum value of $G_N \sim 3.8e^2/h$, we deduce a barrier asymmetry $\Gamma_1/\Gamma_2 \sim 0.64$. We use this to fit $I_C(V_G)$ and $G_N(V_G)$ (see Figs. 7.3a,b; red curves). Although the functional form is in good agreement with theory, the values for Γ , $\Gamma_I = 0.85 \text{ meV}/h$ and $\Gamma_G = 1.36 \text{ meV}/h$, obtained from the $I_C(V_G)$ and $G_N(V_G)$ fits, respectively, differ substantially. Also the value of I_0 that we measure, 4.15 nA, is much smaller than the theoretical value ($2e\Delta_g/h \sim 60 \text{ nA}$). Such low critical currents are reminiscent of the behaviour of small, underdamped, current-biased Josephson junctions [26], where the electromagnetic environment leads to a measured critical current, I_{CM} , much lower than the true critical current I_C . The dynamics of such a Josephson junction can be visualized as that of

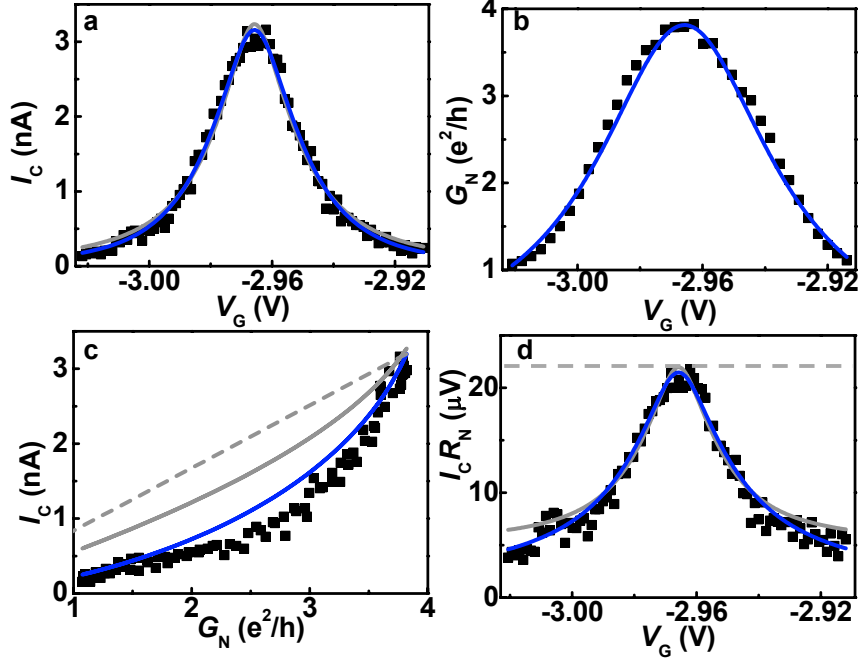


Figure 7.3: Correlation between critical current and normal state conductance and modulation of the $I_C R_N$ product. In all panels, the black dots represent the experimental data points ($T = 30$ mK) and the red/blue curves are theoretical plots. **a**, Critical current, I_C , versus V_G for the resonance shown in Fig. 2c. The theoretical lines are fits to $I_C = I_0[1 - (1 - \Gamma_1\Gamma_2/((V_G - V_{GR})^2 + 0.25\Gamma^2))^{1/2}]$ (red curve) and $I_{CM} = I_{0M}[1 - (1 - \Gamma_1\Gamma_2/((V_G - V_{GR})^2 + 0.25\Gamma^2))^{1/2}]^{3/2}$ (blue), as explained in the main text. V_{GR} is the value of gate voltage on resonance. All gate voltages and Γ 's are converted into energies by multiplying by the gate coupling factor, $\alpha = 0.02$ meV/mV, obtained from measurements in the non-linear regime. **b**, Conductance, G_N , as a function of V_G in the normal state ($B = 40$ mT) and the corresponding fit to $G_N = 4e^2/h\Gamma_1\Gamma_2/((V_G - V_{GR})^2 + 0.25\Gamma^2)$. **c**, $I_C - G_N$ correlation plot. The data show a non-trivial correlation, with a stronger decrease of I_C than expected from the theoretical curve $I_C = I_0[1 - (1 - 0.25G_N)^{1/2}]$ (red curve). The 0.25 factor simply denotes that G_N is measured in e^2/h units. The difference can be almost entirely accounted for by the influence of the electromagnetic environment, resulting in a measured $I_{CM} = I_0[1 - (1 - 0.25G_N)^{1/2}]^{3/2}$ (blue curve). An ideal SNS junction, with N a normal metal with continuous density of states, would exhibit a linear $I_C - G_N$ correlation curve (grey dashed curve). **d**, $I_C R_N$ product versus V_G , resulting from dividing the experimental data and theory curves from **a** and **b**. The grey dashed line indicates a constant $I_C R_N$ product such as in a SNS junction.

a particle moving in the so-called “tilted washboard” potential [5], where the driving current corresponds to the tilt in the potential. For the case of low

dissipation (underdamped junctions), a small fluctuation can cause the particle to slide down the potential and go into a “runaway” state. This occurs at a value of I much smaller than the true I_C , and it has been shown [26] that the measured critical current scales as $I_{CM} \propto (I_C)^{3/2}$. In order to test the applicability of this model to CNT Josephson junctions, we have fitted $I_{CM} = I_{0M}[1 - (1 - T_{BW}(V_G, \Gamma)^{1/2})^{3/2}]$, as shown by the blue curve in Fig. 7.3a. We obtain a similarly low value of $I_{0M} = 4.57$ nA and this time, the value of $h\Gamma_I$ obtained, 1.22 meV, is in good agreement with $h\Gamma_G = 1.36$ meV, resulting also in an improved fit to the data.

The importance of the coupling to the environment manifests itself more explicitly when examining the correlation between the critical current and the normal state conductance. We note that in the case of an ideal diffusive SNS junction the correlation would yield a simple straight line. The experimental data severely deviate from such curve (Fig. 7.3c). First we consider the expected theoretical decay for the case of a discrete state (red curve) $I_C = I_0[1 - (1 - 0.25G_N)^{1/2}]$ (no fitting parameters), with the value of I_0 obtained from Fig. 7.3a, and G_N measured in units of e^2/h . The comparison with the predicted theoretical line shows that the measured I_C is significantly lower than expected. However, a remarkably better agreement is found when the electromagnetic environment is included, as shown by the blue curve, $I_{CM} = I_0[1 - (1 - 0.25G_N)^{1/2}]^{3/2}$, indicating the generality of the $(I_C)^{3/2}$ dependence of I_{CM} for very different type of Josephson junctions [26].

The predicted lineshape of I_C (even in the presence of low dissipation) implies that the $I_C R_N$ product is not constant, but instead has a maximum on resonance. We plot in Fig. 7.3d the $I_C R_N$ product, which indeed exhibits a peak structure. The red and blue lines, which contain no extra fitting parameters, result from dividing the theoretical curves in Fig. 7.3a by the red curve in Fig. 7.3b, and further substantiate the results from earlier figures.

We emphasize that the above-mentioned analysis confirms the correct order of the relevant energy scales necessary for the observation of the resonant tunneling supercurrent transistor action [11]: ΔE (~ 3.5 meV) $>$ $h\Gamma$ (~ 1.3 meV) \gg Δ_g (~ 125 μ eV) $>$ U . The last inequality is justified since signatures of Coulomb blockade effects are absent in our data, concluding that the charging energy, U , is negligible.

We end by noting that, although both superconductivity and the Kondo effect are collective many-body phenomena, their effect on resonant tunneling is very different [18]. The Kondo enhancement occurs OFF-resonance, while the superconducting zero-resistance state, as we have shown, is most pronounced ON-resonance. In fact, we expect that the study of CNT devices with intermediate

transmission, and thus, larger Coulomb interactions, will enable the observation of Kondo-enhanced supercurrents in the OFF resonant case [27, 28].

We thank Yu.V. Nazarov, C.W.J. Beenakker, W. Belzig, S. De Franceschi and Y.-J. Doh for discussions and C. Dekker for the use of CNT growth facilities. Financial support obtained from the Japanese International Cooperative Research Project (ICORP) and the Dutch Fundamenteel Onderzoek der Materie (FOM).

References

- [1] de Gennes, P. G. Boundary Effects in Superconductors. *Rev. Mod. Phys.* **36**, 225-237 (1964).
- [2] Ralph, D. C., Black, C. T. & Tinkham, M. Spectroscopic Measurements of Discrete Electronic States in Single Metal Particles. *Phys. Rev. Lett.* **74**, 3241-3244 (1995).
- [3] von Delft, J. & Ralph, D. C. Spectroscopy of discrete energy levels in ultra-small metallic grains. *Phys. Rep.* **345**, 62-173 (2001).
- [4] Josephson, B. D. Possible New Effects in Superconductive Tunnelling. *Phys. Lett.* **1**, 251-253 (1962).
- [5] Tinkham, M. *Introduction to Superconductivity* (McGraw-Hill, Singapore, 1996).
- [6] Andreev, A. F. The Thermal Conductivity of the Intermediate State in Superconductors. *Sov. Phys. JETP* **19**, 1228-1231 (1964).
- [7] Likharev, K. K. Superconducting Weak Links. *Rev. Mod. Phys.* **51**, 101-159 (1979).
- [8] Blonder, G. E., Tinkham, M. & Klapwijk, T. M. Transition from Metallic to Tunneling Regimes in Superconducting Micro-Constrictions - Excess Current, Charge Imbalance, and Super-Current Conversion. *Phys. Rev. B* **25**, 4515-4532 (1982).
- [9] Sohn, L. L., Kouwenhoven, L. P., & Schön, G. (eds). *Mesoscopic Electron Transport* (Kluwer, Dordrecht, 1997).
- [10] Dresselhaus, M. S., Dresselhaus, G. & Eklund, P. C. *Science of Fullerenes and Carbon Nanotubes* (Academic Press, San Diego, 1996).
- [11] Beenakker, C. W. J. & van Houten, H. *Single-Electron tunneling and mesoscopic devices* (ed. Koch, H., Lbbig, H) (Springer, Berlin, 1992). (see also e-Print available at <http://xxx.lanl.gov/abs/cond-mat/0111505>).

- [12] Kouwenhoven, L. & Glazman, L. Revival of the Kondo effect. *Phys. World* **14**, 33-38 (2001).
- [13] Jarillo-Herrero, P. *et al.* Orbital Kondo effect in carbon nanotubes. *Nature (London)* **434**, 484-488 (2005).
- [14] Liang, W. J. *et al.* Fabry-Perot interference in a nanotube electron waveguide. *Nature (London)* **411**, 665-669 (2001).
- [15] Buitelaar, M. R., Bachtold, A., Nussbaumer, T., Iqbal, M. & Schönenberger, C. Multiwall carbon nanotubes as quantum dots. *Phys. Rev. Lett.* **88**, 156801 (2002).
- [16] Kasumov, A. Y. *et al.* Supercurrents through single-walled carbon nanotubes. *Science* **284**, 1508-1511 (1999).
- [17] Morpurgo, A. F., Kong, J., Marcus, C. M. & Dai, H. Gate-Controlled Superconducting Proximity Effect in Carbon Nanotubes. *Science* **286**, 263-265 (1999).
- [18] Buitelaar, M. R., Nussbaumer, T. & Schönenberger, C. Quantum dot in the Kondo regime coupled to superconductors. *Phys. Rev. Lett.* **89**, 256801 (2002).
- [19] Haruyama, J. *et al.* End-bonding multiwalled carbon nanotubes in alumina templates: Superconducting proximity effect. *Appl. Phys. Lett.* **84**, 4714-4716 (2004).
- [20] Buitelaar, M. R. *et al.* Multiple Andreev reflections in a carbon nanotube quantum dot. *Phys. Rev. Lett.* **91**, 057005 (2003).
- [21] Takayanagi, H. & Kawakami, T. Superconducting Proximity Effect in the Native Inversion Layer on InAs. *Phys. Rev. Lett.* **54**, 2449-2452 (1985).
- [22] McEuen, P. L. Single-wall carbon nanotubes. *Phys. World* **13**, 31-36 (2000).
- [23] Doh, Y. J. *et al.* Tunable supercurrent through semiconductor nanowires. *Science* **309**, 272-275 (2005).
- [24] Liang, W. J., Bockrath, M. & Park, H. Shell filling and exchange coupling in metallic single-walled carbon nanotubes. *Phys. Rev. Lett.* **88**, 126801 (2002).
- [25] Sapmaz, S. *et al.* Electronic excitation spectrum of metallic carbon nanotubes. *Phys. Rev. B* **71**, 153402 (2005).
- [26] Joyez, P., Lafarge, P., Filipe, A., Esteve, D. & Devoret, M. H. Observation of Parity-Induced Suppression of Josephson Tunneling in the Superconducting Single-Electron Transistor. *Phys. Rev. Lett.* **72**, 2458-2461 (1994).

- [27] Glazman, L. I. & Matveev, K. A. Resonant Josephson Current through Kondo Impurities in a Tunnel Barrier. JETP Lett. **49**, 659-662 (1989).
- [28] Choi, M. S., Lee, M., Kang, K., & Belzig, W. Kondo effect and Josephson current through a quantum dot between two superconductors. Phys. Rev. B **70**, 020502 (2004).
- [29] Babic, B. & Schönenberger, C. Observation of Fano resonances in single-wall carbon nanotubes. Phys. Rev. B **70**, 195408 (2004).
- [30] Zhang, Z., Dikin, D. A., Ruoff, R. S. & Chandrasekhar, V. Conduction in carbon nanotubes through metastable resonant states. Europhys. Lett. **68**, 713-719 (2004).
- [31] Fano, U. Effects of Configuration Interaction on Intensities and Phase Shifts. Phys. Rev. **124**, 1866-1878 (1961).
- [32] Kong, J., Soh, H. T., Cassell, A. M., Quate, C. F. & Dai, H. J. Synthesis of individual single-walled carbon nanotubes on patterned silicon wafers. Nature **395**, 878-881 (1998).
- [33] Li, Y. M. et al. Growth of single-walled carbon nanotubes from discrete catalytic nanoparticles of various sizes. J. Phys. Chem. B **105**, 11424-11431 (2001).
- [34] Cheung, C. L., Kurtz, A., Park, H. & Lieber, C. M. Diameter-controlled synthesis of carbon nanotubes. J. Phys. Chem. B **106**, 2429-2433 (2002).
- [35] Johansson, G., Bratus, E. N., Shumeiko, V. S. & Wendin, G. Resonant multiple Andreev reflections in mesoscopic superconducting junctions. Phys. Rev. B **60**, 1382-1393 (1999).

7.4 Appendix

This appendix contains some additional discussion and data, and has been submitted as Supplementary Information to the main text.

Filtering system

In this section we describe our filtering system. A filtering system is necessary to prevent electronic noise from reaching the sample (as much as possible) since this suppresses strongly the critical current. As mentioned in the main text we use three filters in series for each of the four measurement wires attached to a nanotube: a copper-powder filter (CuF), a π -filter and a two-stage RC filter

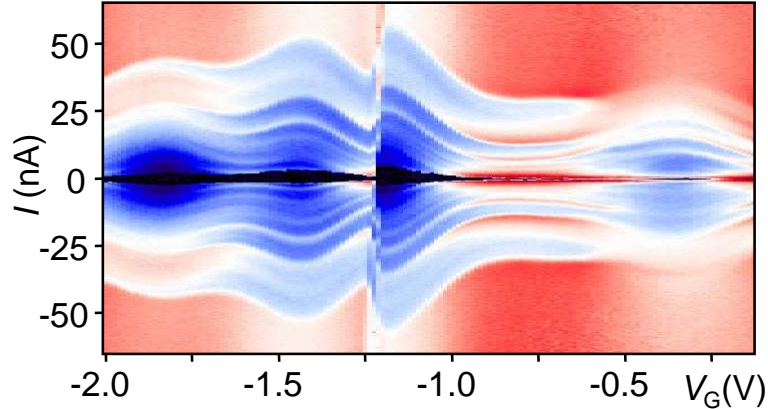


Figure 7.4: Differential resistance versus V and V_G for a different device. Black means zero and dI/dV increases from blue to red.

(RCF). Three filters are used in order to cover the entire spectrum, from low frequency up to the microwave regime. CuFs are widely used in dilution refrigerator measuring setups. They are typically used to suppress the high frequency noise ($f \geq 1$ GHz), lowering the effective electron temperature. Our CuF filters consist of ~ 1.5 m long manganine wires, and give an attenuation ≥ 50 dB at 1 GHz. The π -filters cover the intermediate frequency range (~ 10 MHz - 2 GHz). The two-stage RC filters are useful in the range few kHz - 100 MHz and are widely used to measure small critical currents. The advantage of a two-stage versus a single stage RC filter is that it provides an attenuation of 40 dB per decade (instead of 20 dB/decade) above a certain cut-off frequency. An example of a used configuration is: $R_1 = 820 \Omega$, $R_2 = 1.2$ k Ω ; $C_1 = 20$ nF, $C_2 = 4.7$ nF, which gives a cut-off frequency in the ~ 10 kHz range.

Additional data & Fano resonances

Here we show additional data from a different device. Figure 7.4 shows a dV/dI versus (I, V_G) plot, similar to Fig. 7.2b. Both multiple Andreev reflection and a modulation of the critical current as a function of gate voltage are clearly visible.

In the center of the figure a sharp resonance can be seen, similar also to the sharp resonances in Fig. 7.2b. Such resonances have been observed and discussed in the context of carbon nanotubes strongly coupled to the leads [30, 29] and attributed to Fano resonances [31], although their origin have not been fully established. Two interfering channels are needed for Fano resonances to occur, a strongly coupled one and a weakly coupled one. The weakly coupled one can be

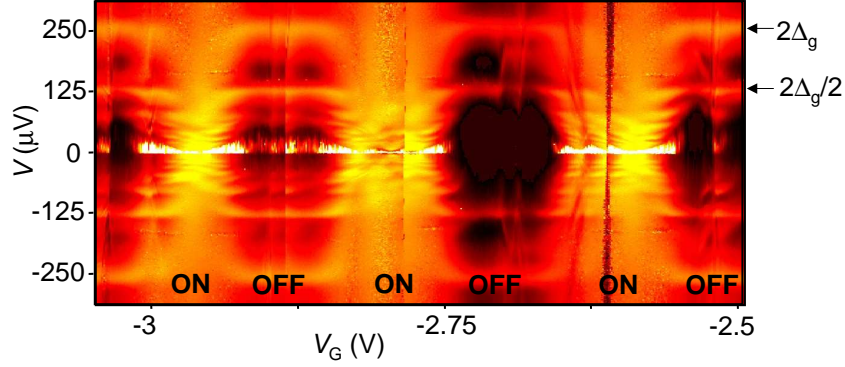


Figure 7.5: Differential conductance versus V and V_G for the data shown in 7.2b. The horizontal features at $2\Delta_g$ and $2\Delta_g/2$ are due to MAR.

an impurity, an inner shell in a multiwall tube or a weakly coupled tube in a thin rope. It has also been suggested that intrinsic resonances may arise for individual single wall tubes [29], due to an asymmetric coupling of the two orbital channels in carbon nanotubes. We have examined the diameters of our samples and they are in the 2 to 7 nm range. While single wall nanotubes of 2-3 nm are usually obtained with our CVD growth method [32], a diameter like 7 nm is more rare. We note however that single wall NTs grown by CVD up to 13 nm in diameter have been reported [33, 34]. Therefore it cannot entirely be excluded that the Fano resonances are due to the fact that those tubes measured are not individual single wall tubes. Nevertheless, the conductance of our devices in the normal state gets very close to, but doesn't exceed, $4e^2/h$, similar to Ref. [29]. Future studies are necessary to clarify the precise origin of the Fano resonances.

Multiple Andreev Reflection

In order to visualize the regions of supercurrent flow, figure 7.2 shows differential resistance plots as a function of current bias. Because of this, the multiple Andreev reflection (MAR) lines move up and down along the plots (e.g., Fig. 7.2b,c). Figure 7.5 shows the differential conductance, dI/dV (in log scale), versus measured source-drain voltage and gate voltage (black/dark red is low dI/dV and yellow is high dI/dV , the white features at low V are due to the conversion from current biased to voltage biased near supercurrent). The features in Fig. 7.5 are in good agreement with previous MAR results in carbon nanotubes [20]. For example, the Andreev reflection peaks at $2\Delta_g$ and $2\Delta_g/2$ are clearly visible OFF resonance, while they become smeared ON resonance. Also, as predicted theoretically [20, 35], the subgap structure becomes very complex in

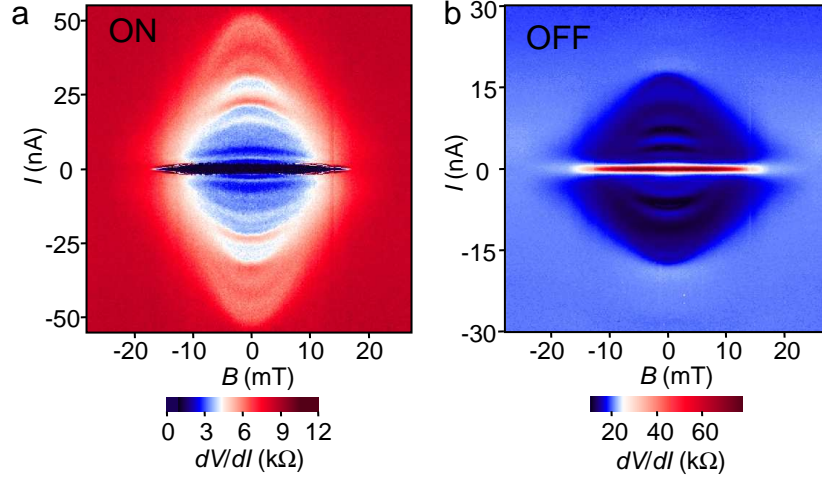


Figure 7.6: Differential resistance versus I and B showing the suppression of the proximity effect for the ON (a) and OFF (b) resonance case.

the vicinity of the resonances.

Magnetic field dependence

The application of a magnetic field, B , suppresses superconductivity in the electrodes and, thus, suppresses the proximity effect associated-features in the transport through the nanotube. As an example we show in Figs. 7.6a,b the suppression of MAR and I_C with B (shown for the device in Fig. 7.4; other devices exhibit the same behaviour). Figure 7.6a corresponds to the ON resonance case, while fig. 7.6b corresponds to the OFF resonance case. As mentioned in the main text, the differential resistance in the ON-resonance case is lower when the leads are superconducting. On the other hand, in the OFF-resonance case, there is a large ‘peak’ in dV/dI at low energies. [Note that the vertical scale is very different for the two figures.] Similar peaks in dV/dI (although smaller in magnitude) have been observed previously [17] and attributed to electron-electron interactions. While we cannot rule out such effects (for example a small Coulomb interaction effect), it has been shown [20] that a non-interacting model which takes into account only a resonant level in between two superconducting leads, can yield also such an enhancement of the differential resistance at low energies in the OFF-resonance case. A more detailed study, both theoretical and experimental, should shed light on the relative importance of each of the possible effects accounting for these peaks.

Chapter 8

Tunneling in suspended carbon nanotubes assisted by longitudinal phonons

S. Sapmaz, P. Jarillo-Herrero,
Ya. M. Blanter, C. Dekker, and H.S.J. van der Zant

Current-voltage characteristics of suspended single-wall carbon nanotube quantum dots show a series of steps equally spaced in voltage. The energy scale of this harmonic, low-energy excitation spectrum is consistent with that of the longitudinal low- k phonon mode (stretching mode) in the nanotube. Agreement is found with a Franck-Condon-based model in which the phonon-assisted tunneling process is modeled as a coupling of electronic levels to underdamped quantum harmonic oscillators. Comparison with this model indicates a rather strong electron-phonon coupling factor of order unity.

8.1 Introduction

In nano-electromechanical systems (NEMS), mechanical motion affects electrical current and vice versa [1, 2, 3, 4]. Of special interest is the study of electron-phonon coupling in these devices since tunneling of a single electron may induce a displacement of the movable structure [5, 6, 7, 8, 9, 10]. The interaction strength is characterized by the dimensionless electron-phonon (e-ph) coupling constant g , which is proportional to the ratio of the classical and the quantum displacement. In bulk systems the e-ph coupling is generally weak and the coupling constant is orders of magnitude smaller than one. However, since the coupling dramatically increases with decreasing device mass, NEM-devices may exhibit an intermediate to strong e-ph coupling [11, 12, 13]. In this regime, current-voltage characteristics are expected to exhibit additional steps whose height can be used as an estimate of g . For example, g is around one in the C_{60} molecular devices of Ref. [11], while measurements on different C_{140} samples [12] indicate a value of g between 0.2 and 8.

Carbon nanotubes (NTs) are ideal systems for exploring electro-mechanical effects since they have a small diameter, a low mass, and can be defect free on a molecular level. In experiments on suspended nanotubes, different methods have already been used to probe the bending [14, 15] and radial breathing mode (RBM) [16]. The measurements show that the free-hanging tubes operate in the underdamped regime of low dissipation. For the fundamental bending mode the reported quality factor is about 100; for the RBM it is estimated as high as 10000.

Here we present electronic transport spectroscopy measurements on suspended carbon nanotubes, which show signatures of phonon-assisted tunneling, evidenced by the presence of a series of steps in the $I - V$ characteristics. Such steps form a harmonic low-energy spectrum, whose energy scale and length dependence are consistent with that of the longitudinal stretching mode. Comparison with the Franck-Condon theory shows that the e-ph coupling constant is of order one.

Devices are fabricated by locating individual nanotubes (laser ablation and CVD) on a Si/SiO₂ substrate using an atomic force microscope (AFM) with respect to predefined markers. Subsequently, the electrodes are made using conventional e-beam lithography techniques and thermal evaporation of Cr (5 nm) and Au (50 nm). The nanotubes are suspended by removing the underlying SiO₂ in a wet etch step using buffered HF [17]. A schematic sample geometry and SEM micrograph are shown in Fig. 8.1. In the experiment the source and gate voltage are defined with respect to the drain, which is connected to ground.

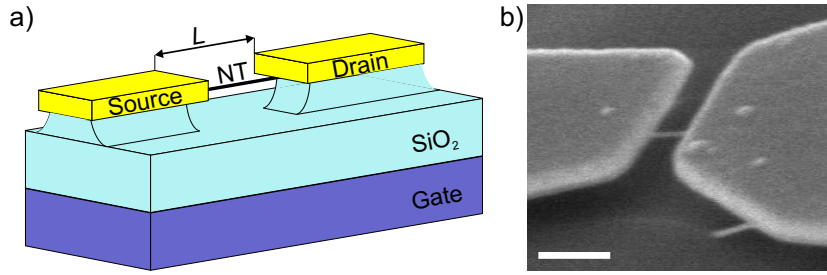


Figure 8.1: (a) Schematic drawing of a suspended nanotube clamped between two Cr/Au electrodes on top of silicon oxide. The underlying oxide is partially removed by a wet etch step leaving the nanotube suspended. The highly doped silicon plane is used as a global gate to tune the electrostatic potential of the nanotube. (b) Scanning-electron microscope micrograph of a suspended nanotube. The scale-bar represents 200 nm.

8.2 Stability diagrams and low-energy spectra

In Fig. 8.2 we show stability diagrams for three nanotubes measured at 10 mK (a) and 300 mK (b,c) where the differential conductance, dI/dV , is plotted versus bias and gate voltage. The three metallic nanotubes have a length between source and drain contacts, L , ranging from 0.14 to 1.2 μm . Their diameter d is between 1 and 1.4 nm as determined from AFM imaging. In the diamond shaped regions (Coulomb diamonds) the current is zero due to Coulomb blockade, and the charge number in the dot is fixed. Regular and closing Coulomb diamonds indicate single dot behavior [18, 19] in all three samples for the gate range shown. Notice that the diamonds in Fig. 8.2a do close, as shown in the inset, which was taken at a higher temperature (300 mK) in a different cooldown. The low-bias current, however, is suppressed which could be a signature of strong electron-phonon coupling [5, 9, 10].

Excitations of a quantum dot appear as lines running parallel to the Coulomb diamond edges in the stability diagrams [18]. At such a line, a new electronic level becomes resonant with the leads and an additional transport channel opens up. The energy of an excitation can be determined by reading off the intersection point between the excitation line and the Coulomb diamond edge on the bias axis [19]. Furthermore, the excitations correspond to the charge state of the Coulomb diamond they end up in. Electronic excitations in nanotubes typically differ between adjacent charge states [20]. In Fig. 8.2a, a dense set of equally spaced excitation lines (starting from the first electronic excitation) is clearly visible near $V_G = 210$ mV and 230 mV, i.e., adjacent charge states exhibit a similar set of excitations with approximately the same energy spacing. The fact

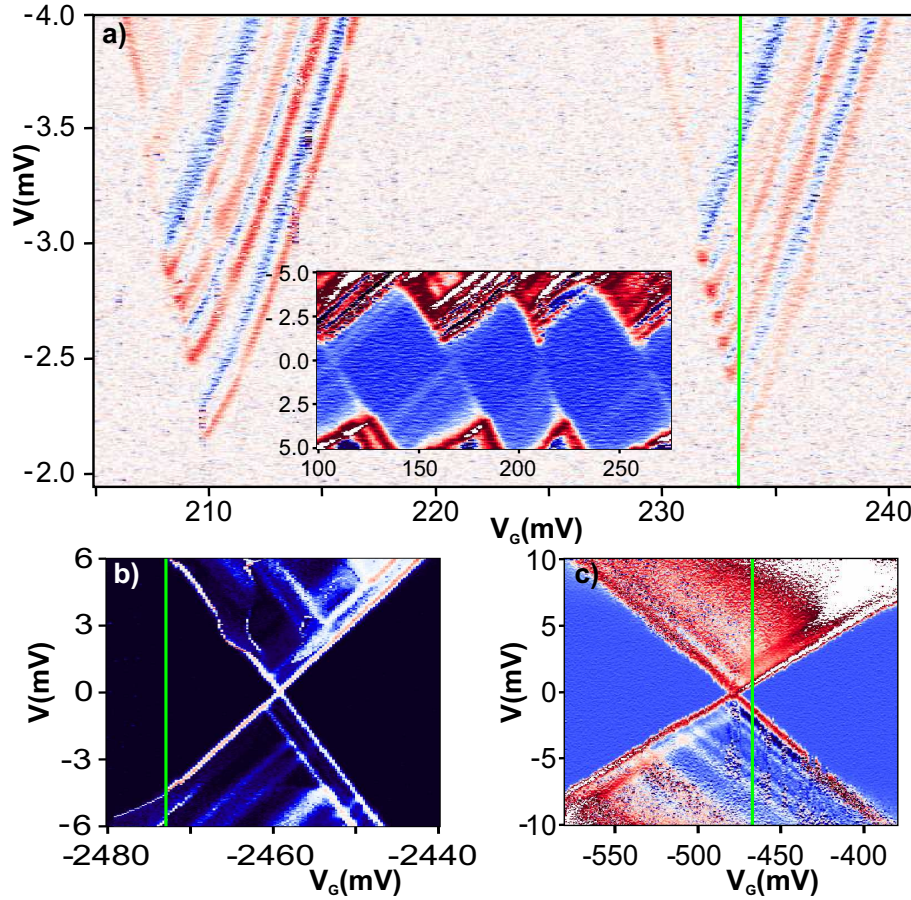


Figure 8.2: Stability diagrams for three different suspended nanotubes with a length in between contacts of $1.2 \mu\text{m}$, 420 nm , and 140 nm for (a),(b) and (c) respectively. The conductance (dI/dV) is plotted as a function of source-drain voltage, V , and gate voltage, V_G . Blue corresponds to low and red to high conductance. Measurements have been performed at $T=300 \text{ mK}$ except in (a), where the base temperature was 10 mK . (a) Small region of a stability diagram showing closely spaced sets of lines running parallel to the Coulomb diamond edges for two charge states. At low bias, a strong suppression of the conductance is present. Red lines indicate positive differential conductance; blue lines negative differential conductance. Inset: regular diamonds that close are observed in a different cool down at $T= 300 \text{ mK}$. (b) and (c) Diamond crossings for two other samples, again showing lines parallel to the diamond edges with energy separations smaller than expected for electronic excitations.

that excitations occur primarily in one direction is due to asymmetric tunnel barriers [19].

The energy differences between the excitation lines of Fig. 8.2 are shown in the insets of Fig. 8.3. In all three cases, the excitation energy is an integer multiple of the first (fundamental) excitation. Thus, they form a harmonic spectrum

with up to 5 levels. A linear fit yields an excitation energy of 140, 690, and 530 μeV for the tubes with length 1.2 μm (a), 420 nm (b), and 140 nm (c), respectively. These values are an order of magnitude smaller than the expected mean electronic level spacing given by $\Delta = hv_F/2L$ with h the Planck constant and $v_F = 8.1 \cdot 10^5$ m/s [21] the Fermi velocity.

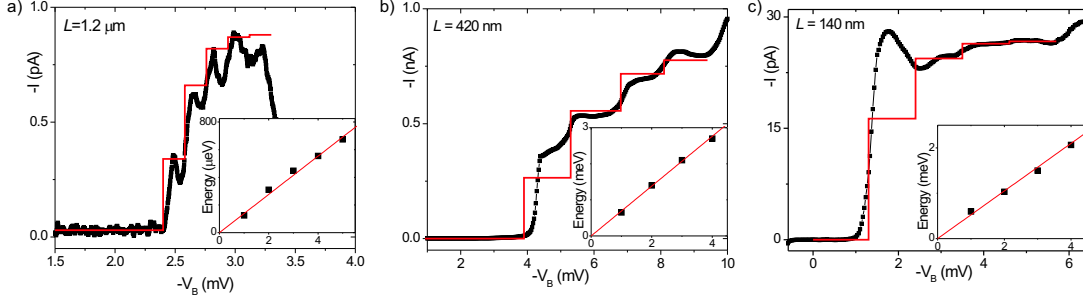


Figure 8.3: Current as a function of source-drain voltage at a gate voltage indicated by the green lines in Fig. 8.2. The red lines represent the step heights calculated in the Franck-Condon model (see text) for an electron-phonon coupling parameter of 0.95, 1.1, and 0.5 for (a), (b), and (c) respectively. In the insets, the energy separation between the peaks or steps (lines in Fig. 2) is plotted, showing equally spaced, harmonic spectrum. The slope of the drawn line is 140, 690, and 530 μeV for the insets of (a), (b), and (c) respectively.

8.3 Vibrational states and Franck-Condon model

A more natural explanation for the observed harmonic spectra is a vibrational mode coupled to an electron tunneling [11]. Multiple steps with identical spacing would then arise from the excitation of an integer number of vibrational quanta. Indeed, the observed equidistant energy separation is consistent with that expected from the longitudinal stretching mode in the nanotubes. In Fig. 8.4, we plot the energy of important low-energy vibrational modes of single-wall nanotubes [22, 23]. For comparison, we plot the mean electronic energy level separation, Δ , in black. Blue squares correspond to the fundamental excitation energy extracted from the linear fits in the insets of Fig. 8.3. The energy of the radial breathing mode (green) does not depend on the nanotube length and equals 28 meV/d(nm). The bending mode (red) has a L^{-2} dependence [25], and an energy much smaller than the measured excitation energy. The stretching mode vibration energy (blue) is inversely proportional to the length [24],

$E = (nh/L)\sqrt{Y/\rho_m}$, where Y is Young's modulus, ρ_m is the density and n is the vibrational quantum number. For nanotubes with $\rho_m = 1.3 \text{ g/cm}^3$, $Y = 1 \text{ TPa}$ the vibrational energy corresponding to the fundamental mode is $\sim 110 \mu\text{eV}/L(\mu\text{m})$ [23]. As Fig. 8.4 shows, the data are in good agreement with these predicted values.

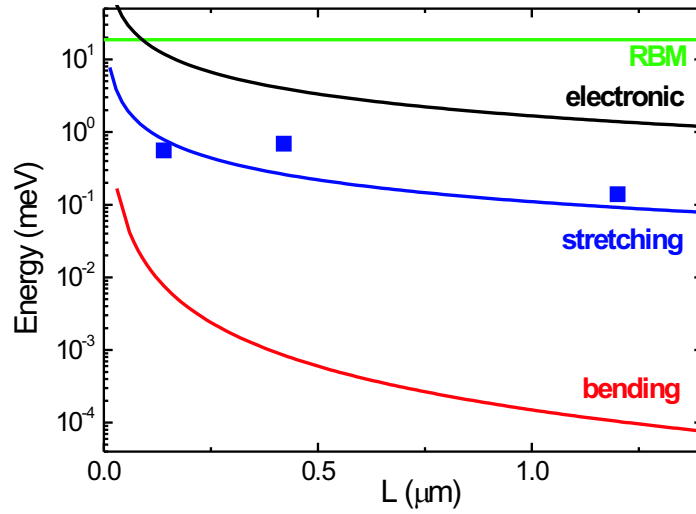


Figure 8.4: Energy scales of different vibrations and electronic excitations plotted on a log scale for a nanotube with a 1.4 nm diameter. The radial breathing mode (green) does not depend on the length L . The bending mode vibrations (red) have a L^{-2} dependence. The mean electronic level spacing (black) and the stretching mode (blue) vibrations depend inversely on the length.

The coupling of electronic levels with vibrational modes (quantum harmonic oscillators) can be described in terms of the Franck-Condon model [26]. According to the Franck-Condon principle, an electron in an electronic transition moves so fast that the nuclear positions are virtually the same immediately before and after the transition. As a consequence, the transition rate is proportional to the Franck-Condon factors defined as the square of the overlap integral between the vibrational wavefunctions of the two states involved. An important parameter is the electron-phonon coupling factor, $g = \frac{1}{2}(\frac{x}{x_0})^2$. This is the ratio of the classical displacement length, x , to the quantum mechanical oscillator length, $x_0 = \sqrt{\hbar/m\omega}$. Alternatively, $g = \frac{F^2}{2\hbar m \omega^3}$, where F is the force on, m the mass of, and ω the frequency of the oscillator.

For low damping, the vibrational levels remain sharp and the Franck-Condon

model predicts steps in the current-voltage characteristics, that are equally spaced in energy (bias voltage). In the presence of strong relaxation, the normalized step heights are given by [5]: $P_n = e^{-g}g^n/n!$. In the strong coupling ($g \gg 1$) limit, the height of the first steps is exponentially suppressed (phonon blockade) [5, 9, 10]. Multiple steps only arise if g is of the order of one or larger and the observation of a spectrum of equally spaced excitation lines therefore indicates that the e-ph coupling in our suspended nanotubes must be rather strong.

In Fig. 8.3, the red curves represent the step heights (P_n) given by the Franck-Condon model with strong relaxation discussed above. The symbols are the experimental curves taken at the green lines in Fig. 8.2. Considering the simplicity of the model, reasonable agreement is obtained in all three cases. The comparison yields an estimate of g of 0.95, 1.1, and 0.5 in Fig. 8.3a, b, and c respectively, indicating that it is approximately length independent. We have also performed a similar analysis at other gate voltages yielding the same g -values.

The theoretical curves in Fig. 8.3 do not exactly follow the measured ones. Better fits may be obtained if the influence of a gate voltage and asymmetric coupling is considered [5], or if coupling to excited electronic states [27] is considered, or if the influence of damping or non-equilibrium phonons (weak relaxation) is taken into account. In the latter case the peak heights are expected to display a non-systematic dependence on g and peak number [9]. Consideration of these effects is, however, beyond the scope of this paper.

The high value of the e-ph coupling ($g \sim 1$) is remarkable since in graphite the coupling between electrons and longitudinal phonons is weak. A source of intermediate to strong coupling could be the interaction between longitudinal and transverse vibrations [28]. Alternatively, we find that in suspended nanotubes the same e-ph coupling mechanism as in the bulk [29] can lead to a $g \sim 1$ if the electron density is inhomogeneous. The calculation proceeds as follows: The interaction energy of electrons with the polarization charge is characterized by the energy

$$W = - \int dx dx' \rho(x) K(x - x') \frac{\partial P}{\partial x'}. \quad (8.1)$$

Here, $\rho(x)$ is the density of excess charge produced by one electron, $K(x - x')$ is an interaction kernel, which we approximate by $\delta(x - x')$ for the case that interactions are effectively screened by the gate, and $P(x) \approx e\rho_0 z(x)$ is the polarization vector. The quantity $\rho_0 \sim k_F$ is the total electron density and $z(x)$ is the displacement, which in the single-mode approximation becomes $z(x) = A_n \sin(\pi n x/L)$. Calculating the force $F = -\partial W/\partial A_n$, we obtain

$$F = \frac{e\rho_0\pi n}{L} \int_0^L dx \rho(x) \cos \frac{\pi n x}{L}. \quad (8.2)$$

If the excess charge density is uniform, $\rho(x) = e/L$, $F = 0$ for all modes. Incorporation of interactions that are screened at distances longer than the distance to the gate, yields a force that scales as L^{-2} . In this case, the coupling parameter g also scales as L^{-2} and typical values are in the order of 10^{-3} , in apparent contradiction with the experimental data.

Assuming that the charge is localized in the center of the tube, $\rho(x) = e\delta(x - L/2)$, the force is zero for odd harmonics, but for even harmonics, $n = 2l$, it reads $F_l = (-1)^l e^2 \rho_0 2\pi l / L$. This results in a coupling parameter that is length independent and scales as l^{-1} : higher modes are coupled weaker to electrons. Numerical estimates show that $g \sim 1$. Localization of an electron in a point away from the middle produces coupling to both odd and even modes. Note that the electron does not have to be strongly localized to produce a $g \sim 1$. Such a non-uniform density can be created by impurities located in the substrate, or induced by a redistribution of electrons in a suspended tube bent by a underlying gate electrode [30].

An interesting feature of the data is the appearance of negative differential conductance (NDC) in the current-voltage characteristics. NDC is very pronounced in Fig. 8.3a, but also present in Fig. 8.3b,c. Although several explanations for NDC have been put forward, its origin remains unclear. Koch and von Oppen [10] showed that for low relaxation and strong e-ph coupling, NDC features appear, although they do not follow regions with strong positive differential conductance (PDC) as in our data. McCarthy *et al.* [6] have shown that NDC features can be due to an e-ph coupling that is voltage dependent. Their calculations also reproduce the catastrophic current decrease of Fig. 8.3a for bias voltages higher than 3 mV. However, at the moment we do not know how such a voltage dependence would arise in suspended tubes. Finally, Nowack and Wegewijs [27] have considered a Franck-Condon model with a coupling to an electronic and its excited state. They show that the competition between the two states generates strong NDC effects. NDC and PDC lines may have the same gate voltage dependence preceded by a region of suppressed current. This scenario may especially be relevant for the data in Fig. 8.3a.

In summary, transport measurements on suspended SWNTs show signatures of phonon-assisted tunneling, mediated by longitudinal vibrational (stretching) modes. The current-voltage characteristics show multiple steps whose heights are in reasonable agreement with the Franck-Condon predictions if the e-ph coupling constant is of order unity. Suspended nanotube quantum dots form an interesting model system for future studies on the interaction between single electrons and quantized phonons in the intermediate to strong electron-phonon coupling limit.

We thank Karsten Flensberg, Wataru Izumida, Leo Kouwenhoven, Leonid

Gurevich and Maarten Wegewijs for discussions. Financial support is obtained from the Dutch organization for Fundamental Research on Matter (FOM), which is financially supported by the 'Nederlandse Organisatie voor Wetenschappelijk Onderzoek' (NWO) and this research was supported by EC FP6 funding (contract no. FP6-2004-IST-003673). This publication reflects the views of the authors and not necessarily those of the EC. The Community is not liable for any use that may be made of the information contained herein.

References

- [1] M.L. Roukes, *Phys. World* **14**, 25 (2001).
- [2] A.N. Cleland, *Foundations of Nanomechanics* (Springer, Berlin, 2002).
- [3] L.Y. Gorelik *et al.*, *Phys. Rev. Lett.* **80**, 4526 (1998).
- [4] A. Erbe, C. Weiss, W. Zwerger, and R.H. Blick, *Phys. Rev. Lett.* **87**, 96106 (2001).
- [5] S. Braig and K. Flensberg, *Phys. Rev. B* **68**, 205324 (2003).
- [6] K.D. McCarthy, N. Prokof'ev, and M.T. Tuominen, *Phys. Rev. B* **67**, 245415 (2003).
- [7] Ya.M. Blanter, O. Usmani, and Yu.V. Nazarov, *Phys. Rev. Lett.* **93**, 136802 (2004); **94**, 049904(E) (2005).
- [8] N.M. Chtchelkatchev, W. Belzig, and C. Bruder, *Phys. Rev. B* **70**, 193305 (2004).
- [9] A. Mitra, I. Aleiner and A.J. Milles, *Phys. Rev. B* **69**, 245302 (2004).
- [10] J. Koch and F. von Oppen, *Phys. Rev. Lett.* **94**, 206804 (2005).
- [11] H. Park *et al.*, *Nature (london)* **407**, 57 (2000).
- [12] A.N. Pasupathy *et al.*, *Nano Lett.* **5**, 203 (2005).
- [13] E.M. Weig *et al.*, *Phys. Rev. Lett.* **92**, 46804 (2004).
- [14] B. Reulet *et al.*, *Phys. Rev. Lett.* **85**, 2829 (1999).
- [15] V. Sazonova *et al.*, *Nature (London)* **431**, 284 (2004).
- [16] B.J. LeRoy, S.G. Lemay, J. Kong, and C. Dekker, *Nature (London)* **432**, 371 (2004).
- [17] J. Nygård and D.H. Cobden, *Appl. Phys. Lett.* **79**, 4216 (2001).
- [18] H. Grabert and M.H. Devoret, Eds. *Single Charge Tunneling* (Plenum, New York, 1992).

- [19] L.P. Kouwenhoven, D.G. Austing, and S. Tarucha, Rep. Prog. Phys. **64**, 701 (2001).
- [20] D.H. Cobden *et al.*, Phys. Rev. Lett. **81**, 681 (1998).
- [21] S. Lemay *et al.*, Nature (London) **412**, 617 (2001).
- [22] M.S. Dresselhaus and P.C. Eklund, Adv. Phys. **49**, 705 (2000). H. Suzuura and T. Ando, Phys. Rev. B **65**, 235412 (2002). A. De Martino and R. Egger, Phys. Rev. B **67**, 235418 (2003).
- [23] The twisting mode vibration of the nanotube has a comparable energy with the stretching mode. However, the twisting mode does not couple [22].
- [24] L.D. Landau and E.M. Lifshitz, *Theory of Elasticity* (Pergamon, Oxford, 1986).
- [25] S. Sapmaz, Ya.M. Blanter, L. Gurevich, and H.S.J. van der Zant, Phys. Rev. B **67**, 235414 (2003).
- [26] G.C. Schatz, and M.A. Ratner, *Quantum Mechanics in Chemistry* (Prentice-Hall, Englewood Cliffs, 1993).
- [27] K.C. Nowack and M. Wegewijs, cond-mat/0506552.
- [28] K. Flensberg, private communication.
- [29] A. A. Abrikosov, *Fundamentals of the Theory of Metals* (North-Holland, New York, 1988).
- [30] D. Fedorets (unpublished).

Summary

Quantum transport in carbon nanotubes

Electronic transport through nanostructures can be very different from transport in macroscopic conductors, especially at low temperatures. Carbon nanotubes are tiny cylinders made of carbon atoms. Their remarkable electronic and mechanical properties, together with their small size (a few nm in diameter), make them very attractive for scientific research, both from the basic as well as from the technological point of view. This thesis describes experimental research aimed at understanding electronic transport through carbon nanotubes (CNTs) at low temperatures. At these temperatures (below a few Kelvin), the quantum properties of CNTs have a strong influence in their transport behavior. When two metallic electrodes are deposited on top of a nanotube, tunnel barriers develop at the nanotube-metal interfaces, leading to the formation of a quantum dot within the nanotube segment in between the electrodes. A quantum dot, *or artificial atom*, is a small box where we can place electrons in discrete energy states, due to quantum confinement in the three directions of space. The short spacing in between the electrodes (\sim few hundred nm), together with the small diameter of carbon nanotubes, makes it possible to observe the quantum properties of carbon nanotubes at temperatures below ~ 10 K.

Depending on the coupling between the nanotube and the leads, different regimes can be experimentally studied. For very opaque tunnel barriers, the electrons are strongly confined in the quantum dot (QD), the electrostatic interactions between electrons, or charging effects, are large, and transport occurs via single electron tunneling processes. In this ‘closed QD’ regime, the energy levels have a very small energy width and we can perform accurate measurements to determine the spectrum of short CNTs. Chapters 3, 4, and 8 study nanotubes in this regime. As the transparency of the barriers increases, the confinement weakens and higher order tunneling processes become more probable. We can still perform spectroscopy by means of inelastic cotunneling, and interesting phenomena involving the spin coherence between the electrons in the QD

and those in the leads, namely the Kondo effect, can occur. This intermediate transparency regime is studied in chapters 5 and 6. Finally, when the barriers are rather transparent and the interactions between electrons can be neglected, transport is dominated by quantum interference. We call this the ‘open QD’ regime. The discreteness of the energy spectrum manifests itself in phenomena such as resonant tunneling, which is explored in chapter 7 for the especial case of superconducting leads. Altogether, the chapters in this thesis cover a wide range of phenomena observed in these different regimes.

Chapter 3 reports the first observation of the energy spectrum of semiconducting carbon nanotubes. We realize a few electron-hole QD and find that the spectra of electrons and holes in CNTs are symmetric, as expected from the symmetry in the band structure. Such spectra could not be compared before for any other type of QDs.

In chapters 4, 5, and 6 we study different effects of the double orbital degeneracy of the band structure of CNTs on their transport properties. Chapter 4 concerns the excitation spectrum of metallic nanotubes. By using a model which includes charging and exchange effects, as well as the four-fold degeneracy of the electronic states in CNTs, we are able to understand the ground state addition energies of NT QDs and their excitation spectra. This four-fold degeneracy manifests itself also in the addition energy spectra of small band gap CNTs, as shown in chapter 5, where this time we focus on the effects of an axial magnetic field on the transport through the NT QDs. We study the evolution of the Coulomb peaks with magnetic field and are able to identify the different orbital and spin transitions in the ground state of the QD. Such degree of understanding is unprecedented for NT QDs. By means of inelastic cotunneling spectroscopy, we also show that there are two contributions to the magnetic moment of electrons in CNTs: orbital and spin, and we observe all possible manifestations of it in the cotunneling spectrum.

The orbital magnetic moment can be thought off as a pseudospin, because it behaves similar to the electron spin. In chapter 6 we focus on the consequences of this pseudospin and the orbital degeneracy associated with it on the Kondo effect in CNTs. We demonstrate that the orbital pseudospin leads to an orbital Kondo effect at high magnetic field, i.e., a Kondo effect with spin polarized electrons. At zero magnetic field, the spin and pseudospin degrees of freedom combined give rise to an $SU(4)$ Kondo effect, manifested as a multiple splitting of the Kondo resonance at finite fields.

In chapter 7 we study how is the transport through a CNT in the open QD regime modified by the presence of superconducting leads. Remarkably, we are able to measure small supercurrents flowing through the NTs. By means of a

gate electrode, we tune the energy levels of the NT QD ON and OFF resonance with respect to the Fermi energy in the leads, resulting in a resonant tunneling transistor-like action of the critical currents through the nanotubes. Our experiment confirms existing theoretical predictions on how a supercurrent flows through a system with a discrete density of states, i.e., a QD.

The last chapter of the thesis is devoted to the study of electronic transport on suspended CNT QDs. We measure a set of anomalously small excitation energies, which cannot be identified as due to electronic excitations and we propose that they are due to phonon assisted tunneling processes in the QD. The current-voltage characteristics indicate a rather strong electron-phonon coupling in suspended carbon nanotubes.

Pablo Jarillo-Herrero
September 2005

Samenvatting

Kwantum transport in koolstof nanobuisjes

Elektrisch transport door nanostructuren kan erg verschillen van transport door macroscopische geleiders, in het bijzonder bij lage temperaturen. Koolstof nanobuisjes zijn kleine cilinders van koolstof atomen. De opmerkelijke elektrische en mechanische eigenschappen, samen met de kleine afmetingen (enkele nm in diameter), maken ze erg interessant voor fundamenteel onderzoek, zowel vanuit fundamenteel als toegepast oogpunt.

Dit proefschrift beschrijft experimenteel onderzoek gericht op het begrijpen van elektrisch transport door koolstof nanobuisjes (CNTs) bij lage temperaturen. Bij deze lage temperaturen (beneden een paar Kelvin), hebben de kwantum eigenschappen van CNTs een belangrijke invloed op het elektrisch gedrag. Wanneer twee metallische elektrodes worden aangebracht op een nanobuisje ontstaan tunnel barrières aan het metaal-nanobuisje grensvlak, resulterend in een kwantum dot in het nanobuisje segment tussen de elektrodes. Een kwantum dot, of artificieel atoom, is een klein doosje waarin we elektronen kunnen plaatsen in discrete energietoestanden vanwege de kwantum opsluiting in de drie ruimtelijke dimensies. De kleine afstand tussen de elektrodes (\sim een paar honderd nm), in combinatie met de kleine diameter van de nanobuisjes, maakt het mogelijk om kwantum eigenschappen van de koolstof nanobuisjes waar te nemen bij temperaturen beneden ~ 10 K.

Afhankelijk van de koppeling tussen het nanobuisje en de contacten, kunnen verschillende regimes worden bestudeerd. Voor erg gesloten barrières zijn de elektronen gelokaliseerd in de kwantum dot (QD) en zijn de elektrostatische interacties tussen de elektronen (ladingseffecten) sterk, waardoor transport plaatsvindt via het tunnelen van enkele elektronen. In dit ‘gesloten QD’ regime, is de breedte van de energieniveaus erg klein en kunnen we nauwkeurige metingen uitvoeren om het spectrum te bepalen van korte CNTs. Hoofdstukken 3, 5 en 8 gaan over nanobuisjes in dit regime. Als de transparantie van de barrières groter wordt, wordt de lokalisatie kleiner en worden hogere orde tunnel processen

waarschijnlijker. We kunnen nog steeds spectroscopie uitvoeren met behulp van inelastische co-tunneling en interessante fenomenen zoals het Kondo effect kunnen optreden, welke betrekking hebben op de spin coherentie tussen de elektronen in de QD en die in de contacten. Dit tussenliggende regime in transparantie wordt behandeld in hoofdstukken 5 en 6. Als de barrières behoorlijk transparant zijn en interacties tussen elektronen kunnen worden verwaarloosd, is transport gedomineerd door kwantum interferentie. We noemen dit het ‘open QD’ regime. Het discrete energie spectrum resulteert in bijvoorbeeld resonante tunneling, wat wordt behandeld in hoofdstuk 7 voor het bijzondere geval van supergeleidende contacten. Samen beslaan de hoofdstukken van dit proefschrift een breed scala aan fenomenen in deze verschillende regimes.

Hoofdstuk 3 gaat over de eerste meting van het energie spectrum van halfgeleidende koolstof nanobuisjes. We realiseren een QD met maar enkele elektron- en gaten en vinden dat het spectrum van elektron en gaten in de CNTs symmetrisch is, zoals verwacht vanwege de symmetrische banden structuur. Zulke spectra konden in andere typen QDs niet worden vergeleken.

In hoofdstukken 4, 5 en 6 bestuderen we verschillende effecten op de transporteigenschappen van CNTs die te maken hebben met de dubbele orbitale onttaarding van de banden structuur. Hoofdstuk 4 behandelt het excitatie spectrum van metallische nanobuisjes. Door gebruik te maken van een model dat rekening houdt met ladings-effecten, exchange interactie en de 4-voudige onttaarding van de elektronische toestanden in CNTs, kunnen we de grondtoestand additie energieën en hun excitatie spectra begrijpen. Deze 4-voudige onttaarding manifesteert zichzelf ook in de additie spectra van kleine bandgap CNTs, zoals beschreven is in hoofdstuk 5. Hier focuseren we op effecten van een axiaal magnetisch veld op de transporteigenschappen door NT QDs. We bestuderen de evolutie van de Coulomb pieken in een magnetisch veld en zijn in staat om de verschillende orbitale en spin transitie te identificeren in de grondtoestand van de QD. Door middel van co-tunneling spectroscopie kunnen we ook laten zien dat er twee bijdragen zijn aan het magnetisch moment van elektronen in CNTs: orbitaal en spin. In het co-tunneling spectrum kunnen we alle mogelijke combinaties hiervan bestuderen.

Het orbitale magnetisch moment kan worden gezien als een pseudospin omdat het zich gedraagt als een elektron spin. Hoofdstuk 6 gaat over de gevolgen van deze pseudospin, en de geassocieerde orbitale onttaarding, op het Kondo effect in CNTs. We laten zien dat de orbitale pseudospin leidt tot een orbitaal Kondo effect bij hoge magneetvelden, oftewel een Kondo effect met spin gepolariseerde elektronen. Bij nul magnetisch veld, resulteren de spin en pseudospin samen in het $SU(4)$ Kondo effect. Dit manifesteert zich in een meervoudige splitsing van

de Kondo resonantie in een eindig magnetisch veld.

In Hoofdstuk 7 bestuderen we hoe het transport door een CNT in het open QD regime verandert met supergeleidende contacten. We zijn in staat kleine superstromen te meten door de NTs. Door middel van een gate electrode kunnen we de energie niveaus van de NT QD variëren zodat ze AAN of UIT resonantie zijn met de Fermi energie in de contacten. Dit resulteert in een transistor werking door resonante tunneling van de superstroom door de nanobuisjes. Onze experimenten bevestigen bestaande theoretische voorspellingen over hoe een superstroom door een systeem met een discrete toestandsdichtheid, zoals een QD, stroomt.

Het laatste hoofdstuk van dit proefschrift is gewijd aan het elektrisch transport door opgehangen CNT QDs. We meten een verzameling van abnormaal lage excitatie energieën, die niet geïdentificeerd kunnen worden als elektronische excitaties en we stellen dat ze veroorzaakt worden door fonongerelateerde tunnel processen in de QD. De stroom-spanning karakteristieken geven aan dat de elektron-fonon koppeling behoorlijk sterk is in opgehangen koolstof nanobuisjes.

Pablo Jarillo-Herrero
September 2005

Curriculum Vitae

Pablo David Jarillo-Herrero

- 11-06-1976 Born in Valencia, Spain.
- 1990-1994 Secondary school at Colegio Jesuitas in Valencia.
- 1994-1999 Licenciado in Physics,
University of Valencia.
- 1999-2001 M.Sc. Physics,
University of California San Diego.
- 2001-2005 Ph.D research at Delft University of Technology
under supervision of prof.dr.ir. L.P. Kouwenhoven
Subject: Quantum transport in carbon nanotubes

List of publications

1. *Coupling between electrons and longitudinal phonons in suspended nanotubes*
S. Sapmaz, P. Jarillo-Herrero, Ya. M. Blanter, and H. S. J. van der Zant.
To be submitted to New Journal of Physics, special issue on Nano-electromechanical systems.
2. *Quantum supercurrent transistors in carbon nanotubes*
P. Jarillo-Herrero, J. A. van Dam, and L. P. Kouwenhoven.
Submitted to Nature (2005).
3. *Tunneling in suspended carbon nanotubes assisted by longitudinal phonons*
S. Sapmaz, P. Jarillo-Herrero, Ya. M. Blanter, C. Dekker, and H.S.J. van der Zant.
Submitted to Physical Review Letters (2005).
See also <http://xxx.lanl.gov/abs/cond-mat/0508270> (2005).
4. *Tunable Orbital Pseudospin and Multi-level Kondo Effect in Carbon Nanotubes*
P. Jarillo-Herrero, J. Kong, H. S. J. van der Zant, C. Dekker, L. P. Kouwenhoven, and S. De Franceschi.
To appear in Proceedings of the International Winterschool on Electronic Properties of Novel Materials (2005).
5. *Electronic transport spectroscopy of carbon nanotubes in a magnetic field*
P. Jarillo-Herrero, J. Kong, H. S. J. van der Zant, C. Dekker, L. P. Kouwenhoven, and S. De Franceschi.
Physical Review Letters **94**, 156802 (2005).
6. *Electronic excitation spectrum of metallic carbon nanotubes*
S. Sapmaz, P. Jarillo-Herrero, J. Kong, C. Dekker, L. P. Kouwenhoven, and H. S. J. van der Zant.
Physical Review B **71**, 153402 (2005).
7. *Orbital Kondo effect in carbon nanotubes*
P. Jarillo-Herrero, J. Kong, H. S. J. van der Zant, C. Dekker, L. P. Kouwenhoven, and S. De Franceschi.
Nature **434**, 484 (2005).

8. *A few electron-hole semiconducting carbon nanotube quantum dot*
P. Jarillo-Herrero, S. Sapmaz, C. Dekker, L. P. Kouwenhoven, and H. S. J. van der Zant.
Proceedings of the International Winterschool on Electronic Properties of Novel Materials 583 (2004).
9. *Electron-hole symmetry in a semiconducting carbon nanotube quantum dot*
P. Jarillo-Herrero, S. Sapmaz, C. Dekker, L. P. Kouwenhoven, and H. S. J. van der Zant.
Nature **429**, 389 (2004).
10. *Production of Very Neutron-Deficient Isotopes near ^{100}Sn via Reactions Involving Light-Particle and Cluster Emission*
M. La Commara, J. Gómez del Campo, A. D'Onofrio, A. Gadea, M. Glogowski, P. Jarillo-Herrero, N. Belcari, R. Borcea, G. de Angelis, C. Fahlander, M. Górska, H. Grawe, M. Hellström, R. Kirchner, M. Rejmund, V. Roca, E. Roeckl, M. Romano, K. Rykaczewski, K. Schmidt, and F. Terrasi.
Nucl. Phys. A **689**, 43 (2000).